

**COUPLED LITHOSPHERE-MANTLE DYNAMICS AND
SURFACE RESPONSES: INSIGHTS FROM MODELING**

PhD. Thesis
by Flora Bajolet

presented at “University Roma Tre”
in the section Geology of the Environment and Geodynamics
(Geologia dell’Ambiente e Geodinamica, XXV ciclo)

Under the supervision of
Claudio Faccenna and Francesca Funiciello

External reviewers:

Dimitrios Sokoutis – University of Utrecht (The Netherlands)

Laurent Husson – University of Rennes 1 (France)

Abstract

The focus of this work is to understand the interaction in space and time between mantle and lithosphere under different conditions. In a first part, I explore the behavior of the lithosphere under a vertical surface load whilst a second part deals with deep lithospheric load. The third chapter presents preliminary results on dynamic topography in subduction zone. Finally, in a fourth chapter I investigate the surface evolution under kinematically imposed convergence.

The adopted methodology consists in scaled analog experiments simulating the lithosphere and upper mantle, during which mantle flow, kinematics, surface topography and deformation can be recorded. The results are then compared with numerical simulations and natural data.

Surface loading/unloading experiments using a visco-elastic lithosphere show that we can simulate isostatic rebound using layers of silicone putty and gelatin. Reequilibration occurs in two phases: a fast elastic reequilibration at the My time-scale, and a slower viscous response spanning over tenth of My.

The presence of a deep lithospheric load is modeled by a thick lithospheric root inducing continental delamination. This process produces a complex topographic signal combining isostasy, flexure and dynamic topography coupled with mantle flow and surface deformation. The performed experiments provide a first order quantification of the forces at work alongside with empirical constraints.

The third part aims at modeling subduction zone and tracking dynamic topography, especially in the overriding plate.

Results of the fourth part of this work show that kinematically imposed convergence during subduction and collision can lead to the formation of a curved orogen with various topographic patterns. In that case, strength of the subduction fault zone, rheology of the upper plate and boundary conditions are the most important parameters controlling mantle-lithosphere interactions.

TABLE OF CONTENTS

GENERAL INTRODUCTION	5
PART I: SURFACE LOADING/UNLOADING	9
1. INTRODUCTION AND PURPOSES	10
2. EXPERIMENTS SETUP	10
2.1. Rheological properties of the materials	10
2.2. Experimental procedure	12
3. PRELIMINARY RESULTS	13
3.1. Model 1: viscous lithosphere, undeformable load	13
3.2. Model 2: visco-elastic lithosphere, deformable load	15
CONCLUSIONS AND PERSPECTIVES	16
PART II: DEEP LITHOSPHERIC LOADING	19
1. INTRODUCTION	21
2. EXPERIMENTAL SETUP	23
3. EXPERIMENTAL RESULTS	26
3.1. Evolution of the reference experiment (DEL 10)	26
3.1.1. Initiation of delamination	29
3.1.2. Main phase of delamination	32
3.1.3. Final stage	35
3.2. Sensitivity analysis	37
4. DISCUSSION	38
4.1. Forces at work during delamination	38
4.2. Dynamics of delamination and surface response	40
4.3. Comparison with previous modeling results	45
4.4. Comparison with natural systems	46
7. CONCLUSIONS	48
8. NOTATION	49
PART III: DYNAMIC TOPOGRAPHY IN SUBDUCTION ZONES	58
1. INTRODUCTION, MODEL SETUP AND FORCE BALANCE	59
1.1. Introduction	59
1.2. Model setup	59
1.3. Force balance	61

2. EXPERIMENTAL RESULTS.....	62
3. DISCUSSION AND CONCLUSIONS.....	66
PART IV: SURFACE EXPRESSIONS OF SUBDUCTION AND COLLISION.....	70
1. INTRODUCTION	72
2. MODEL SETUP AND EXPERIMENTAL PROCEDURE.....	75
2.1. Model setup	75
2.2. Forces equilibrium	78
<i>Driving forces</i>	78
<i>Resisting forces</i>	79
<i>Buoyancy number</i>	81
3. EXPERIMENTAL RESULTS: GENERATING CURVATURE AND SYNTAXES	81
3.1. First set (low F_b), high viscosity asthenosphere (SH7)	82
3.2. First set (low F_b), low viscosity asthenosphere (SH22)	85
3.3 First set (low F_b), low viscosity asthenosphere, weak upper plate (SH9).....	86
3.4. Second set (high F_b), high viscosity asthenosphere, weak upper plate (SH15).....	87
3.5. Second set (high F_b), low viscosity asthenosphere, thick and weak upper plate (SH13).....	89
3.6. Third set (lateral oceans), low F_b , high viscosity asthenosphere (SH6).....	91
3.7. Third set (lateral oceans), high F_b , low viscosity asthenosphere (SH20).....	92
4. DISCUSSION: RANGE SHAPE EVOLUTION.....	94
4.1. Subduction efficiency	94
4.2. Buoyancy number	95
4.3. Lateral decoupling.....	97
4.4. Comparison with the India-Asia collision	99
5. CONCLUSIONS: FOUR END-MEMBERS REGIMES OF INDENTATION.....	101

General introduction

The topography on Earth has intrigued scientists for a long time, but only recently we started to understand the influence deep processes can have on the surface, both in terms of topography and deformation.

The very first models trying to understand topography were models of isostatic compensation that can be of two types [Stüwe, 2002; Watts, 2001]:

- Hydrostatic, where the compensation is determined by the topographic load [Airy model, 1855]. The principle is to do a vertical balance of stresses, the lithosphere is assumed to have zero strength, and such methods are valid for large regions [Turcotte and Schubert, 1982].
- Flexural models where the lithosphere is considered as a layered body with visco-elastic behavior. This method takes into account horizontal elastic stresses, and can thus be applied both in 2D or 3D.

Flexure of the lithosphere has an important impact on surface topography in numbers of geologic contexts such as volcanic seamounts loading, bending of passive margins, foreland basins, or post-glacial rebound. Several analytical or numerical models have been performed in the last decades, but analog approach has not been deeply explored.

Additionally, a dynamic component can be added to the topography: it corresponds to the part of the signal responding to stresses arising from the mantle [e.g. Colin and Fleitout, 1990; Conrad and Husson, 2009; Moucha et al., 2008]. Especially, dynamic topography in subduction zones have been investigated as it can produce changes in elevation of the order of kilometers [e.g. Gurnis, 1990b, 1992; Mitrovica, 1996; Liu et al. 2008; Guillaume et al., 2009; Faccenna and Becker, 2010; Husson et al., 2012; Melosh and Raefsky, 1980; Zhong and Gurnis, 1994; Husson, 2006].

However, in most cases, it is difficult to distinguish the effects of isostasy, flexure and dynamic topography. In the following chapters, we will investigate several geodynamic contexts and try to decipher the relationships between deep processes and surface responses, both topography and deformation.

Airy, G.B. (1855). On the computation of the effect of the attraction of mountain-masses as disturbing the apparent astronomical latitude of stations in geodetic surveys. *Philosophical Transactions of the Royal Society of London*, 145, 101–104.

Colin, P., and L. Fleitout (1990). Topography of the ocean floor: thermal evolution of the lithosphere and interaction of deep mantle heterogeneities with the lithosphere. *Geophysical Research Letters*, 17, 1961–1964.

Conrad, C.P., and L. Husson (2009). Influence of dynamic topography on sea level and its rate of change. *Lithosphere*, 1, 110–120.

Faccenna, C., and T.W. Becker (2010). Shaping mobile belts by small-scale convection. *Nature*, 465, 602–605.

Funiciello, F., M. Moroni, C. Piromallo, C. Faccenna, A. Cenedese, and H.A. Bui (2006). Mapping mantle flow during retreating subduction: laboratory models analyzed by feature tracking. *Journal of Geophysical Research*, 111, 3402.

Guillaume, B., J. Martinod, L. Husson, M. Roddaz, and R. Riquelme (2009). Neogene uplift of central eastern Patagonia: dynamic response to active spreading ridge subduction? *Tectonics*, 28, C2009.

Gurnis, M. (1990b). Ridge spreading, subduction, and sea level fluctuations. *Science*, 250, 970–972.

Gurnis, M. (1992). Rapid continental subsidence following the initiation and evolution of subduction. *Science*, 255, 1556–1558.

Husson, L. (2006). Dynamic topography above retreating subduction zones. *Geology*, 34(9), 741-744.

Husson, L. (2012), B. Guillaume, F. Funiciello, C. Faccenna, and L.H. Royden. Unraveling topography around subduction zones from laboratory models. *Tectonophysics*, 526-529, 5-15.

Liu, L., S. Spasojević, and M. Gurnis (2008). Reconstructing Farallon Plate subduction beneath North America back to the Late Cretaceous. *Science*, 322, 934-938.

Melosh, H.J., and A. Raefsky (1980). The dynamical origin of subduction zone topography. *Geophysical Journal*, 60, 333–354.

Mitrovica, J. (1996). The Devonian to Permian sedimentation of the Russian Platform: an example of subduction-controlled long-wavelength tilting of continents. *Journal of Geodynamics*, 22, 79–96.

Moucha, R., A.M. Forte, J.X. Mitrovica, D.B. Rowley, S. Quéré, N.A. Simmons, and S.P. Grand (2008). Dynamic topography and long-term sea-level variations: there is no such thing as a stable continental platform. *Earth and Planetary Science Letters*, 271, 101–108.

Stüwe, K. (2002). *Geodynamics of the Lithosphere*. Springer, Berlin, 449pp.

Turcotte, D.L., and G. Schubert (1982). *Geodynamics: Application of Continuum Physics to Geological Problems*. Wiley, New York, NY 450pp.

Watts, A.B. (2001). *Isostasy and Flexure of the Lithosphere*. Cambridge University Press, Cambridge, UK 478pp.

Zhong, S., and M. Gurnis (1992). Viscous flow model of a subduction zone with a faulted lithosphere: long and short wavelength topography, gravity and geoid. *Geophysical Research Letters*, 19, 1891–1894.

Zhong, S., and M. Gurnis (1994). Controls on trench topography from dynamic models of subducted slabs. *Journal of Geophysical Research*, 99, 15683.

Part I: Surface loading/unloading

1. Introduction and purposes

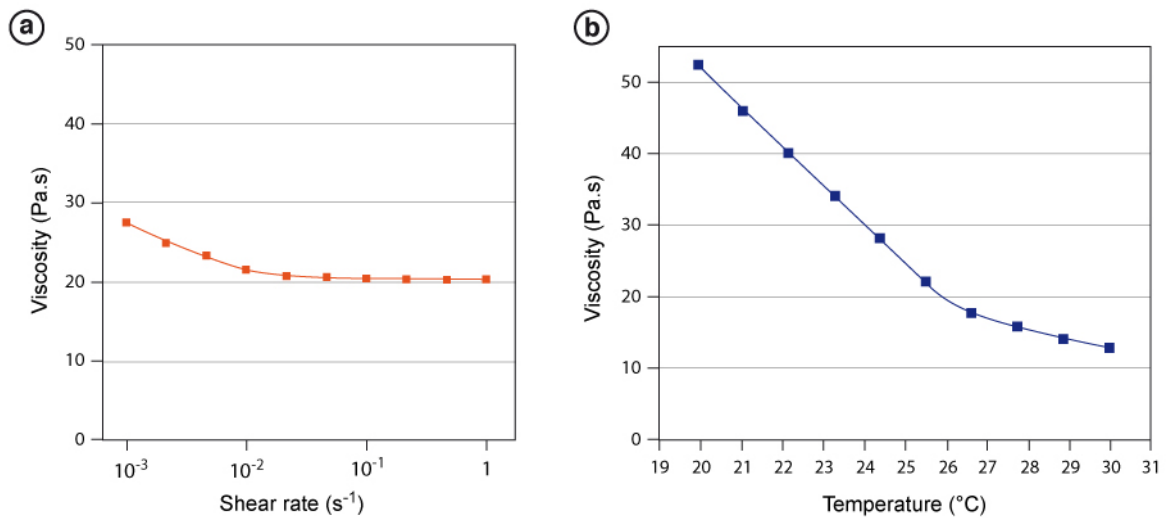
The flexural isostasy arising from the rigidity of the lithosphere and accompanying loading and unloading processes has a major contribution of Earth's topography. It has been observed in various settings such as loading in volcanic areas or foreland basins, bending of passive margins, or post-glacial rebound. These processes have previously been quantified with analytical and numerical means, but have not been tested with analog models.

The main purpose of this preliminary study is to elaborate an experimental procedure reproducing surface loading/unloading and able to take into account the visco-elastic properties of the lithosphere.

2. Experiments setup

2.1. Rheological properties of the materials

In our models, we use three types of analog materials: glucose syrup, silicone putties and gelatin. The glucose syrup simulating the asthenospheric mantle is a simple Newtonian fluid at experimental strain rates (ca. 10^{-2} s^{-1}), whose viscosity varies with the temperature (Figure I.1ab). The silicone putty is a visco-elastic material that is considered quasi-Newtonian at experimental strain rates [Weijermars, 1986], and also shows a dependence on temperature (Figure I.1c).



(Legend on next page)

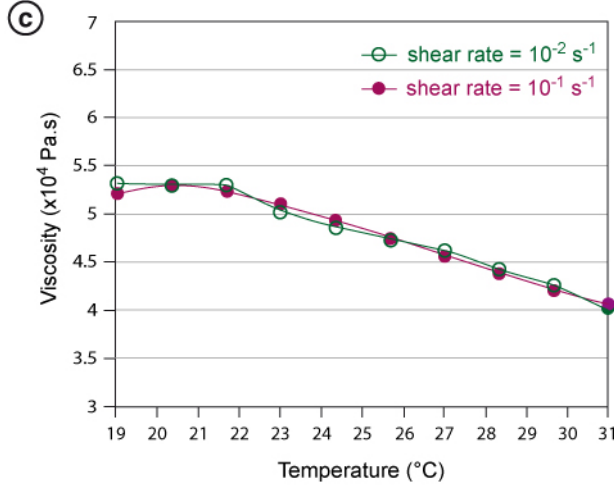


Figure I.1. Viscosity of the glucose syrup depending on (a) shear rate and (b) temperature. (c) Viscosity of the silicone putty depending on temperature for two experimental shear rates.

Gelatins are also visco-elastic material but with a non-negligible elastic component. The response of these materials to stress is time-dependent and can be characterized measuring the deformation energy stored during deformation and lost afterwards [Mezger, 2002]. If the storage modulus G' is largely superior to the loss modulus G'' at a given frequency ω , the material will behave elastically, while in the frequency range where $G'' \gg G'$, it will behave viscously [Figure I.2a; Mezger, 2002]. We use pig skin gelatin powder mixed with water at 2.5%wt and 10°C since it has been shown fitted to model lithosphere rheological behavior [Figure I.2b; Di Giuseppe et al., 2009].

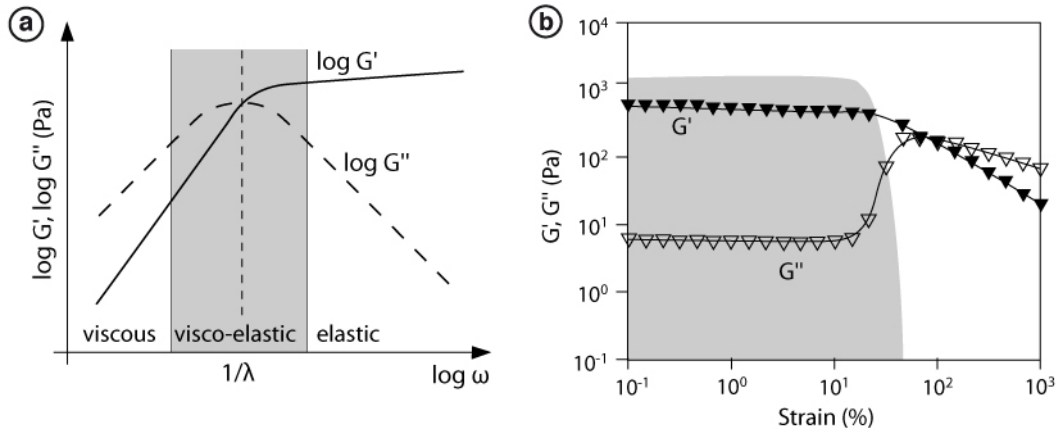


Figure I.2. (a) Evolution of the storage and loss modulus, G' and G'' with the frequency ω for an ideal visco-elastic material. In the visco-elastic domain, G' and G'' are of the same order of magnitude. The intersection between the two curves determines the relaxation time of the system (λ) [modified after Di Giuseppe et al., 2009]. (b) G' and G'' measured for pig skin gelatin at 2.5%wt and 10°C. The shaded area represents the visco-elastic domain [modified after Di Giuseppe et al., 2009].

2.2. Experimental procedure

We performed two types of models (Figure I.3). In the first type of models, the lithosphere is modeled by a single layer of silicone and the load is undeformable (Figure I.3a). In the second type of models, we add a thin layer of gelatin on top of the silicone and the load itself is made of deformable gelatin (Figure I.3b). Characteristics of the plates and loads are given in Table I.1. In all cases, the modeled lithosphere is lying on top of low-viscosity glucose syrup simulating the asthenosphere. The bottom of the box represents the 660 km discontinuity. The model is unconstrained in all directions, and no tectonic forces are applied. We place the load at the center of the plate and leave it for 30 min (loading phase), then remove it (unloading phase). This setup implies the following assumptions, and consequent limitations, that are detailed in *Funiciello et al.* [2003]: (1) isothermal system, (2) constant viscosity and density over the depth of the individual layers, and (3) lack of global background mantle flow. The topography evolution is monitored with a 3D laser-scanner (Real Scan USB) whose precision is 0.1 mm corresponding to 600 m in nature.

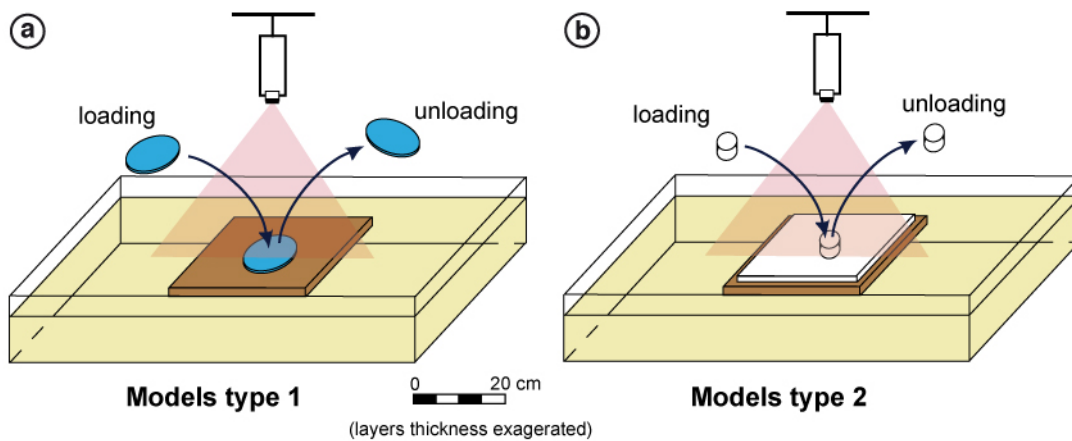


Figure I.3. (a) Experimental setup for the first type of models with a single silicone layer (brown) and a spherical undeformable load. (b) Models type 2 with silicone and gelatin layers (white) and deformable load.

Parameters		Model 1	Model 2
Plate size (cm ²)	30 x 30	30 x 30	30 x 30
Silicone thickness (cm)	1.2	1.2	1.2
Gelatin thickness (cm)	n/a		0.3
Load size	diameter 12cm, height 3mm		diameter 3 cm, height 2 cm
Load weight (g)	46		11

Table I.1. Experimental parameters.

3. Preliminary results

All the topographic maps presented thereafter are the difference between two scans and thus represent a difference in elevation (Δz) for a certain time step. The vertical resolution of the scanner is 0.1 mm and variations inferior to that value are background noise.

3.1. Model 1: viscous lithosphere, undeformable load

As soon as the system is loaded, a depression is created in the center edged by a flexural bulge due to the bending of the plate (Figure I.4a). It induces about 1 mm of uplift during the first 10 min of loading. The width of the area affected by the flexural bulge is about one half of the load diameter. The elevation of the rest of the plate remains unchanged. Deformation of the plate continues during the time span 10 to 30 min but with a smaller amplitude (Figure I.4b). In 20 min, the flexural bulge is uplifted by ca. 0.5 mm.

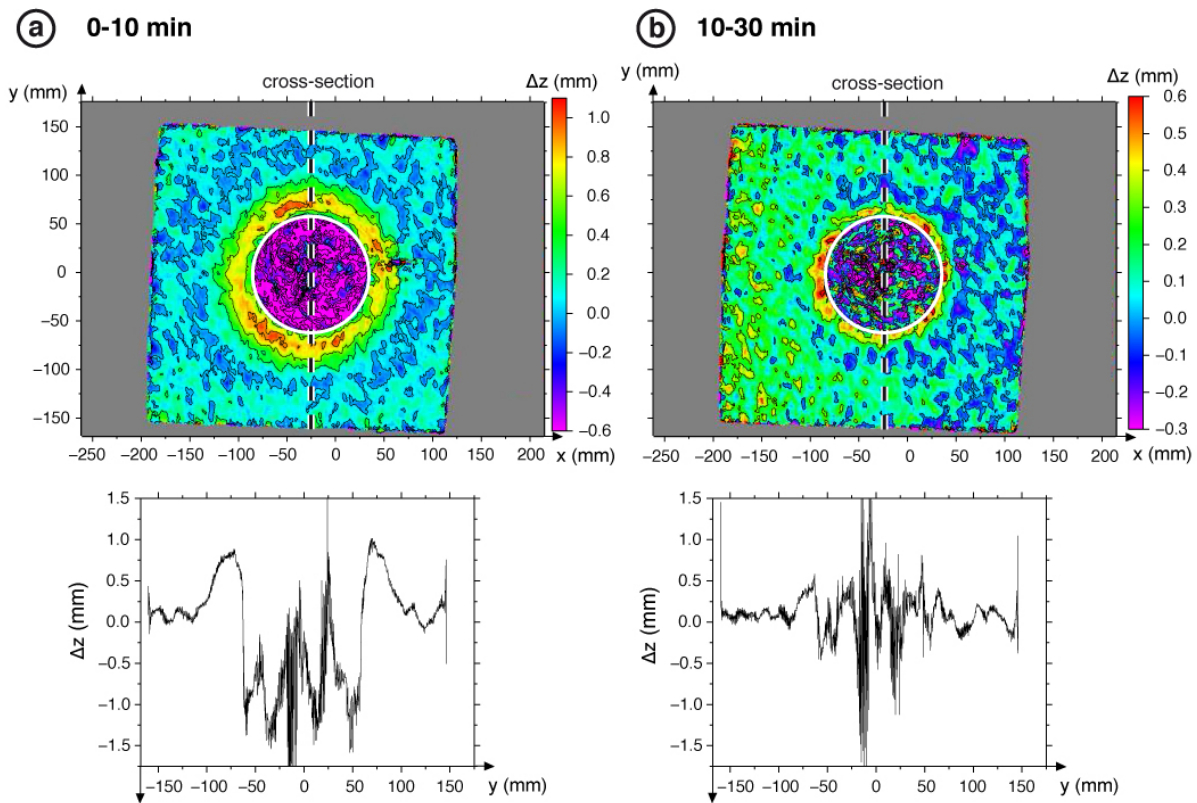


Figure I.4. Map view and corresponding cross-section (along the axis $x = -25$) of topography evolution (Δz) for the model 1 during loading phase, (a) for the time step 0 to 10 min, (b) for time step 10 to 30 min. The white circle highlights the position of the load.

After 30 min, the elevation is stable, and we remove the load. We observe an uplift of the plate, at first with a stronger amplitude in the centre, then propagating in the whole model (Figure I.5). On the contrary, the flexural bulge undergoes subsidence and progressively reequilibrates. The main part of the reequilibration takes place during the first 15 min (Figure I.5a). The variation of elevation from 15 to 45 min is reduced (± 0.25 mm; Figure I.5b), and from 45 to 210 min Δz is negligible (± 0.15 mm; Figure I.5c). The lateral gradient formed in the late phases of loading and unloading (Figure I.4b and I.5bc) is probably due to the laying and removing of the weight non exactly positioned at the center of the plate and/or disturbance by the operator's gesture.

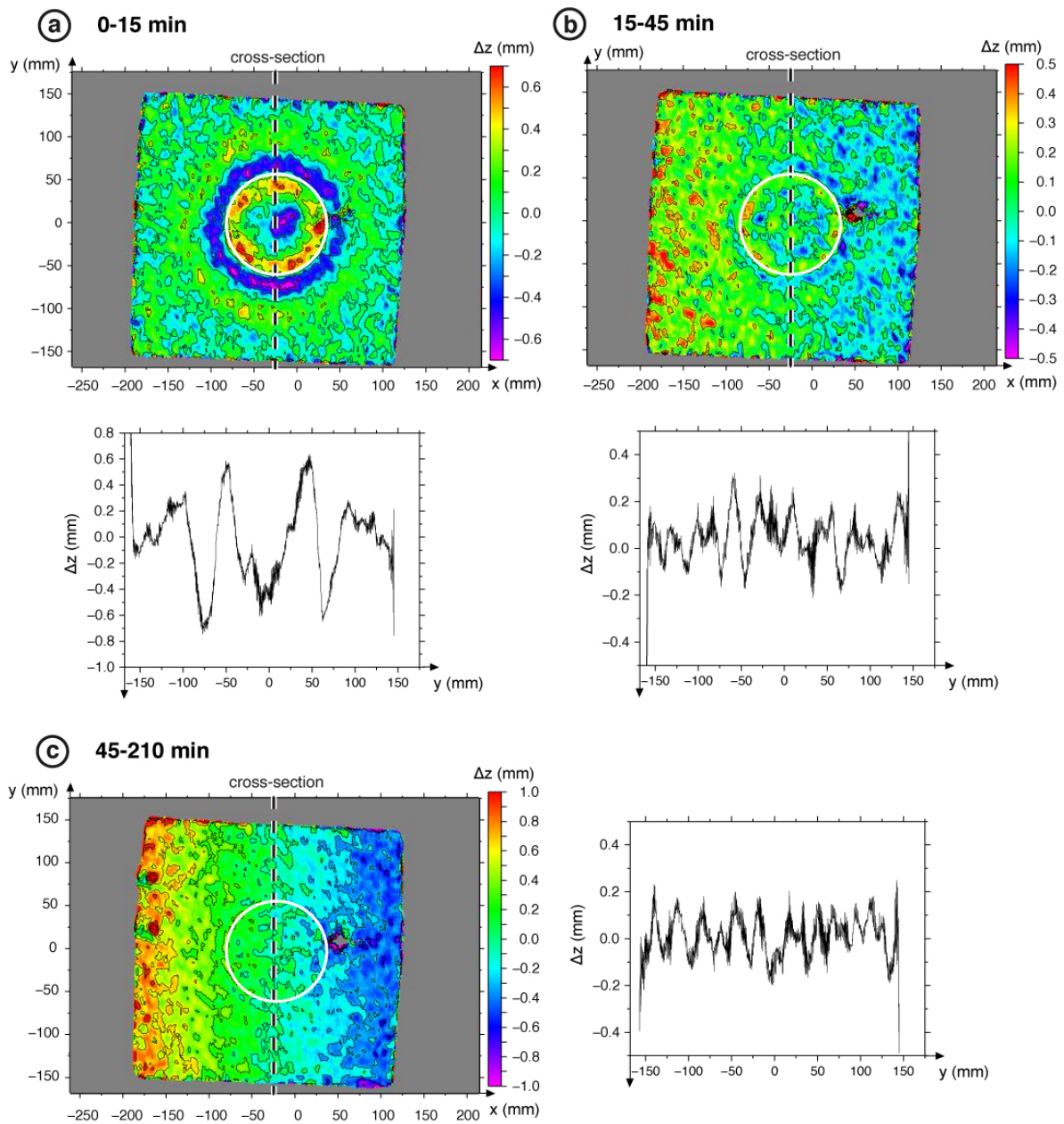


Figure I.5. Map view and corresponding cross-section (along the axe $x = -25$) of topography evolution (Δz) for the model 1 during unloading phase, (a) for the time step 0 to 15 min, (b) for time step 15 to 45 min, (c) for time step 45 to 210 min. The white circle highlights the previous position of the load.

This type of model, although made only of silicone putty, shows a non-negligible flexural response to loading/unloading processes. This suggests that the usual approximation of silicone putties behaving as Newtonian fluids [Weijermars, 1986] should be taken with caution. The main part of isostatic reequilibration occurs within 15 min (elastic response) while the last increments of deformation take one to several hours (viscous response).

3.2. Model 2: visco-elastic lithosphere, deformable load

As for the model 1, the response to loading starts as soon as we place the load and lead to the formation of a depression edged by a flexural bulge (Figure I.6a). However, the bulge surrounding the load spread over a larger area than for model 1 (larger wavelength) and is smaller in magnitude with a maximum of 0.5 mm of uplift after 10 min. Isostatic and flexural adjustments continue from 10 to 30 min with 0.2 to 0.5 mm of uplift affecting all the plate's surface (Figure I.6b).

After 30 min, we remove the load from the plate. The magnitude of the surface response is more important than for the model 1, especially just below the load with an uplift of 3.25 mm in 5 min (Figure I.7a). The flexural bulge has similar values of subsidence, but reequilibration is occurring faster than for model 1 (0.5 mm in 5 min compared to 0.6 mm in 15 min). The isostatic response decreases with time and affects only the very center of the model in the late stages (Figure I.7bc).

Compared to the first type of models, the delay between the applied stresses (loading/unloading) and the surface response is shorter. The elastic component is enhanced by the thin layer of gelatin. As for model 1, the viscous part of the response is spanning over a longer time (one to several hours).

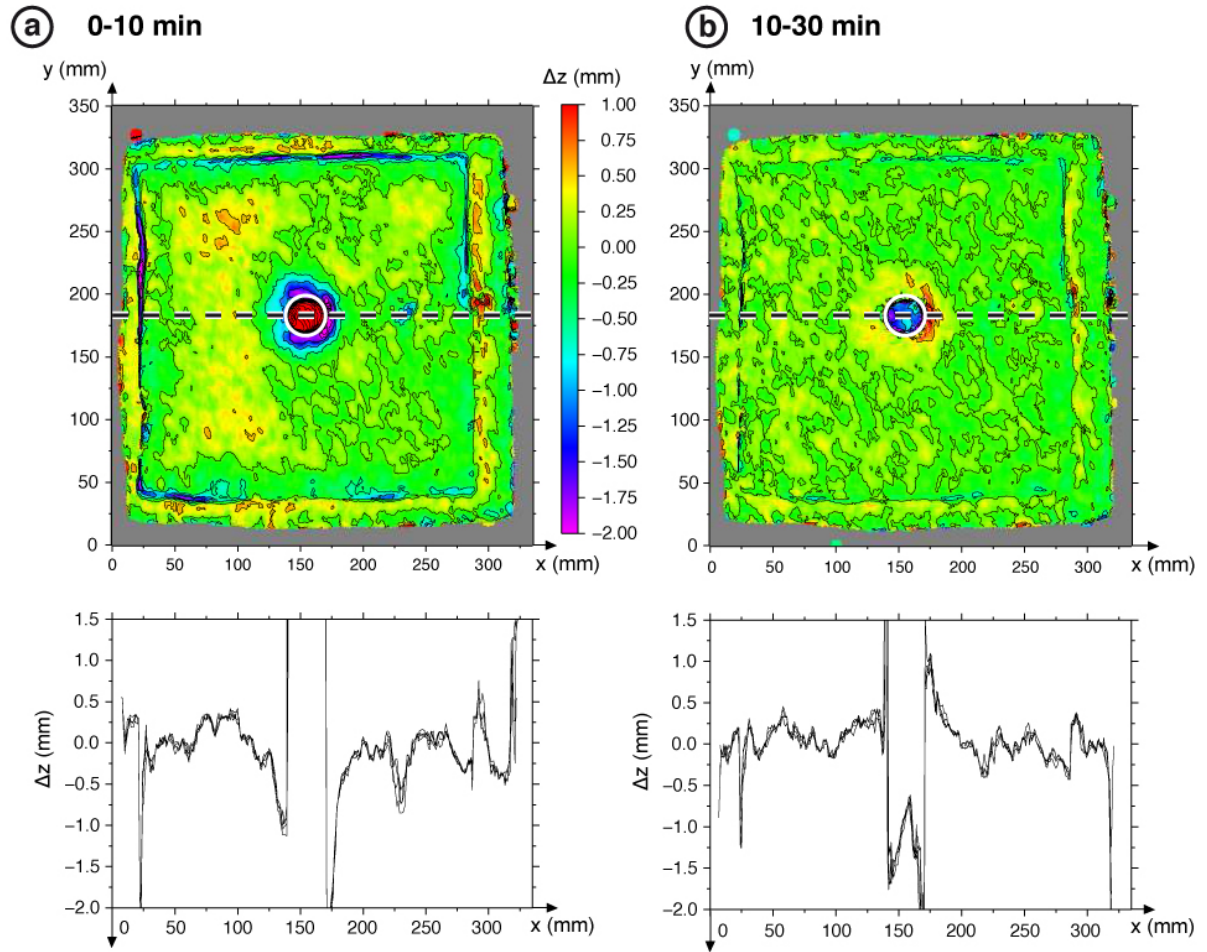


Figure I.6. Map view and corresponding cross-section (along the axe $y = -180$) of topography evolution (Δz) for the model 2 during loading phase, (a) for the time step 0 to 10 min, (b) for time step 10 to 30 min. The white circle highlights the position of the load.

Conclusions and perspectives

The use of silicone putties associated with pig skin gelatin opens new opportunities to adjust the visco-elastic properties of analog materials to natural cases. The gelatin layer increases the elastic response and shortens the delay between applied stresses and surface reequilibration. Varying the thickness of the gelatin layer and using different types of loads would allow modelers to simulate various processes implying flexure and isostatic response.

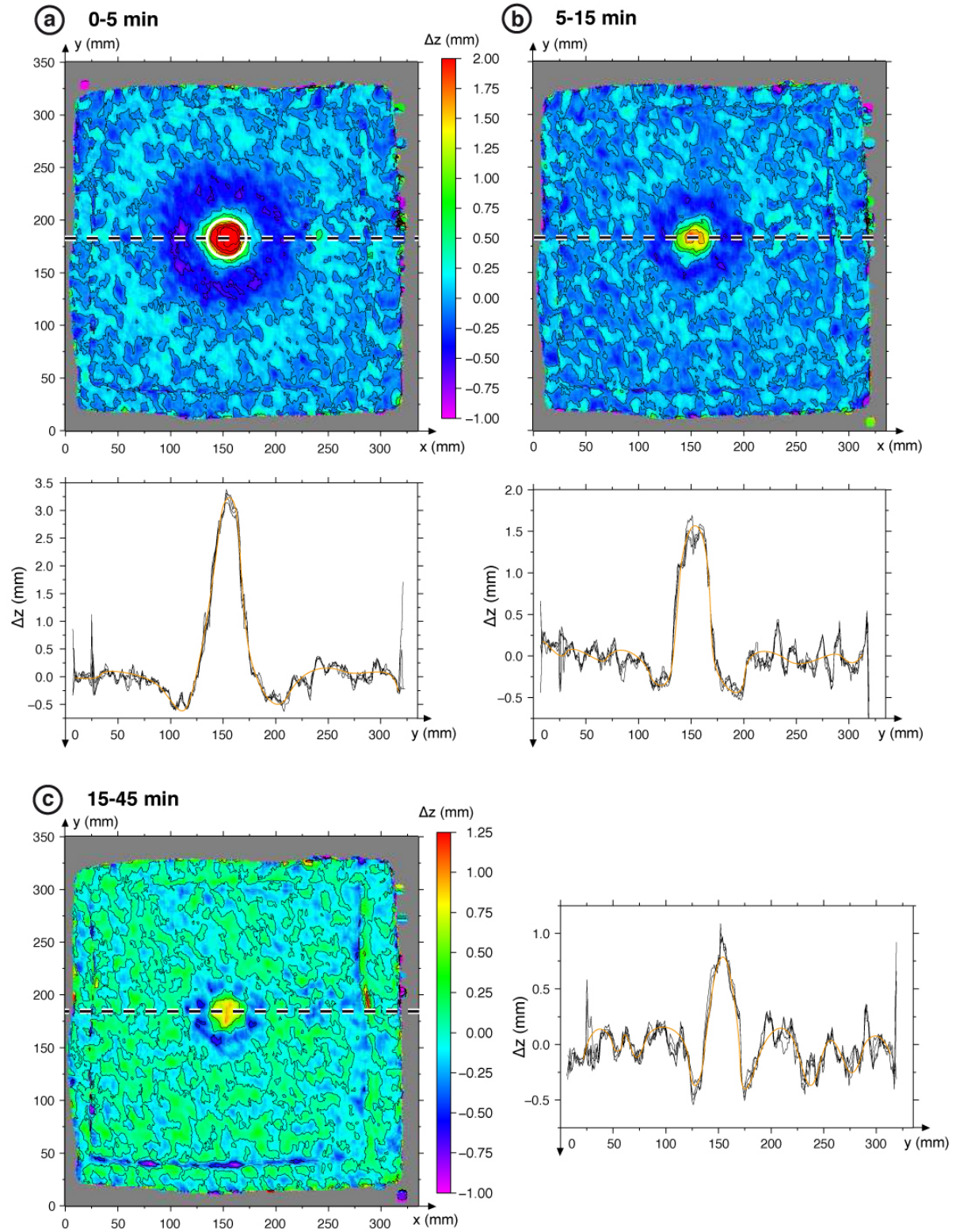


Figure I.7. Map view and corresponding cross-section (along the axe $y = 180$) of topography evolution (Δz) for the model 2 during unloading phase, (a) for the time step 0 to 5 min, (b) for time step 5 to 15 min, (c) for time step 15 to 45 min. The white circle highlights the previous position of the load.

References

Funiciello, F., C. Faccenna, D. Giardini, and K. Regenauer-Lieb (2003), Dynamic of retreating slabs: 2. Insights from three-dimensional laboratory experiments, *J. Geophys. Res.*, *108*(B4), 2207, doi:10.1029/2001JB000896.

Mezger, T.G. (2002). In: Ulrich, Zorll (Ed.), *The Rheology Handbook: For Users of Rotational and Oscillatory Rheometers*. Hannover, Germany.

Part II: Deep lithospheric loading

CONTINENTAL DELAMINATION: INSIGHTS FROM LABORATORY MODELS

Flora Bajolet^{1*}, Javier Galeano², Francesca Funiciello¹, Monica Moroni³, Ana-María Negredo⁴, Claudio Faccenna¹

(1) Dipartimento Scienze Geologiche, Università "Roma TRE", Largo S. L. Murialdo 1, 00146 Rome, Italy.

(2) Dpto. Ciencia y Tecnología Aplicadas, EUIT Agrícola, U. Politécnica de Madrid, 28040 Madrid, Spain.

(3) DICEA, Sapienza Università di Roma, via Eudossiana 18, 00184 Rome, Italy.

(4) Dpto. Física de la Tierra, Astronomía y Astrofísica I, and Instituto de Geociencias (CSIC-UCM). Facultad de Ciencias Físicas, Univ. Complutense Madrid, 28040 Madrid, Spain.

*Published in **Geochemistry, Geophysics, Geosystems** 13 (2012), Q02009*

Abstract. One of the major issues of the evolution of continental lithospheres is the detachment of the lithospheric mantle that may occur under certain conditions and its impact on the surface. In order to investigate the dynamics of continental delamination, we performed a parametric study using physically-scaled laboratory models. The adopted setup is composed of a three-layers visco-elastic body (analog for upper crust, lower crust, lithospheric mantle) locally thickened/thinned to simulate a density anomaly (lithospheric root) and an adjacent weak zone, lying on a low viscosity material simulating the asthenosphere. The results emphasize the interplay between mantle flow, deformation, surface topography and plate motion during a three-phases process: (1) a slow initiation phase controlled by coupling and bending associated with contraction and dynamic subsidence, (2) lateral propagation of the delamination alongside with extension and a complex topographic signal controlled by coupling and buoyancy, while poloidal mantle flow develops around the tip of the delaminating lithospheric mantle, and (3) a late phase characterized by a counterflow that triggers retroward motion of the whole model. A semi-quantitative study allows us to determine empirically two parameters: (1) an initiation parameter that constrains the propensity of the delamination to occur and correlates with the duration of the first stage, (2) a buoyancy parameter characterizing the delamination velocity during late stages and therefore its propensity to cease. Finally, we point out similarities and differences with the Sierra Nevada (California, USA) in terms of topography, deformation and timing of delamination.

1. Introduction

Continental delamination is presently one of the most discussed geodynamic processes due to its significant impact on the long-term behavior of the continental lithosphere. The concept of continental delamination was first introduced by *Bird* [1978, 1979], who proposed the hypothesis that along a tectonically stable area, the dense lithospheric mantle could peel away from the crust and sink into the asthenosphere. Delamination is permitted as soon as any process provides an elongated conduit connecting the underlying asthenosphere with the base of the continental crust. The delaminated mantle part of the lithosphere peels away as a coherent slice, without necessarily undergoing major internal deformation, and is replaced by buoyant asthenosphere. To avoid ambiguity, the term ‘delamination’ is used here to indicate

the process that causes the asthenosphere to come into direct contact with the crust, and the hinge of delamination, where the lithosphere peels off the overlying crust, to migrate laterally. Others processes able to remove a part of the lithosphere such as convective removal of the lithospheric mantle developing from Rayleigh-Taylor instabilities [e.g. *Houseman et al.*, 1981; *England and Houseman*, 1989] are not considered here.

Delamination has often been proposed to explain different observations such as regional uplift associated with alkaline volcanism, anomalously high heat flow and change of stress field toward extension in various geodynamic contexts: either near a plate boundary (western Mediterranean [*Channel and Mareschal*, 1989]; Alboran sea [*Seber et al.*, 1996; *Calvert et al.*, 2000; *Valera et al.*, 2008]); for intracontinental zones (Variscan belt [*Arnold et al.*, 2001]; Sierra Nevada in California [*Ducea and Saleeby*, 1998; *Zandt et al.*, 2004; *Le Pourhiet et al.*, 2006]); plateau interiors (Tibet [*Bird*, 1978]; Anatolia [*Gogus and Pysklywec*, 2008a]; Colorado [*Bird*, 1979; *Lastowka et al.*, 2001; *Levander et al.*, 2011]); or in more complex areas exhibiting unusual intermediate depth seismicity (East Carpathians [*Girbacea and Frisch*, 1998; *Knapp et al.*, 2005; *Fillerup et al.*, 2010]).

In spite of the popularity of continental delamination, its basic aspects remain poorly studied. For one part because most observables possibly indicating ongoing delamination are indirect ones (tomography, seismicity) [*Levander et al.*, 2011], and some surface features (tectonic, volcanism, topography) could be interpreted as subduction-related signals (i.e. slab roll-back, slab break-off). Moreover, few physical-numerical models have been developed [e.g. *Schott and Schmeling*, 1998; *Morency and Doin*, 2004; *Gogus and Pysklywec*, 2008b; *Valera et al.*, 2008, 2011; *Faccenda et al.*, 2009]. Although these models successfully capture the main features of delamination, they have to deal with difficulties such as numerical instabilities associated with fast deforming bodies and with strong lateral contrasts of viscosity. Unlike subduction, which has been investigated by numerous laboratory studies over the last two decades [e.g. *Jacoby*, 1980; *Kincaid and Olson*, 1987; *Griffiths et al.*, 1995; *Guillou-Frottier et al.*, 1995; *Faccenna et al.*, 1996, 1999; *Funiciello et al.*, 2003, 2004, 2008; *Schellart*, 2004), or convective removal [*Pysklywec and Cruden*, 2004] very few attempts to reproduce continental delamination with analog models have been made [*Chemenda et al.*, 2000; *Gogus et al.*, 2011].

The main purpose of this study is to investigate the dynamics of continental delamination with laboratory models exploring the influence of various parameters (initial structure, rheological properties), and the relationships between deep dynamics (i.e. mantle

circulation), surface deformation (i.e. deformation, isostatic reequilibration, dynamic topography), and plate motion.

2. Experimental Setup

Delamination is reproduced in the laboratory using a thin sheet three-layers model (lithosphere), lying on top of a low-viscosity glucose syrup simulating the asthenospheric mantle (Figure II.1). From top to bottom, the lithospheric sheet is composed of: 1) visco-elastic silicone putty simulating the upper crust, 2) high-viscosity glucose syrup simulating the viscous lower crust, 3) strong and dense visco-elastic silicone, analog of the lithospheric mantle (Table II.1). The selected asthenospheric mantle is a Newtonian fluid whose viscosity allows us to obtain laminar flow in the limit of a small Reynolds number.

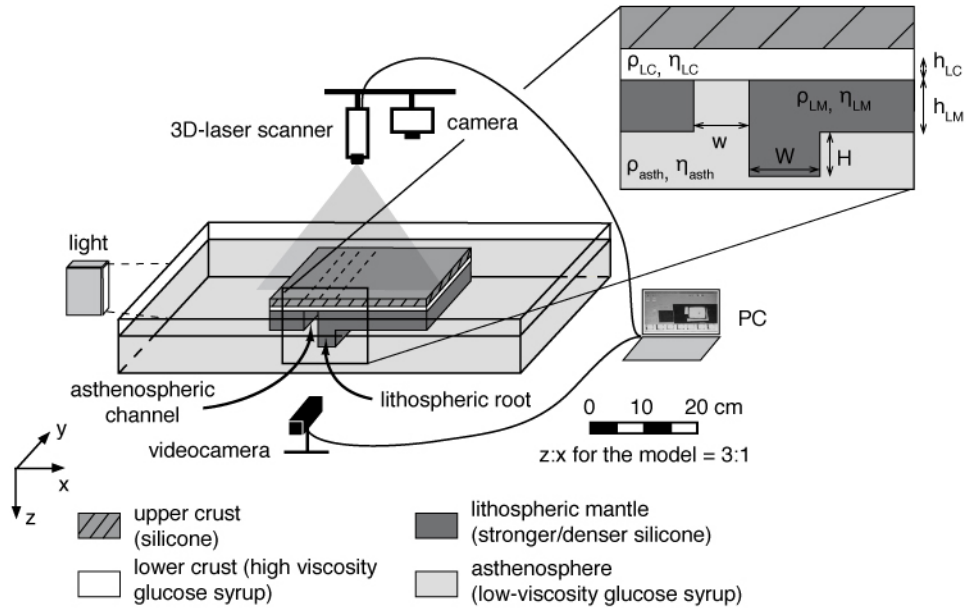


Figure II.1. Experimental setup. Material properties are given in Table II.1, and settings for each experiment in Table II.3.

The three-layered sheet is located in the center of a large Plexiglas tank (75 x 25 x 25 cm³), whose bottom mimics the 660 km discontinuity, and is free to move in all directions (free boundary conditions). The distance between the plate and box sides is set large enough to minimize possible boundary effects [Funiciello *et al.*, 2006].

Material	Density (kg m ⁻³)	Viscosity (Pa s ⁻¹)
Silicone 4 (upper crust)	1422	5.10 ⁴
Silicone 7 (lithospheric mantle)	1476	1.10 ⁵
Silicone 2 (light lithospheric mantle)	1456	6.10 ⁴
Silicone 1 (very light lithospheric mantle)	1438	7.2 x 10 ⁴
Intermediate syrup (asthenosphere)	1428	22
High viscosity syrup (lower crust)	1442	168
Very high viscosity syrup (lower crust experiment DEL23)	1455	425

Table II.1. Material properties. Viscosities are given for room temperature (22°C) and an experimental strain rate of 10^{-2} s^{-1} (scaled for nature).

This experimental setting is properly scaled for normal gravity field to simulate the competition between acting gravitational and viscous resistive forces stored within the mantle and the lithosphere [e.g. *Weijermars and Schmeling, 1986; Davy and Cobbold, 1991*]. The density and the viscosity ratios between the lithosphere and asthenosphere range between 1.01 and 1.02 and 400 and 3000, respectively. The length scale factor is fixed to 1.2×10^{-7} so that 1 cm in the models corresponds to 83 km in nature. Further details on experimental parameters and scaling relationships can be found in Table II.2. The adopted setup implies the following assumptions, and consequent limitations, that are detailed in *Funiciello et al. [2003]*: (1) isothermal system, (2) constant viscosity and density over the depth of the individual layers, (3) lack of global background mantle flow, (4) 660 km discontinuity as an impermeable barrier. In contrast with *Gogus et al. [2011]*, we do not impose any convergence, nor manually trigger initiation of delamination. Delamination is spontaneously enhanced by the adopted ad hoc initial condition which, in analogy with previous numerical models [*Schott and Schmeling, 1998; Valera et al., 2008, 2010*], includes a zone of thicker lithospheric mantle (orogenic root, 1.04 cm thick in the reference experiment) adjacent to a weak zone represented by an asthenospheric channel (absence of lithospheric mantle; Figure II.1). This configuration enables the asthenosphere upwelling to replace the delaminated lithospheric mantle. A similar setting has also been adopted in the numerical models of *Gogus and Pysklywec [2008b]*, who considered a flat geometry of the lithospheric mantle, but imposed a local density increase of 100 kg m^{-3} , producing a negative buoyancy similar to our orogenic root. The presence of a local weakened zone is fundamental to trigger delamination in nature.

This is usually explained as likely related to the presence of free water, which would decrease the pore pressure allowing a reduction in the brittle strength [Schott and Schmeling, 1998], or thermally active areas in response to active mantle upwelling. This weak zone is spontaneously created only in the model developed by Morency and Doin [2004] where strong localized thinning of the lithospheric mantle leads to the formation of an “asthenospheric conduit”.

Parameter		Nature	Model
g	Gravitational acceleration (m s^{-2})	9.81	9.81
Thickness ^a			
h_l	Continental lithosphere (m)	100000	0.012
h_{asth}	Upper mantle asthenosphere (m)	660000	0.11
Density			
ρ_l	Continental lithosphere (kg m^3)	3200	1457
ρ_{asth}	Upper mantle asthenosphere (kg m^3)	3220	1428–1442
ρ_l / ρ_{um}	Density ratio	0.99	1.02–1.01
Viscosity			
η_l	Continental lithosphere (Pa s^{-1})	10^{23}	7×10^4
η_{asth}	Upper mantle asthenosphere (Pa s^{-1})	10^{21}	22–168
η_l / η_{um}	Viscosity ratio	10^2	4×10^2 – 3×10^3
Dimensionless parameters		Equivalence model-nature	
t°	Characteristic time: ($t_{\text{model}}/t_{\text{nature}} = (\Delta\rho gh)_{\text{lith nature}} / (\Delta\rho gh)_{\text{lith model}} \times (\eta_l)_{\text{model}} / \eta_l$ nature)	4.02×10^{-12} $1 \text{ min}_{\text{model}} \rightarrow 0.473 \text{ My}_{\text{nature}}$ $1 \text{ h}_{\text{model}} \rightarrow 28.4 \text{ My}_{\text{nature}}$	
U°	Characteristic velocity: ($U_{\text{model}}/U_{\text{nature}} = t_{\text{nature}} / t_{\text{model}} \times L_{\text{model}} / L_{\text{nature}}$)	29829 $1 \text{ cm h}^{-1}_{\text{model}} \rightarrow 0.29 \text{ cm y}^{-1}_{\text{nature}}$	

^aScale factor for length $L_{\text{model}}/L_{\text{nature}} = 1.2 \times 10^{-7}$.

Table II.2. *Scaling of parameters for the reference experiment.*

Each model is monitored over its entire duration using a sequence of digital pictures taken in lateral and top views. We also record the evolution of the surface topography with a 3D-laser scanner (Real Scan USB) whose precision is 0.1 mm, corresponding to 830 m in nature. The evolution of delamination is monitored by Feature Tracking (FT) image analysis technique on representative experiments. In order to adopt the FT for our models, the glucose syrup is previously seeded with bright reflecting air micro-bubbles used as passive tracers. These bubbles have a diameter less than 1 mm, and consequently its possible influence on the density/viscosity is negligible. Images of the micro-bubbles are recorded by a CCD camera, set to acquire about 2 frames per second in lateral view. FT algorithms provide sparse velocity

vectors with application points coincident with pixel luminosity intensity gradients characterizing the passive tracers seeding the mantle. This technique permits to obtain a Lagrangian description of the observed velocity field, which is then used to reconstruct instantaneous and time-averaged Eulerian velocity maps (modulus, x-y components, streamlines) through a resampling procedure [see *Funiciello et al.*, 2006 and references therein].

3. Experimental Results

Our models were performed to provide new insights into the mechanical/dynamic behavior of the lithosphere in a delamination process. In particular, we intend to describe and quantify the spatial and temporal evolution of the mantle circulation induced by delamination and the related surface response. Fourteen models out of 26 (Table II.3) have been selected to illustrate the influence of (1) plate thickness, (2) plate viscosity, (3) plate density, (4) presence/absence/size of the asthenospheric channel, (5) presence/absence/size of the lithospheric root, (6) asthenosphere viscosity on the delamination process.

3.1. Evolution of the reference experiment (DEL 10)

All the performed experiments show a typical sequence of deformation, starting from spontaneous delamination to the arrival of lithospheric mantle to the bottom of the box. In this section, we describe the typical evolution of the delamination process as recorded for the reference model DEL10. DEL10 is characterized by thicknesses of 0.375 cm, 0.2 cm and 0.78 cm for the upper crust, the lower crust and the lithospheric mantle, respectively. It includes a zone of 1.04 cm thick lithospheric mantle simulating the orogenic root. The other parameters are listed in Table II.3. The proward direction is defined as the direction of migration of the delamination (toward the right in all the figures), and retroward direction corresponds to the opposite sense (toward the part of the model that does not delaminate, i.e. left in the figures).

Experiment	Plates (size, silicones)	Asthenospheric channel width (w)	Orogenic root width (W)	Layers thickness
DEL10	UC (sil. 4): 30 x 18 cm ² LM (sil. 7): 30 x 14 cm ²	2 cm	3 cm	UC: 0.375 cm LC: 0.2 cm LM: 0.78 cm Root: 1.04 cm
DEL11	UC (sil. 4): 30 x 18 cm ² LM (sil. 7): 30 x 14 cm ²	4 cm	3 cm	UC: 0.38 cm LC: 0.2 cm LM: 0.665 cm Root: 1.04 cm
DEL12	UC (sil. 4): 30 x 18 cm ² LM (sil. 7): 30 x 14 cm ²	2 cm	3 cm	UC: 0.37 cm LC: 0.2 cm LM: 0.775 cm Root: 0.55 cm
DEL13	UC (sil. 4): 30 x 18 cm ² LM (sil. 7): 30 x 14 cm ²	1 cm	3 cm	UC: 0.325 cm LC: 0.2 cm LM: 0.6 cm Root: 1.025 cm
DEL14	UC (sil. 4): 30 x 18 cm ² LM (sil. 7): 30 x 14 cm ²	2 cm	3 cm	UC: 0.35 cm LC: 0.4 cm LM: 0.65 cm Root: 0.975 cm
DEL15	UC (sil. 4): 30 x 18 cm ² LM (sil. 7): 30 x 14 cm ²	2 cm	1 cm	UC: 0.36 cm LC: 0.2 cm LM: 0.675 cm Root: 0.975 cm
DEL16	UC (sil. 4): 30 x 18 cm ² LM (sil. 7): 30 x 14 cm ²	2 cm	No orogenic root	UC: 0.275 cm LC: 0.2 cm LM: 0.65 cm
DEL17	UC (sil. 4): 30 x 18 cm ² LM (sil. 7): 30 x 14 cm ²	2 cm	No orogenic root	UC: 0.275 cm LC: 0.2 cm LM: 0.68 cm
DEL18	UC (sil. 4): 30 x 18 cm ² LM (sil. 1): 30 x 14 cm ²	2 cm	3 cm	UC: 0.35 cm LC: 0.2 cm LM: 0.675 cm Root: 1.0 cm
DEL19	UC (sil. 4): 30 x 18 cm ² LM (sil. 2): 30 x 14 cm ²	2 cm	3 cm	UC: 0.325 cm LC: 0.2 cm LM: 0.725 cm Root: 0.970 cm
DEL20	UC (sil. 4): 30 x 18 cm ² LM (sil. 7): 30 x 14 cm ² Asth.: high viscosity syrup	2 cm	3 cm	UC: 0.340 cm LC: 0.2 cm LM: 0.720 cm Root: 0.940 cm
DEL21	UC (sil. 4): 30 x 18 cm ² LM (sil.7): 30 x 14 cm ²	No asthenospheric channel	No orogenic root	UC: 0.40 cm LC: 0.2 cm LM: 0.730 cm
DEL22	UC (sil. 4): 30 x 18 cm ² LM (sil.7): 30 x 14 cm ²	No asthenospheric channel	3 cm	UC: 0.320 cm LC: 0.2 cm LM: 0.760 cm Root: 0.950 cm
DEL23	UC (sil. 4): 30 x 18 cm ² LM (sil.7): 30 x 14 cm ²	No asthenospheric channel	No orogenic root	UC: 0.325 cm LC: 0.2 cm very high viscosity syrup LM: 0.660 cm
DEL24	UC (sil. 4): 30 x 25 cm² LM (sil.7): 30 x 24.5 cm²	No asthenospheric channel	No orogenic root	UC: 0.350 cm LC: 0.2 cm LM: 0.770 cm

Table II.3. Experimental parameters for each experiment. UC: upper crust; LC: lower crust; LM: lithospheric mantle; Asth.: asthenosphere. Values in bold italic are the parameters

varying compared to the reference case (DEL10, highlighted in grey). In a few experiments (DEL21, 22, 23), the lithospheric mantle tends to detach from the lower crust along the borders parallel to the length of the model. This is due to the fact that in this area, the layer of lower crust is in contact with the asthenosphere, thus creating a “false” asthenospheric channel. In experiment DEL24, the layer of silicone simulating the lithospheric mantle is larger avoiding the contact. In this case, there is no delamination.

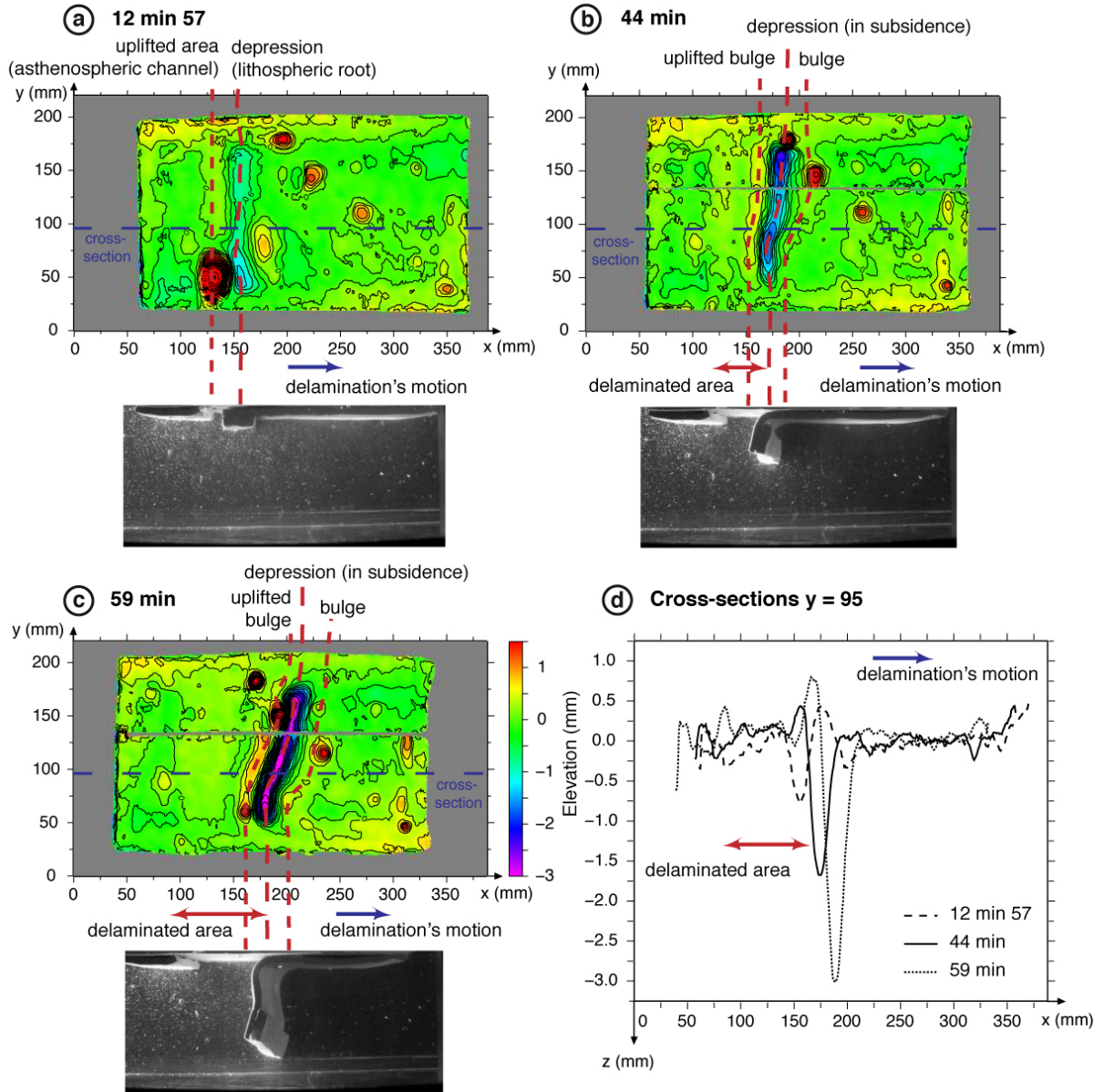


Figure II.2. Side view photos and surface topography for the reference experiment (DEL10) at three stages of the delamination process: a) 12 min 57s during initiation phase, b) 44 min at the transition between main and final phase, c) 59 min during final phase, with corresponding cross-sections (d) taken along the reference dotted blue line. The high (red)

circular zones are air bubbles trapped between the layers during the construction of the model. Later experiments free of that experimental bias showed that it does not affect significantly the delamination process.

3.1.1. Initiation of delamination

At the beginning of the experiment, the area above the asthenospheric channel is 0.1 to 0.2 mm higher than the unperturbed area due to the absence of lithospheric mantle, and the area above the lithospheric root is 0.3 mm lower (Figure II.2ad). The edge of the unstable thickened lithospheric mantle slowly starts to peel away from the overlying lower crust alongside the length of the asthenospheric channel and displaces underlying mantle material proward (Figure II.2a). The amount of time necessary to initiate this process is 30 min (corresponding to 14.2 My in nature) in the reference experiment (Table II.4). Concurrently, the difference of pressure at the base of the sinking lithospheric mantle and in the asthenospheric channel produces a clockwise return flow that injects asthenospheric material into the lower crust toward the lithospheric root. This flow remains very modest during all the initiation with a maximum velocity of 3.6 cm h^{-1} (Figure II.3a). A small amount of extension parallel to the direction of delamination affects the area above the asthenospheric channel, while the rest of the model is globally in contraction, which is stronger above the lithospheric root (Figure II.4a). The depression caused by the pull of the thickened lithospheric mantle progressively narrows and deepens up to 0.9 mm. As subsidence is deforming the model, two bulges due to bending form, one at each side of the depression (i.e. each side of the lithospheric root). They are ca. 0.1 mm higher than the average elevation of the model (Figure II.2ad). Figure II.5 shows the evolution of the elevation for the uplifted bulge located above the asthenospheric channel, and for the depression migrating with the delamination hinge. Figure II.6 shows the evolution of horizontal velocity of both the dynamic depression, that corresponds to the velocity of delamination (in the plate reference frame), and of the whole model (in a fixed external reference frame).

Experiment	Difference with reference experiment	Duration of initiation t	Duration of main phase	w_c (cm)	Duration of final stage	Root pull F_{rp} ($\times 10^{-4}$ N)	Initiation parameter I ($\times 10^{-7} s^7 m^{-3}$)	Buoyancy parameter B ($\times 10^{-10} m^4 s^4 kg^{-1}$)	Mean velocity during Stokes' phase V ($\times 10^{-5} m s^{-1}$)
DEL10	Reference experiment	30 min (14.2 My)	4 min (34 min after the beginning of the experiment) (1.9 My)	4.8	27 min (12.8 My)	11.46	6.02	6.20	6.13
DEL11	Asthenospheric channel twice wider	25 min (11.8 My)	0 (25 min)	4.6	23 min (10.9 My)	9.77	16.57	5.29	9.85
DEL12	Lithospheric root half thick	60 min (28.4 My)	24.9 min (84.9 min) (11.8 My)	4.4	18.1 min (8.6 My)	6.02	3.23	3.26	4.13
DEL13	Asthenospheric channel twice narrower	30 min (14.2 My)	17.8 min (47.8 min) (8.4 My)	4.5	22.2 min (10.5 My)	8.69	5.01	4.70	7.15
DEL14	Lower crust twice thicker	15 min (7.1 My)	5 min (20 min) (2.4 My)	4.9	14 min (6.6 My)	8.95	16.26	9.69	16.6
DEL15	Lithospheric root 3 times narrower	50 min (23.6 My)	22 min (72 min) (10.4 My)	5.1	20 min (9.5 My)	3.10	2.51	1.68	4.02
DEL16	No orogenic root	45 min (21.3 My)	26 min (71 min) (12.3 My)	Variable along the width of the model	17 min (8.0 My)				Variable along the width of the model
DEL17	No orogenic root	60 min (28.4 My)	37 min (97 min) (17.5 My)	4.7	17 min (8.0 My)				Variable along the width of the model
DEL18	Density contrast 4.8 times smaller	No delamination				1.99	0.070	1.07	
DEL19	Density contrast 2.4 times smaller	1h45 min (49.7 My)	5.5 min (110.5 min) (2.6 My)	3.7	39.5 min (18.7 My)	5.80	2.15	3.14	4.98
DEL20	Asthenosphere 10 times more viscous	2h20 min (66.2 My)	15.9 min (155.9 min) (7.5 My)	4.3	74.1 min (35.0 My)	6.77	0.30	0.48	1.87
DEL21	No asthenospheric channel, no orogenic root	Detachment by setup bias							
DEL22	No asthenospheric channel	Detachment by setup bias							
DEL23	No asthenospheric channel, no orogenic root, lower crust more viscous	Detachment by setup bias							
DEL24	No asthenospheric channel, no orogenic root, larger plates	No delamination							

(Legend on next page)

Table II.4. Characteristic values of duration and physical parameters for each experiment. Durations of characteristic phases are given in minutes with the corresponding scaled time for nature (in My). Main phase is defined as the time span between the end of initiation and the onset of retroward motion of the plate, the final phase from this change in kinematics until the DLM touches the bottom of the box. w_c is the width of the asthenospheric channel at the transition between main and final phase. For experiments DEL16 and DEL17, in the absence of lithospheric root, the shape of the delamination hinge is highly sinuous, with very variable velocities of delamination along the width of the model.

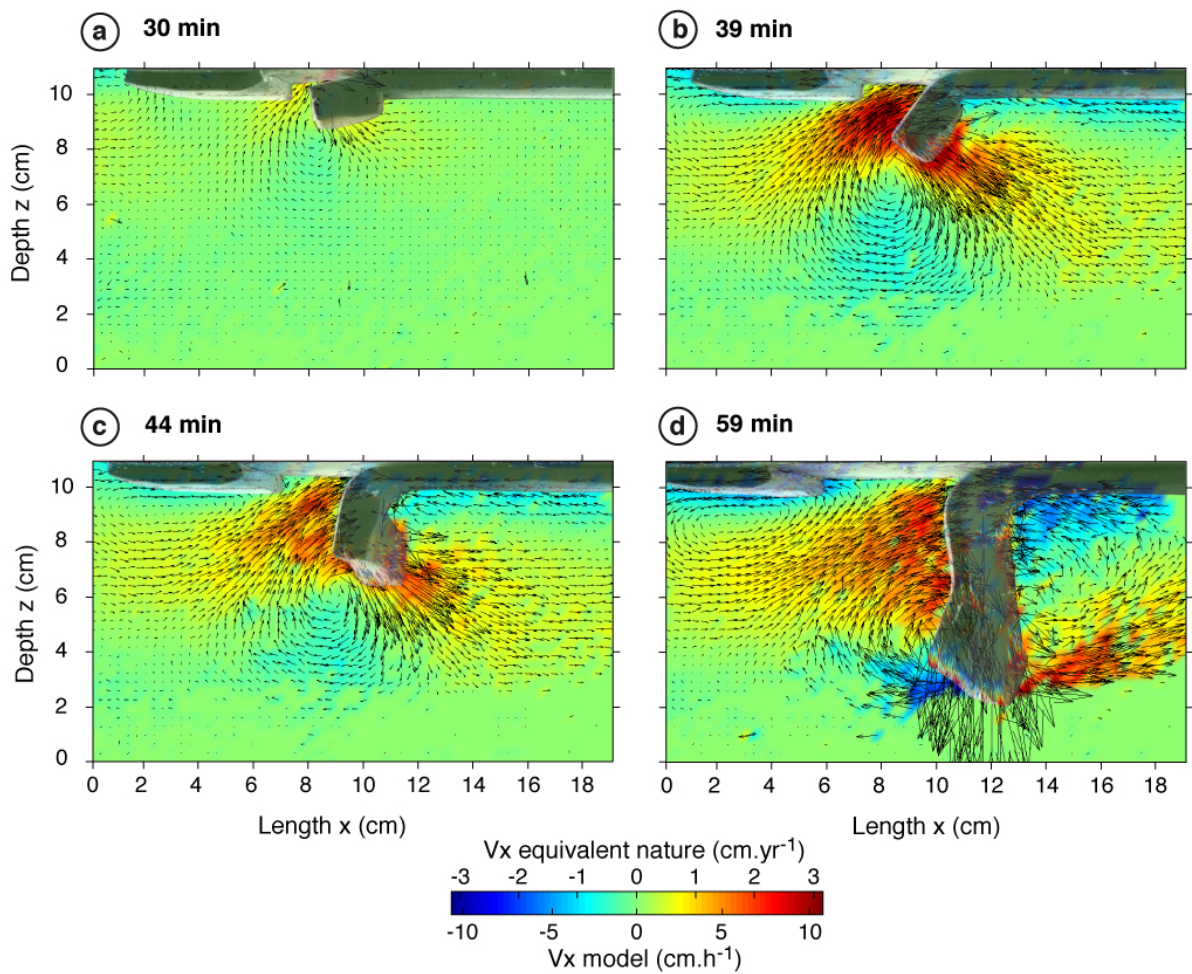


Figure II.3. Velocity field (lateral view) for experiment DEL10 at four different stages of the delamination: a) 30 min just after initiation, b) 39 min at the end of the main phase of delamination, c) 44 min at the change in dynamic with strong increase in retroward motion of the model, d) 59 min during the last phase of delamination, just before the DLM reaches the bottom of the box. Color scale represents the velocity in the x direction (length, positive in the proward direction). Shadowed images underline the position of the model.

3.1.2. Main phase of delamination

Once the lithospheric mantle decouples from the crust, the hinge of the delamination migrates progressively proward and the dip of the delaminated lithospheric mantle (DLM) increases (Figure II.3b). As the DLM rolls back in the proward direction, the poloidal clockwise flow centered beneath the tip of the slab enhances the ascent of asthenosphere, which replaces the DLM. Maximum velocities of 10.8 cm h^{-1} are reached soon after the end of the main phase, at 39 min (Figure II.3b). Sinking and proward motion of the DLM enlarge the asthenospheric channel and an ascending asthenospheric counterflow directed retroward grows (Figure II.3c). The initial topographic signal (composed of the depression flanked by the two bulges) moves laterally following the delamination's propagation with a velocity reaching 8 cm h^{-1} at 33 min (equivalent to 2.4 cm yr^{-1} in nature, Figure II.6a), and increases in amplitude. The bulge situated toward the asthenospheric channel is more uplifted than the one on the other side (reaching respectively 0.3 and 0.2 mm; Figure II.2bd) due to the impingement of the ascending asthenospheric material against the base of the crust. The increased bending of the plate causes the formation of a second area of extension above the smaller flexural bulge (Figure II.4b). The area where the lithospheric mantle is removed is also uplifted by 0.1 to 0.3 mm (Figure II.2abd). This elevated zone will remain permanently until the end of the experiment, whereas high and low areas moving with the delamination are the transient, dynamic response of the system.

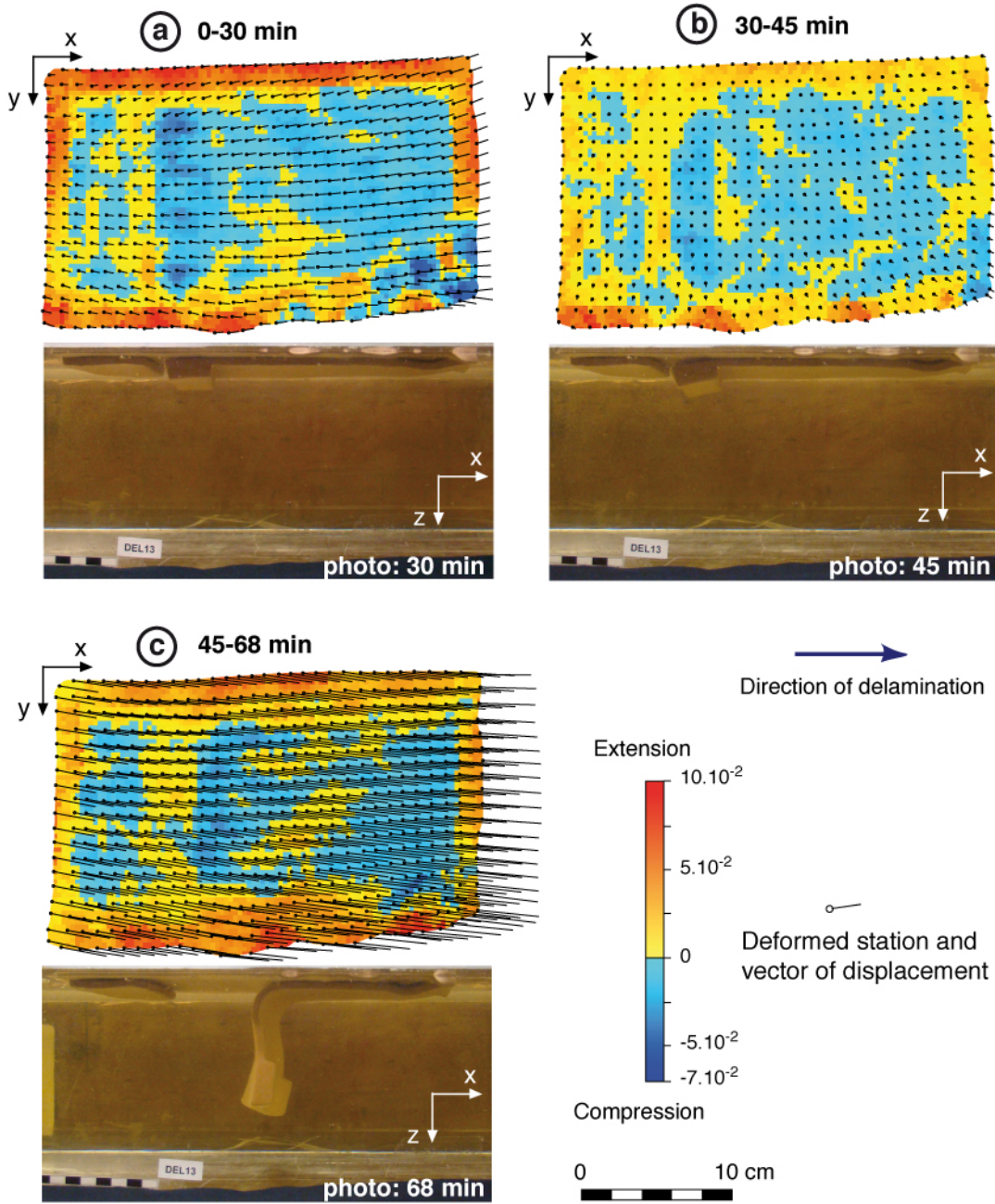


Figure II.4. 2D finite strain map of the upper crust (top view) and corresponding side view photos at 3 different stages of the delamination for experiment DEL13: a) initiation between 0 and 30 min, b) main phase between 30 and 45 min, c) final phase between 45 and 68 min. Finite strain is computed with SSPX software [Cardozo and Allmendinger, 2009]. Initial and final coordinates of reference points drawn on the upper silicone are transformed into a displacement gradient tensor from which is calculated the strain gradient tensor. The deformation field is then computed with a grid-nearest neighbor method.

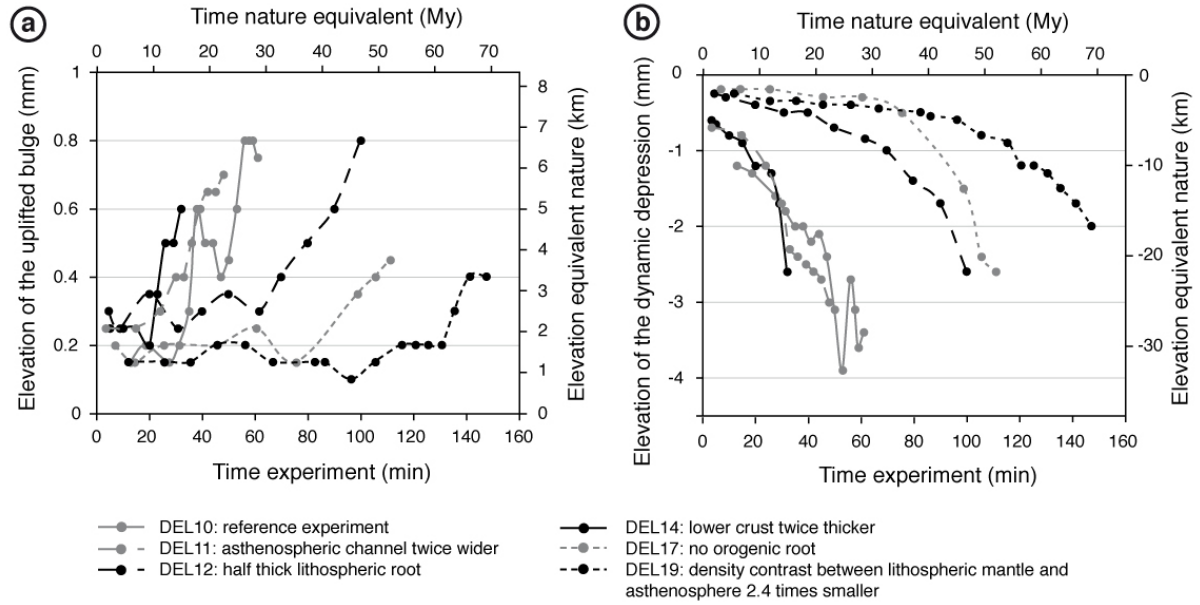


Figure II.5. Evolution through time of (a) the amplitude of elevation for the uplifted bulge and (b) depression migrating with the delamination's hinge in the plate reference frame (most significant experiments). The curves stop just before the DLM touches the bottom of the box (upper/lower mantle boundary).

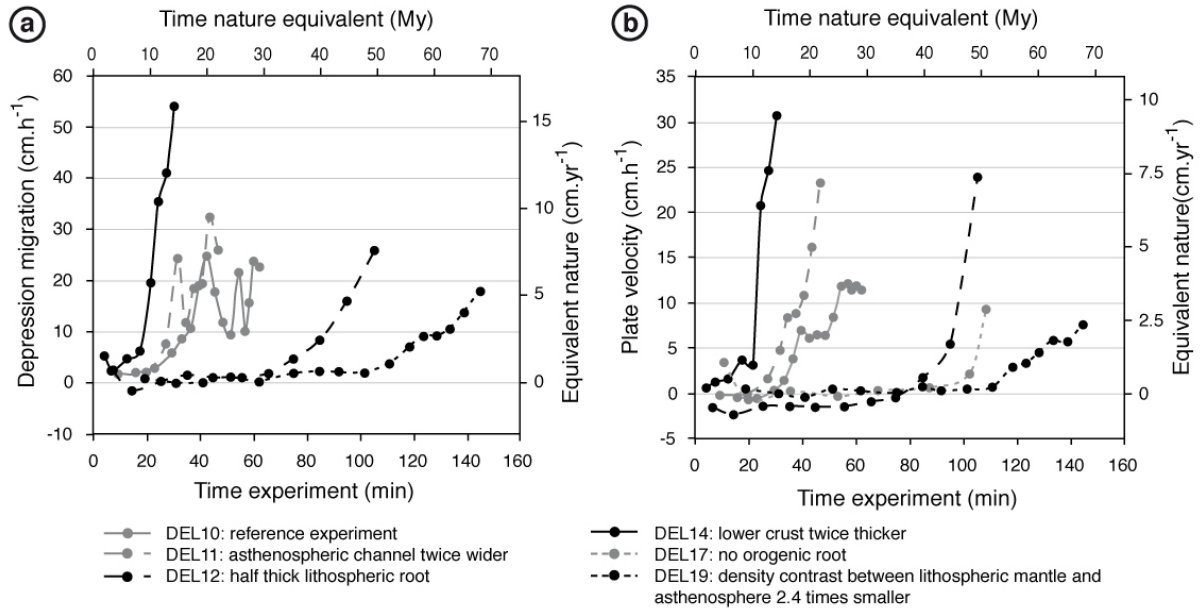


Figure II.6. Evolution of (a) the horizontal velocity of the dynamic depression in the plate referential and (b) the whole model in a fixed external reference frame. The displacement of the dynamic depression follows the delamination front and can be assimilated with the horizontal velocity of delamination. Delamination during experiment DEL17 (without

orogenic root) is very irregular and it is therefore difficult to measure the displacement of the dynamic depression at the delamination's hinge.

3.1.3. Final stage

Around 4 min after delamination initiation, i.e. 34 min after the beginning of the experiment, the width of the delaminated area reaches a critical value of ca. 4.5 cm (Table II.4). The pull induced by the DLM triggers the rapid retroward motion of the plate that sharply accelerates up to 12 cm h^{-1} at the end of the experiment (3.5 cm yr^{-1} in nature, Figure II.6b), and enhances the efficiency of the asthenospheric counterclockwise flow (Figure II.3b). The DLM's proward motion stops although delamination proceeds: the DLM roughly remains in a fixed position with respect to an external fixed reference frame, and delaminates near vertically. The mantle circulation associated with this final stage is thus characterized by the coeval flow of two advection cells, a clockwise cell to the left of DLM and a counterclockwise cell to the right (counterflow).

Consequently to the near-vertical position of the DLM, the hinge of delamination, the associated surface deformation and the topographic signal also remain fixed with respect to an external reference frame. However, they still move proward in the plate's reference frame, with a maximum velocity of 23 cm h^{-1} at the end of the experiment (6.8 cm yr^{-1} in nature, Figure II.6a). Increase in amplitude of both the depression and uplifted bulge continues until the DLM approaches the bottom of the box (Figures II.2cd and II.5). Similarly, the surface above the delaminated area continues to widen and uplift up to 0.2 to 0.3 mm as previously (Figure II.2d). Zones of extension (associated with both bulges) and contraction (associated with the dynamic depression) follow the delamination's hinge as elastic deformation. The resulting finite deformation for the whole duration of the final phase shows widening of extension both above the delaminated area and the flexural bulge. However, approximately half the delaminated area has undergone finite compression (Figure II.4c). A part of the deformation is elastic and thus transient, but the model is also durably deformed with 6% of shortening accumulated in the whole lithosphere at the end of the experiment.

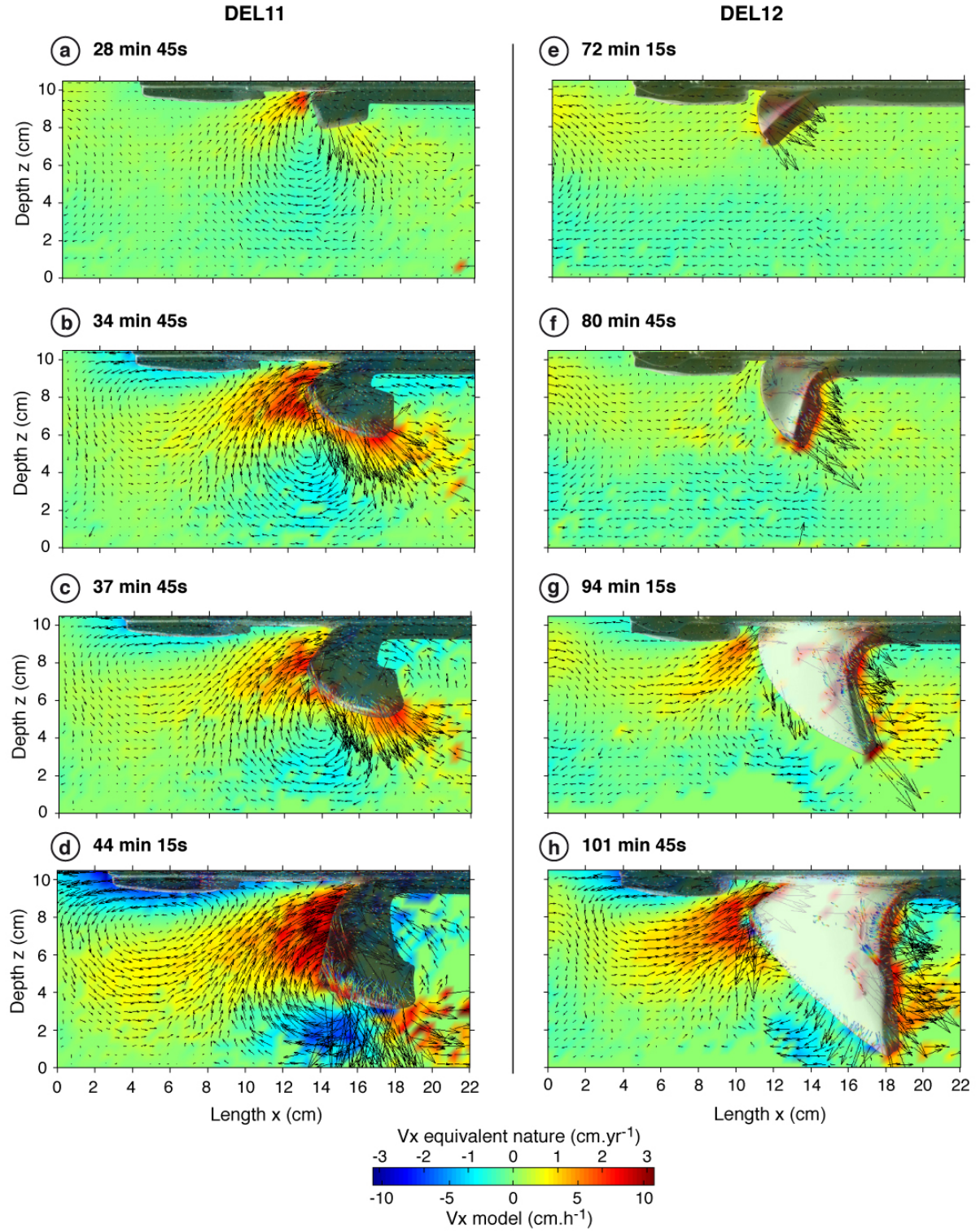


Figure II.7. Velocity field for experiment DEL11 (a-d) and DEL12 (e-h) presented as for Figure II.3 (see caption).

3.2. Sensitivity analysis

We performed a parametric study to test how the initial geometrical configuration and rheological properties of the lithosphere can influence the evolution of delamination. The main features characterizing the delamination process are invariant for all the experiments, but the timescale, mantle flow velocity and amplitude of the surface features depend on the adopted parameters.

Key parameters determining the occurrence and timing of the first phase of delamination are the thickness of the lower crust (i.e. degree of coupling between lower crust and lithospheric mantle), and the width of the asthenospheric channel. Delamination starts earlier and proceeds faster when the lower crust is thicker, and/or the asthenospheric channel is wider (compare in Figures II.5 and II.6 DEL10 with DEL11 and DEL14, Table II.4). Thickness of the orogenic root, alongside with density contrast between the lithospheric mantle and asthenosphere has also an impact on delamination velocity, especially in the initiation phase (compare in Figures II.5 and II.6 DEL10 and DEL19, Table II.4). If the density contrast is very small ($<7 \text{ kg m}^{-3}$), the delamination does not initiate (Table II.3, DEL18 not detailed here). A viscosity contrast one order of magnitude lower slows down the whole process, initiation as well as main and final phases of delamination (Tables II.3 and II.4, DEL20 not detailed here).

Although the global pattern of mantle flow is stable whatever the parameters are, the timing of the different phases and flow velocities vary. If the asthenospheric channel is initially two times larger (4 cm instead of 2 cm, DEL 11, Figure II.7a), delamination is slightly faster during the whole modeling evolution (Table II.4). More precisely, mantle flow is slower during the main phase of delamination (with a maximum of 8.1 cm h^{-1} against 10.8 cm h^{-1} for reference experiment; Figure II.7b), followed by a faster final phase (9 cm h^{-1} against 7.2 cm h^{-1} , Figure II.7d). When the orogenic root is half thick (0.55 cm instead of 1.04 cm, DEL12, Figure II.7e to h), we do not observe clear distinct phases but rather a continuous increase in flow velocity, more significant after the retroward plate motion has started (Figure II.7gh). However, this result must be taken with caution given that in this experiment, the delamination front is twisted and does not allow a good view for mantle flow record.

The topographic signal results from the interplay between different parameters, with a dominant role played by the gravitational instability of the lithospheric root. The amplitude of the topography (both for the depression and the uplifted bulge) is higher for a thick and dense lithospheric root, which therefore creates a stronger relief (Figure II.5, compare DEL10, DEL12, DEL 17 and DEL 19). On the contrary, a lower viscosity contrast between

lithosphere and asthenosphere results in lower amplitude of topography (Table II.3, DEL20 not detailed here).

Geometry and propagation of delamination is controlled by the presence/absence and size of the orogenic root. In experiments where the lithospheric root is absent (Table II.3 and Figure II.5, DEL17 and DEL16, not detailed here), delamination begins strongly delocalized along the asthenospheric channel and, afterwards, irregularly propagates in several directions. As a consequence, the topographic signal following the delamination is also heterogeneous in shape and amplitude.

4. Discussion

All the parameters discussed below are listed with symbols and units in section 8.

4.1. Forces at work during delamination

A typical feature of delamination, compared to convective removal, is that the lithospheric mantle delaminates coherently, with little internal deformation and with a geometry comparable to that of a subducting lithosphere. Thus, the following analysis of forces acting during the delamination process is partly inferred from previous studies on subduction [e.g. *Forsyth and Uyeda*, 1975; *Turcotte and Schubert*, 1982; *Conrad and Hager*, 1999; *Funiciello et al.*, 2003; *Lallemand et al.*, 2008].

The main driving force is the gravitational instability generated by the presence of the lithospheric root that progressively pulls down the lithospheric mantle. The root pull (F_{rp}) increases with time as more lithospheric mantle is delaminated. In analogy with the slab pull [e.g. *Forsyth and Uyeda*, 1975; *McKenzie*, 1977; *Davies*, 1980], our root pull force can be expressed as

$$F_{rp} = \Delta \rho g h_{LM} W H \quad (1)$$

where $\Delta \rho$ is the density contrast between the lithospheric mantle and the asthenosphere, g the gravity acceleration, h_{LM} is the thickness of the delaminated lithospheric mantle and W and H the width and thickness of the lithospheric root respectively.

The resisting forces include the shear resistance at the lower crust/lithospheric mantle boundary, the bending resistance, and the asthenosphere resistance at the interface with the DLM. First, the lithospheric mantle has to overcome the coupling (i.e. the shear resistance) with the lower crust. The shear stress at the base of the lower crust τ_{LC} is proportional to the shear rate $\dot{\gamma}$ and the viscosity of the lower crust η_{LC} ,

$$\tau_{LC} = \dot{\gamma} \eta_{LC} \quad (2)$$

The lower crust deforms by a combination of Couette and Poiseuille flow. However, side view photos show a pattern closer to Couette flow's geometry at the base of the lower crust, consistent with the deformation observed in numerical models [Le Pourhiet *et al.*, 2006]. Therefore, we will approximate the shear rate at the first order as Couette flow in a Newtonian fluid so that

$$\dot{\gamma} = v/h_{LC} \quad (3)$$

where v is the velocity in the lower crust and h_{LC} its thickness. Expressions (2) and (3) give

$$\tau_{LC} = v \eta_{LC}/h_{LC} \quad (4)$$

The delamination process requires bending of the lithospheric mantle. Following *Turcotte and Schubert* [1982], the force necessary to bend a viscous layer can be approximated by

$$R_b \approx V_d h_{LM}^3 \eta_{LM} / r^3 \quad (5)$$

where V_d is the velocity of delamination, η_{LM} and r the viscosity and radius of curvature of the lithospheric mantle respectively.

The displaced asthenosphere also exerts a viscous resistance on the DLM at its interface. For subduction, this resistance has been solved with fluid dynamics equations for the case of a stationary slab [Turcotte and Schubert, 1982]. Following the simplification adopted by *Funiciello et al.* [2003], we will only estimate the order of magnitude. At the first order, the viscous shear resistance is proportional to the asthenosphere viscosity η_{asth} and velocity of delamination V_d

$$R_{asth} \propto \eta_{asth} V_d \quad (6)$$

Acceleration of delamination with time implies a faster increase of the driving force (root pull) compared to the resisting forces. Indeed, the bending resistance decreases rapidly as it is inversely proportional to the cube of the radius of curvature expressed as the deviation of the initial straight shape. The shear resistance at the base of the lower crust and the viscous resistance of the asthenosphere, though increasing with the velocity in the lower crust and the velocity of delamination respectively, do not compensate for the augmentation of the root pull force. In the following section, we examine the evolution of the forces at work with time and their influence on the observables (timing, velocities, topography) and attempt to further quantify the delamination process.

4.2. Dynamics of delamination and surface response

The initial configuration is unstable due to the negative buoyancy of the lithospheric mantle. Conditions for initiation include a sufficient root pull: if $F_{rp} < 2 \times 10^{-4}$ N (experiment DEL18) the process does not start within the time span tested in laboratory (4 hours equivalent to 113.5 My). The mantle flow generated in the asthenospheric channel is very modest and is due to the difference of pressure between the asthenospheric channel and the base of the heavy lithospheric root. Injection of asthenospheric material at the extremity of the lithospheric root causes a viscosity decrease in the area previously occupied by the lower crust. Progressive sinking of the root enlarges the conduit. Consequently, the shear resistance τ_{LC} (equation 4) is reduced with relative increase of the root pull force's efficiency. This is indeed confirmed in experiment DEL14: when the lower crust is twice thicker, the time required for initiation is twice shorter (Table II.4, Figures II.5 and II.6). A wider asthenospheric channel (DEL11) allows for a stronger initial mantle flow that also reduces slightly the duration of initiation phase (Table II.4, Figures II.5 and II.6). In order to determine the main parameters controlling the initiation phase, we consider two parameters: the ratio T° between the time required for initiation (t) and the total duration of the experiment (T):

$$T^\circ = t/T \quad (7)$$

and an initiation parameter (I) representing the ratio of driving forces over resisting forces acting during initiation such as

$$I = F_{rp}/\tau_{LC}R_bR_{asth} \quad (8)$$

I will successfully represent the possibility for delamination to initiate if it correlates well with T° . We can therefore try to adjust its expression empirically. In equations (4), (5) and (6), we observe that τ_{LC} , R_b and R_{asth} are proportional to η_{LC}/h_{LC} , η_{asth} and $h_{LM}^3\eta_{LM}$, respectively, then

$$I \propto F_{rp}h_{LC}/\eta_{LC}\eta_{asth}h_{LM}^3\eta_{LM} \quad (9)$$

Moreover, the width of the asthenospheric channel, not taken into account in the force balance analysis, is a parameter enhancing the velocity of the initiation phase and hence can be placed at the numerator. The best fit between I and T° is obtained by adding a factor $\Delta\rho^2$ that highlights the strong dependency of the initiation duration on the density contrast so that

$$I \propto F_{rp}\Delta\rho^2h_{LC}w/\eta_{LC}\eta_{asth}h_{LM}^3\eta_{LM} \quad (10)$$

Figure II.8 shows a good linearly inverse correlation between I and T° , highlighting how I and, in turn, the interplay between its constitutive parameters, reasonably characterizes the possibility for the delamination to initiate.

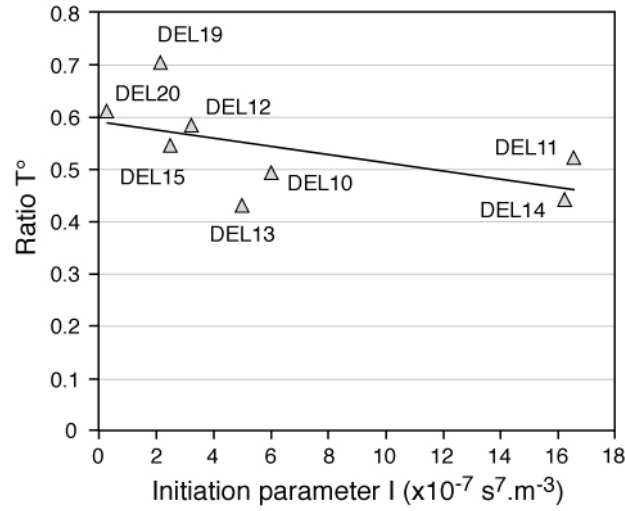


Figure II.8. Plot of the initiation parameter (I) versus the ratio between the time required for initiation of delamination and the total duration of the experiment (T°) with best fit regression line. The regression coefficient is -7.9×10^4 .

At the onset of the experiments, the zone above the asthenospheric channel undergoes fast isostatic reequilibration and is uplifted due to the absence of lithospheric mantle. The observed initial value of this uplifted zone ranges between 0.1 and 0.3 mm (corresponding to 0.6 to 1.8 km) and reasonably fits the prediction by Airy model (i.e. 0.24 mm; Figure II.2a). The depression above the lithospheric root has also a flexural bending component, as the upper and lower crusts are deflected downward by the root pull (dynamic effect). Once decoupling has started, the DLM bends preferentially in the region just behind the lithospheric root, where the resistance is smaller. Indeed, the bending resistance increases as the cube of the thickness (equation 5), preventing any important bending of the lithospheric root. Finally, the increase of the root pull force becomes high enough to control the system dynamics. The transition between the bending-dominated phase and the root pull-dominated phase is easily identifiable by plotting the vertical position and velocity of the tip of the DLM against time (Figure II.9). At some point, the vertical velocity increases almost linearly with time, adopting a Stokes flow-like law, also observed in numerical simulations [Le Pourhiet *et al.*, 2006] (Figure II.9b). The predominance of the root pull force can be further verified by comparing the mean vertical velocity during this period to a buoyancy parameter, B , (Figure II.10) defined as

$$B = F_{rp}/\tau_{LC}R_{asth} \quad (11)$$

that we simplify, in the same way as for I , as

$$B \propto F_{rp}h_{LC}/\eta_{LC}\eta_{asth} \quad (12)$$

B includes the root pull force over the asthenosphere viscosity, characteristic of a Stokes sinker. However, the good correlation between B and the mean vertical velocity (Figure II.9) is obtained only introducing the ratio of lower crust thickness over its viscosity, proportional to the shear resistance τ_{LC} . This implies that the coupling between the lower crust and the lithospheric mantle remains a determining force all along the delamination process.

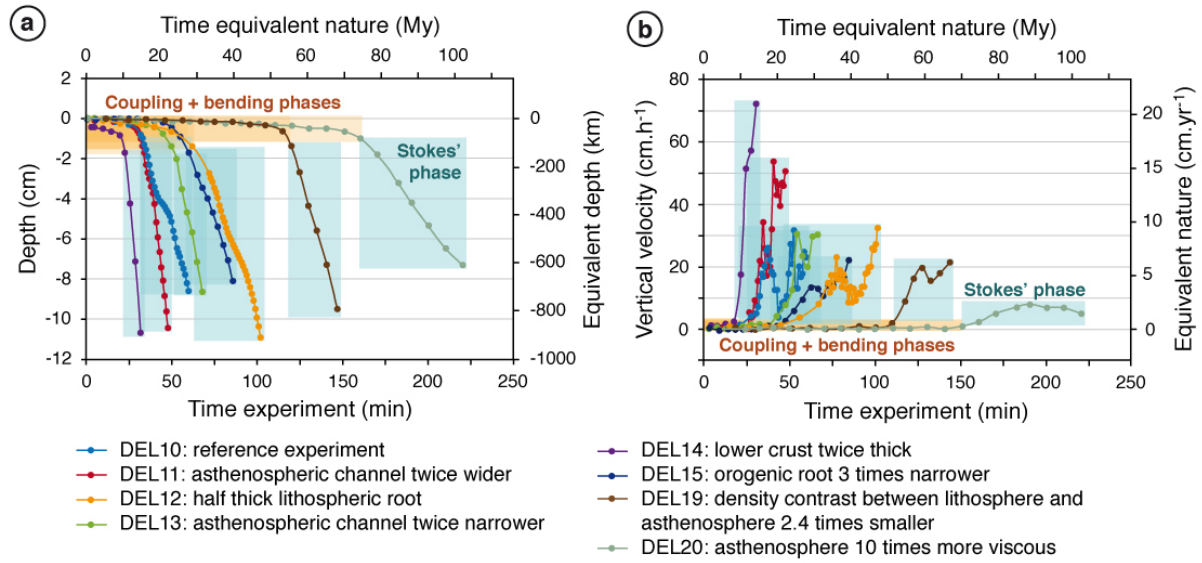


Figure II.9. Evolution of (a) the vertical position and (b) vertical velocity of the tip of the DLM through time. First stages dominated by coupling and bending are highlighted in orange, last stage dominated by root pull and characterized by a sinking similar to Stokes flow law is highlighted in blue. Curves stop just before the DLM touches the bottom of the box (upper/lower mantle boundary). The slight decrease of the vertical velocity visible on a few curves (b) is due to transitory periods of uneven delamination (lateral variations, with one side delaminating faster than the other).

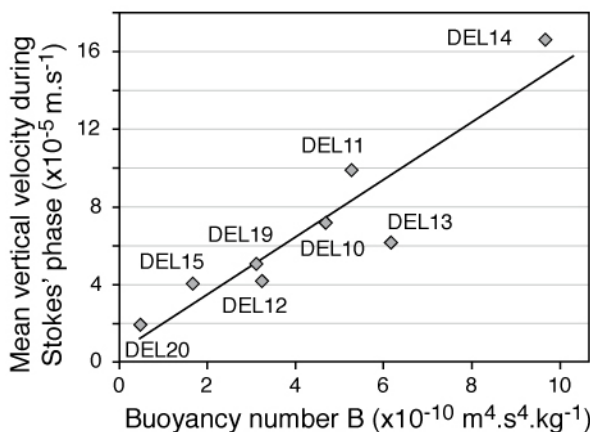


Figure II.10. Graph highlighting the correlation between the mean vertical velocity during Stokes' phase (V) and the buoyancy parameter (B) (root-pull dominated phase) with best fit regression line. The regression coefficient is 57.6.

Concurrently to the delamination acceleration, the amount of subsidence progressively increases and the maximum locus of depression migrates laterally following the delamination hinge motion (Figure II.2bc). This observable shows that a large part of the recorded topographic signal can be attributed to dynamic topography. The mantle flow also speeds up, generating fast asthenospheric upwelling. Therefore, there is a positive feedback between the induced mantle circulation and sinking of the DLM (progression of the delamination). The ascending asthenospheric flow is also responsible for the larger uplift of the bulge flanking the retroward side of the dynamic depression, with an elevation up to 0.7 mm higher than the proward bulge, which is only generated by bending (Figures II.2cd and II.11). Uplift of the delaminated area is thus partly isostatic (as observed at the beginning of experiments above the initial asthenospheric channel), and partly dynamically supported by the mantle flow.

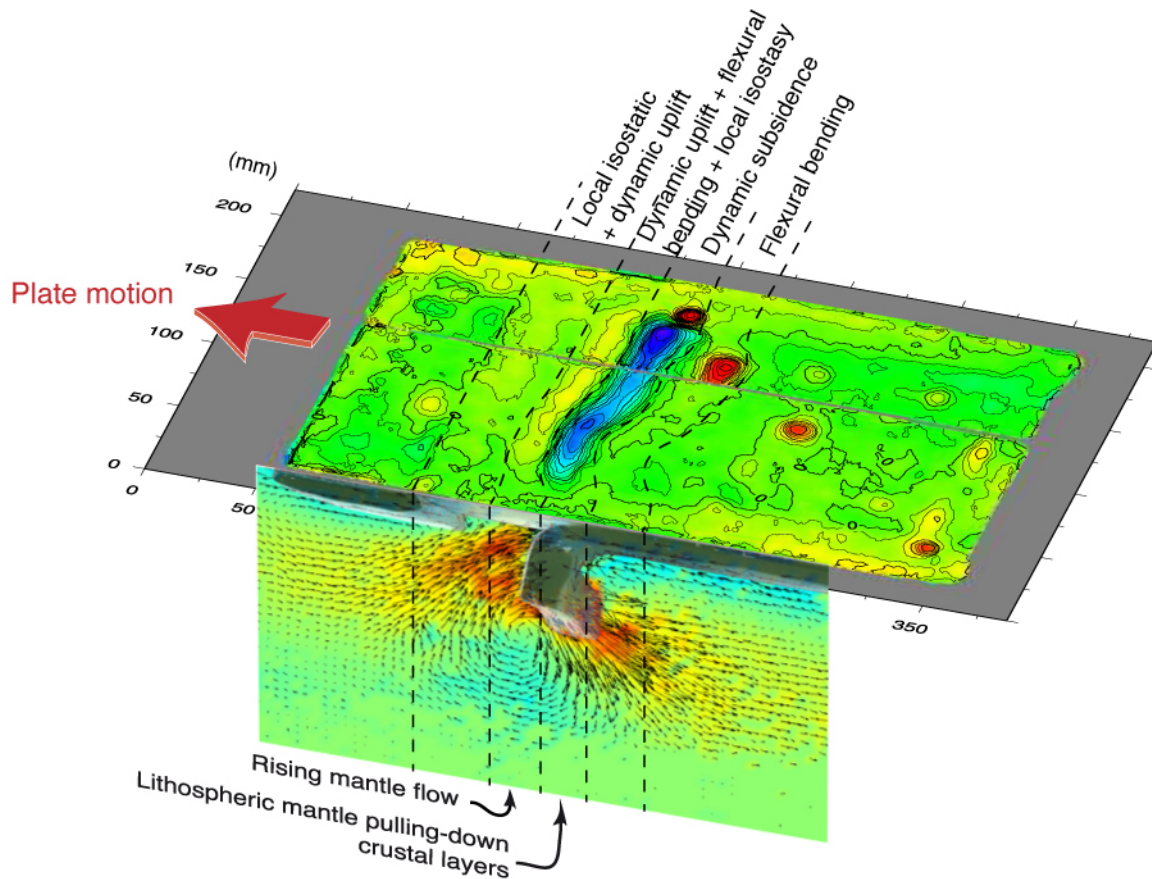


Figure II.11. Reconstruction of the relationships between mantle flow and surface topography during delamination (reference experiment DEL10 at 18 min 40s).

In summary, velocity of propagation, amplitude of the dynamic topography and plate motion are correlated with delamination hinge motion (Figures II.5 and II.6) and with sinking of the DLM, and, therefore, with mantle flow velocity. The initiation phase is mainly controlled by the density contrast between the DLM and asthenosphere (equation 10), the shear resistance at the base of the lower crust, the bending resistance and width of the asthenospheric channel. During the main phase, slow migration of the delamination front starts with active poloidal flow (Figures II.3, II.6a and II.9). The onset of the final phase can be defined when the delaminated area reaches a critical value of ~ 4.5 cm. The counterflow triggers rapid plate motion and faster delamination, correlated with strong increase of dynamic topography (Table II.4, Figures II.5, II.6 and II.11). Ultimately, delamination is controlled by buoyancy force and shear resistance, close to a Stokes sinker behavior. The transition between initiation (characterized by parameter I) and Stokes phases (characterized by parameter B) can occur either during main or final phase (Figure II.9).

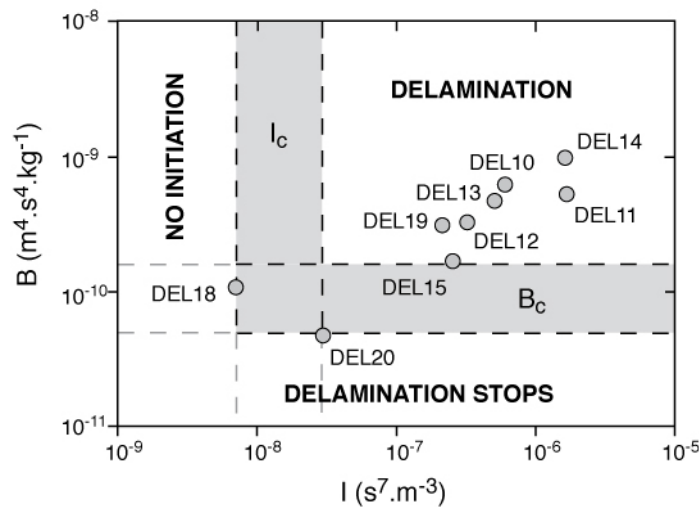


Figure II.12. Plot of the initiation parameter (I) versus the buoyancy parameter (B). Domains where delamination does not occur, stops during the process, or continues are constrained by experiments DEL18, DEL20, and DEL15. Shaded areas represent the uncertainties on the critical values I_c and B_c delimiting the different domains.

One may restrict the conditions required for delamination by plotting B versus I (Figure II.12). If I is too small, delamination will not start (experiment DEL18). Moreover, in a natural system, we expect the process to freeze if the motion is too slow (i.e. if B is too small)

event though initiation was possible. Most probably, the velocity of delamination in experiment DEL20 is too low to be sustained in a real convective-advective system, as heat transport will be faster than material motion. We can define a range for the critical values of I and B below which delamination will not start (I_c) or will stop (B_c). We find $6.99 \times 10^{-9} < I_c < 2.97 \times 10^{-8}$ and $4.80 \times 10^{-11} < B_c < 1.68 \times 10^{-10}$ (Figure II.12). The visco-elastic behavior of our analog materials rules out the possibility for break-off of the DLM. However, detachment of the root and/or part of the DLM will reduce the root pull force and could also cause cessation of the delamination.

4.3. Comparison with previous modeling results

Numerical studies dealing with delamination introduced the calculation of the topographic response using a wide range of approaches. *Bird and Baumgardner* [1981] introduced the calculated dynamic pressure in the equation of elastic bending of the crust. *Schott and Schmeling* [1998] computed the topography calculating the vertical normal stresses exerted on the model surface. *Gogus and Pysklywec* [2008b] included a free top surface, where topography develops as the model evolves. And, finally, *Valera et al.* [2011] introduced a thin upper layer of low density and viscosity to allow the top of the crust to behave as a free surface. The results of our laboratory models are reasonably comparable to the numerical models by *Gogus and Pysklywec* [2008b] because in both cases a significant amount of lateral migration of the delamination hinge is reproduced, whereas the other studies predict small to moderate (less than about 400 km) hinge migration.

The typical signal characterized by the migrating pattern of subsidence and uplift - the former caused by the sinking of the delaminated lithospheric mantle, the latter due to asthenospheric upwelling - is consistently reproduced in both numerical and laboratory approaches. However, in *Gogus and Pysklywec* [2008b] the amplitude of the highest bulge is smaller than in our experiments. This can be explained as their weak zone consists of normally buoyant lithospheric mantle, which acts as a barrier and slows down the ascent of asthenosphere. On the contrary, the buoyant “asthenospheric conduit” introduced in our setup enables the direct impingement of the asthenosphere into the base of the crust. In both *Gogus and Pysklywec* [2008b] and our models a high amplitude of the negative deflection is obtained, related to the extra negative buoyancy imposed to initiate the delamination process. In contrast, the models by *Schott and Schmeling* [1998] and *Valera et al.* [2008, 2011] predict a much smaller long-term subsidence because DLM buoyancy, which is only thermally induced, diminishes with time as heated from thermal diffusion. *Valera et al.* [2011] highlight

the sensitivity to the initial crustal structure and show that in some cases of initially orogenic crust, the sinking of DLM drags down the lower crust so that the positively buoyant thickened crust locally overcomes the effect of negative buoyancy of DLM, resulting in overall surface uplift. In our experiments, the lower crust acting as a decoupling layer is partly dragged downward into the asthenosphere alongside with the DLM, while another part remains in place beneath the upper crust. The interface between the remaining lower crust and the asthenosphere is very irregular, probably disturbed by the mantle flow. For natural systems, the dragged down lower crust is expected to later partially melt and mix with the asthenosphere.

Concerning the velocity of delamination, our estimated value of 4 cm yr^{-1} for the reference experiment (ranging from 0.7 to 14.6 cm yr^{-1} in others experiments), is consistent with the range of 0.3 to 8.0 cm yr^{-1} obtained by *Bird and Baumgardner* [1981] for a mantle of viscosity $10^{21} \text{ Pa s}^{-1}$. *Morency and Doin* [2004] found similar values, with a velocity larger than 10 cm yr^{-1} for a 590 km long sinking DLM and an asthenospheric viscosity of $10^{19} \text{ Pa s}^{-1}$. Our purely dynamic experiments likely lead to overestimated values of delamination velocities, amplitude of topographic response and width of the delaminated area, because thermal diffusion is not included [*Valera et al.*, 2008]. Differently from numerical models assuming a non linear rheology [*Schott and Schmeling*, 1998; *Morency and Doin*, 2004; *Gogus and Pysklywec*, 2008b], strain localization and DLM breakoff never occur in our experiments due to the constant viscosity of the materials used here, and therefore the amplitude of depression keeps on increasing until the DLM reaches the base of the box. On the other hand, the two-dimensional approach adopted in thermal-mechanical numerical models likely leads to underestimation of velocity of delamination, since return flow around the edges of DLM (toroidal flow) is not accounted for.

4.4. Comparison with natural systems

Despite the oversimplified experimental setting, we can try to export the modeling results to interpret the behavior of natural systems, taking into account the limitations imposed by the adopted experimental setting (see section 2). In the following discussion we focus on a qualitative comparison with the southern Sierra Nevada range (California, USA), as a large number of observations compatible with the occurrence of delamination are found in this area. For instance, *Zandt et al.* [2004] proposed a sequential history for the evolution of the southern Sierra Nevada, based on the lateral propagation of the foundering of an ultramafic lithospheric root. *Le Pourhiet et al.* [2006] considered a completely different initial

setup and proposed a delamination model in which a local instability induced a localized small-scale convection that thermally eroded the lithospheric mantle, enhancing the connection between the asthenosphere and lower crust by means of a low viscosity zone. Whatever the triggering mechanism, our setup reproduces similar scale situation. We performed experiments with a scaled lithospheric root of 42 to 83 km, present over a width of 83 to 250 km, coherent with the supposed delaminated root estimated to 40 to 70 km thick [Ducea and Saleeby, 1998] that probably underlain most of the ca. 100 km-wide Sierra Nevada range [Jones *et al.*, 2004]. The density contrast with the asthenosphere is estimated to 10 kg m^{-3} (from three-dimensional shear-wave velocity structure [Fay *et al.*, 2008a]) to 200 kg m^{-3} (from xenoliths studies [Ducea and Saleeby, 1998]), in the same order of magnitude as our scaled values of 23 to 100 kg m^{-3} . The presence of an adjacent weak area is generally attributed to the previous early Cenozoic subduction and could represent a fluid-weakened lithosphere by dehydration processes [Schott and Schmeling, 1998; Zandt *et al.*, 2004; Valera *et al.*, 2008]. Alternatively, an “asthenospheric conduit” would be more consistent with strong thermal thinning in the upper plate above the hydrated zone [Arcay *et al.*, 2007]. For simplicity, the experiments performed in this study are always characterized by free boundaries while in nature plates are laterally confined. In particular, it would imply that the plate motion recorded during the last stage of our experimental delamination is not realistic since a laterally constrained natural plate would exhibit a strong active shortening retoward of the delamination’s direction, as recorded in models characterized by free-slip boundary conditions [e.g. Schott and Schmeling 1998]. Hence, in nature the topographic signal could also be affected by an extra uplift due to thickening of the crust.

The global topographic pattern obtained in the analog models reproduces well the surface features of the Sierra Nevada region. The depression over the sinking DLM is consistent with the subsidence currently recognized in the Tulare Lake basin (southern Great Valley [Saleeby and Foster, 2004]). Uplift associated with poloidal flow and replacement of lithospheric mantle by more buoyant asthenosphere (Figure II.10) is coherent with the recent uplift/tilting of the Sierra Nevada range [Unruh, 1991; Wakabayashi and Sawyer, 2001; Saleeby and Foster, 2004; Stock *et al.*, 2004; Bennett *et al.*, 2009]. The order of magnitude of both isostatic reequilibration (2 km) and dynamically uplifted bulge (1.7 to 6.7 km) obtained in laboratory (Figure II.5) are similar to the estimated uplift of the Sierra $>1 \text{ km}$ [e.g. Jones *et al.*, 2004 and references therein]. However, in our models, the removal of lithosphere is preceded by strong subsidence accompanying the dynamic uplift. Though today’s Great Valley fits such a pattern [Saleeby and Foster, 2004], there is no record of subsidence in the

Sierra Nevada Range preceding its recent uplift. Deformation pattern with proward propagation of the extension front above the delaminated area (Figure II.4) is consistent with the westward migration of normal faulting along the edge of the Sierra [Jones *et al.*, 2004 and references therein]. Both partial melting found in the lower crust under Sierra Nevada [Ducea and Saleeby, 1998], return-flow [Boyd *et al.*, 2004] and high alkaline magmatic pulse migrating over the last 4-3 Myr [Manley *et al.*, 2000] are observations compatible with our experimental study, which shows the strong upwelling and intrusion of the asthenosphere along the base of the crust (Figure II.10). Mantle flow patterns imply large shear stress at the base of the lower crust. Poloidal flow injecting the lower crust will induce proward-directed shear, whereas the counterflow will produce retroward-directed shear. The seismic anisotropy fabric of the crust-mantle boundary recognized using receiver functions is interpreted to be likely caused by shearing along a detachment zone [Zandt *et al.*, 2004], which is in agreement with our modeling results.

One puzzling point in the history of the Sierra Nevada is the timing of delamination. Although the presence of the eclogitic root is attested since ca. 80 My, delamination started very recently at ca. 8 My and was very rapid [Ducea and Saleeby, 1998; Manley *et al.*, 2000; Wakabayashi and Sawyer, 2001; Jones *et al.*, 2004]. In our experiments, a long initiation phase (because of a low root pull force and/or high viscosity contrast between lithosphere and asthenosphere) is always correlated with a slow process and conversely. We suggest that the onset of delamination could be related to a change in boundary conditions or a disturbing intermediate-depth event (e.g. change in global mantle flow circulation), not reproduced in our models.

7. Conclusions

The present work highlights the dynamics of continental delamination with little internal deformation and triggered by the presence of a density anomaly (lithospheric root) and a weak zone. Our results show that delamination is first controlled by coupling between lower crust and lithospheric mantle and bending resistance of the DLM during a slow initiation phase. The propensity for delamination to initiation can be empirically constrained via a parameter I representative of the ratio of driving forces over resisting forces. Delamination then evolves toward a root-pull dominated phase during which the delaminating lithospheric mantle adopts the dynamics of a Stokes' sinker. Vertical velocity and propensity for the process to stop or proceed during this second stage can be characterized by an

empirical buoyancy parameter B . The induced topographic response is a combination of local isostatic reequilibration, flexural bending and dynamic topography. Especially, the onset of delamination is not marked by uplift, but by a strong dynamic subsidence above the density anomaly, associated with contraction. A poloidal mantle flow then develops around the tip of the DLM and is responsible for a strong dynamic uplift next to the delamination hinge. Ultimately, a counterflow triggers a retoward motion of the model that could induce a significant amount of shortening in constrained natural systems. Many features of our models are consistent with observations in the Sierra Nevada (overall topographic signal, migration of extension and volcanism). However, the absence of significant subsidence preceding uplift of the range and timing/duration of delamination suggest that others processes than pure density-driven detachment may have affected the Sierra Nevada and triggered delamination.

8. Notation

g	gravitational acceleration, m s^{-2}
h_l	thickness of the continental lithosphere, m
h_{UC}	thickness of the upper crust, m
h_{LC}	thickness of the lower crust, m
h_{LM}	thickness of the lithospheric mantle, m
h_{asth}	thickness of the upper mantle asthenosphere, m
W	width of the lithospheric root, m
H	thickness of the lithospheric root, m
w	width of the asthenospheric channel, m
w_c	critical width of the asthenospheric channel, m
ρ_l	density of the continental lithosphere, kg m^3
ρ_{UC}	density of the upper crust, kg m^3
ρ_{LC}	density of the lower crust, kg m^3
ρ_{LM}	density of the lithospheric mantle, kg m^3
ρ_{asth}	density of the asthenosphere, kg m^3
$\Delta\rho$	density contrast between lithospheric mantle and asthenosphere, kg m^3
η_l	viscosity of the continental lithosphere, Pa s^{-1}
η_{LC}	viscosity of the lower crust, Pa s^{-1}

η_{LM}	viscosity of the lithospheric mantle, Pa s ⁻¹
η_{asth}	viscosity of the asthenosphere, Pa s ⁻¹
τ_{LC}	shear stress at the base of the lower crust, N m ⁻²
$\dot{\gamma}$	shear rate in the lower crust, s ⁻¹
v	velocity in the lower crust, m s ⁻¹
V_d	horizontal velocity of delamination (hinge migration), m s ⁻¹
V	mean vertical velocity of the DLM during Stokes' phase, m s ⁻¹
r	radius of curvature of the lithospheric mantle expressed as deviation of the initial straight shape, m
t	duration of initiation phase, s
T	total duration of the experiment, s
T°	ratio of duration of initiation over total duration of the experiment
t°	characteristic time
U°	characteristic velocity
F_{rp}	root pull force, N
R_b	bending resistance of the lithospheric mantle, N m ⁻¹
R_{asth}	viscous resistance at the interface DLM-asthenosphere, N m ⁻¹
I	initiation parameter, s ⁷ m ⁻³
I_c	critical value of the initiation parameter, s ⁷ m ⁻³
B	buoyancy parameter, m ⁴ s ⁴ kg ⁻¹
B_c	critical value of the buoyancy parameter, m ⁴ s ⁴ kg ⁻¹

Acknowledgments

F. Bajolet was funded by the European Union FP7 Marie Curie ITN “Crystal2Plate”, contract no. 215353. J. Galeano and A. M. Negredo acknowledge support from Spanish Research Ministry projects CGL2008-04968, CGL2009-13103 and CSD2006-00041 (TOPO-IBERIA). F. Funiciello was supported by the European Young Investigators (EURYI) Awards Scheme (Eurohorcs/ESF including funds the National Research Council of Italy). Experiments presented in this paper have been realized at the Laboratory of Experimental Tectonics, Univ. "Roma TRE", Italy. The paper benefited from constructive reviews by T. Gerya and the editor J. Tyburczy.

References

- Arcay, D., E. Tric, and M. P. Doin (2007), Slab surface temperature in subduction zones: Influence of the interplate decoupling depth and upper plate thinning processes, *Earth Planet. Sci. Lett.*, 255(3-4), 324-338, doi:10.1016/j.epsl.2006.12.027.
- Arnold, J., W. R. Jacoby, H. Schmeling, and B. Schott (2001), Continental collision and the dynamic and thermal evolution of the Variscan orogenic crustal root - numerical models, *J. Geodyn.*, 31(3), 273-291, doi:10.1016/S0264-3707(00)00023-5.
- Bennett, R. A., N. P. Fay, S. Hreinsdottir, C. Chase, and G. Zandt (2009), Increasing long-wavelength relief across the southeastern flank of the Sierra Nevada, California, *Earth Planet. Sci. Lett.*, 287(1-2), 255-264, doi:10.1016/j.epsl.2009.08.011.
- Bird, P. (1978), Initiation of Intracontinental Subduction in the Himalaya, *J. Geophys. Res.*, 83(B10), 4975-4987, doi:10.1029/JB083iB10p04975.
- Bird, P. (1979), Continental Delamination and the Colorado Plateau, *J. Geophys. Res.*, 84(B13), 7561-7571.
- Bird, P., and J. Baumgardner (1981), Steady Propagation of Delamination Events, *J. Geophys. Res.*, 86(B6), 4891-4903, doi:10.1029/JB086iB06p04891.
- Boyd, O. S., C. H. Jones, and A. F. Sheehan (2004), Foundering lithosphere imaged beneath the Southern Sierra Nevada, California, USA, *Science*, 305, 660-662, doi:10.1126/science.1099181.
- Calvert, A., E. Sandvol, D. Seber, M. Barazangi, S. Roecker, T. Mourabit, F. Vidal, G. Alguacil, and N. Jabour (2000), Geodynamic evolution of the lithosphere and upper mantle beneath the Alboran region of the western Mediterranean: Constraints from travel time tomography, *J. Geophys. Res.*, 105(B5), 10871-10898, doi:10.1029/2000JB900024.
- Cardozo, N., and R. W. Allmendinger (2009), SSPX: A program to compute strain from

displacement/velocity data, *Comput. Geosci.*, 35(6), 1343-1357, doi:10.1016/j.cageo.2008.05.008.

Channell, J. E. T., and J. C. Mareschal (1989), Delamination and asymmetric lithospheric thickening in the development of the Tyrrhenian Rif, in *Alpine Tectonics*, edited by M. P. Coward, D. Dietrich and R. G. Park, *Geol. Soc. Spec. Publ.*, 45, 285-302, doi:10.1144/GSL.SP.1989.045.01.16.

Chemenda, A. I., J. P. Burg, and M. Mattauer (2000), Evolutionary model of the Himalaya-Tibet system: geopoem based on new modelling, geological and geophysical data, *Earth Planet. Sci. Lett.*, 174(3-4), 397-409, doi:10.1016/s0012-821x(99)00277-0.

Conrad, C. P., and B. H. Hager (1999), Effects of plate bending and fault strength at subduction zones on plate dynamics, *J. Geophys. Res.*, 104(B8), 17551-17571, doi:10.1029/1999JB900149.

Davies, G. F. (1980), Mechanics of subducted lithosphere, *J. Geophys. Res.*, 85(B11), 6304–6318, doi:10.1029/JB085iB11p06304.

Davy, P., and P. R. Cobbold (1991), Experiments on Shortening of a 4-Layer Model of the Continental Lithosphere, *Tectonophysics*, 188(1-2), 1-25, doi:10.1016/0040-1951(91)90311-F.

Ducea, M., and J. Saleeby (1998), A case for delamination of the deep batholithic crust beneath the Sierra Nevada, California, *Int. Geol. Rev.*, 40(1), 78-93, doi:10.1080/00206819809465199.

England, P., and G. Houseman (1989), Extension during Continental Convergence, with Application to the Tibetan Plateau, *J. Geophys. Res.*, 94(B12), 17561-17579, doi:10.1029/JB094iB12p17561.

Faccenda, M., G. Minelli, and T. V. Gerya (2009), Coupled and decoupled regimes of continental collision: Numerical modeling, *Earth Planet. Sci. Lett.*, 278(3-4), 337-349, doi:10.1016/j.epsl.2008.12.021.

- Faccenna, C., P. Davy, J. P. Brun, R. Funiciello, D. Giardini, M. Mattei, and T. Nalpas (1996), The dynamics of back-arc extension: An experimental approach to the opening of the Tyrrhenian Sea, *Geophys. J. Int.*, *126*(3), 781-795, doi:10.1111/j.1365-246X.1996.tb04702.x.
- Faccenna, C., D. Giardini, P. Davy, and A. Argentieri (1999), Initiation of subduction at Atlantic-type margins: Insights from laboratory experiments, *J. Geophys. Res.*, *104*(B2), 2749-2766, doi:10.1029/1998JB900072.
- Fay, N. P., R. A. Bennett, J. C. Spinler, and E. D. Humphreys (2008a), Small-scale upper mantle convection and crustal dynamics in southern California, *Geochem. Geophys. Geosyst.*, *9*(8), Q08006, doi:10.1029/2008gc001988.
- Fillerup, M. A., J. H. Knapp, C. C. Knapp, and V. Raileanu (2010), Mantle earthquakes in the absence of subduction? Continental delamination in the Romanian Carpathians, *Lithosphere*, *2*(5), 333-340, doi:10.1130/L102.1.
- Forsyth, D., and S. Uyeda (1975), On the relative importance of the driving forces of plate tectonics, *Geophys. J. R. Astr. Soc.*, *43*(1), 163-200, doi:10.1111/j.1365-246X.1975.tb00631.x.
- Funiciello, F., C. Faccenna, D. Giardini, and K. Regenauer-Lieb (2003), Dynamic of retreating slabs: 2. Insights from three-dimensional laboratory experiments, *J. Geophys. Res.*, *108*(B4), 2207, doi:10.1029/2001JB000896.
- Funiciello, F., C. Faccenna, and D. Giardini (2004), Role of lateral mantle flow in the evolution of subduction systems: insights from laboratory experiments, *Geophys. J. Int.*, *157*(3), 1393-1406, doi:10.1111/j.1365-246X.2004.02313.x.
- Funiciello, F., M. Moroni, C. Piromallo, C. Faccenna, A. Cenedese, and H. A. Bui (2006), Mapping mantle flow during retreating subduction: Laboratory models analyzed by feature tracking, *J. Geophys. Res.*, *111*(B3), B03402, doi:10.1029/2005JB003792.

- Funiciello, F., C. Faccenna, A. Heuret, S. Lallemand, E. Di Giuseppe, and T. W. Becker (2008), Trench migration, net rotation and slab-mantle coupling, *Earth Planet. Sci. Lett.*, 271(1-4), 233-240, doi:10.1016/j.epsl.2008.04.006.
- Girbacea, R., and W. Frisch (1998), Slab in the wrong place: Lower lithospheric mantle delamination in the last stage of the eastern Carpathian subduction retreat, *Geology*, 26(7), 611-614, doi:10.1130/0091-7613(1998)026<0611:SITWPL>2.3.CO;2.
- Gogus, O. H., and R. N. Pysklywec (2008a), Mantle lithosphere delamination driving plateau uplift and synconvergent extension in eastern Anatolia, *Geology*, 36(9), 723-726, doi:10.1130/G24982A.1.
- Gogus, O. H., and R. N. Pysklywec (2008b), Near-surface diagnostics of dripping or delaminating lithosphere, *J. Geophys. Res.*, 113(B11), B11404, doi:10.1029/2007JB005123.
- Gogus, O. H., R. N. Pysklywec, F. Corbi, and C. Faccenna (2011), The surface tectonics of mantle lithosphere delamination following ocean lithosphere subduction: Insights from physical-scaled analogue experiments, *Geochem. Geophys. Geosyst.*, 12(5), Q05004, doi:10.1029/2010gc003430.
- Griffiths, R. W. (1995), A laboratory investigation of effects of trench migration on the descent of subducted slabs, *Earth Planet. Sci. Lett.*, 133(1-2), 1-17, doi:10.1016/0012-821X(95)00027-A.
- Guillou-Frottier, L., J. Buttles, and P. Olson (1995), Laboratory experiments on the structure of subducted lithosphere, *Earth Planet. Sci. Lett.*, 133(1-2), 19-34, doi:10.1016/0012-821X(95)00045-E.
- Houseman, G., D. McKenzie, and P. Molnar (1981), Convective instability of a thickened boundary layer and its relevance for the thermal evolution of continental convergent belts, *J. Geophys. Res.*, 86(B7), 6115-6132, doi:10.1029/JB086iB07p06115.
- Jacoby, W. R. (1980), Plate Sliding and Sinking in Mantle Convection and the Driving

Mechanism, in *Mechanisms of Continental Drift and Plate Tectonics*, edited by P. A. Davis and F. R. S. Runcorn, pp. 159-172, *Academic Press*.

Jones, C. H., G. L. Farmer, and J. Unruh (2004), Tectonics of Pliocene removal of lithosphere of the Sierra Nevada, California, *Geol. Soc. Am. Bull.*, 116(11-12), 1408-1422, doi:10.1130/b25397.1.

Kincaid, C., and P. Olson (1987), An Experimental-Study of Subduction and Slab Migration, *J. Geophys. Res.*, 92(B13), 13832-13840, doi:10.1029/JB092iB13p13832.

Knapp, J. H., C. C. Knapp, V. Raileanu, L. Matenco, V. Mocanu, and C. Dinu (2005), Crustal constraints on the origin of mantle seismicity in the Vrancea zone, Romania: The case for active continental lithospheric delamination, *Tectonophysics*, 410(1-4), 311-323, doi:10.1016/j.tecto.2005.02.020.

Lallemand, S., A. Heuret, C. Faccenna, and F. Funiciello (2008), Subduction dynamics as revealed by trench migration, *Tectonics*, 27(3), TC3014, doi:10.1029/2007tc002212.

Lastowka, L. A., A. F. Sheehan, and J. M. Schneider (2001), Seismic evidence for partial lithospheric delamination model of Colorado Plateau uplift, *Geophys. Res. Lett.*, 28(7), 1319-1322, doi:10.1029/2000GL012360.

Le Pourhiet, L., M. Gurnis, and J. Saleeby (2006), Mantle instability beneath the Sierra Nevada mountains in California and Death Valley extension, *Earth Planet. Sci. Lett.*, 251(1-2), 104-119, doi:10.1016/j.epsl.2006.08.028.

Levander, A., B. Schmandt, M. S. Miller, K. Liu, K. E. Karlstrom, R. S. Crow, C. T. A. Lee, and E. D. Humphreys (2011), Continuing Colorado plateau uplift by delamination-style convective lithospheric downwelling, *Nature*, 472, 461-465, doi:10.1038/nature10001.

Manley, C. R., A. F. Glazner, and G. L. Farmer (2000), Timing of volcanism in the Sierra Nevada of California: Evidence for Pliocene delamination of the batholithic root?, *Geology*, 28(9), 811-814, doi:10.1130/0091-7613(2000)28<811:tohits>2.0.co;2.

- McKenzie, D. (1977), The initiation of trenches: A finite amplitude instability, in *Island Arcs, Deep Sea Trenches and Back-Arc Basins*, edited by M. Talwani and W. C. Pitman, pp. 57-62, AGU, Washington D. C.
- Morency, C., and M. P. Doin (2004), Numerical simulations of the mantle lithosphere delamination, *J. Geophys. Res.*, *109*(B3), B03410, doi:10.1029/2003JB002414.
- Pysklywec, R. N., and A. R. Cruden (2004), Coupled crust-mantle dynamics and intraplate tectonics: Two-dimensional numerical and three-dimensional analogue modeling, *Geochem. Geophys. Geosyst.*, *5*(10), Q10003, doi:10.1029/2004GC000748.
- Saleeby, J., and Z. Foster (2004), Topographic response to mantle lithosphere removal in the southern Sierra Nevada region, California, *Geology*, *32*(3), 245-248, doi:10.1130/g19958.1.
- Schellart, W. P. (2004), Kinematics of subduction and subduction-induced flow in the upper mantle, *J. Geophys. Res.*, *109*(B7), B07401, doi:10.1029/2004jb002970.
- Schott, B., and H. Schmeling (1998), Delamination and detachment of a lithospheric root, *Tectonophysics*, *296*(3-4), 225-247, doi:10.1016/S0040-1951(98)00154-1.
- Seber, D., M. Barazangi, A. Ibenbrahim, and A. Demnati (1996), Geophysical evidence for lithospheric delamination beneath the Alboran Sea and Rif-Betic mountains, *Nature*, *379*, 785-790, doi:10.1038/379785a0.
- Stock, G. M., R. S. Anderson, and R. C. Finkel (2004), Pace of landscape evolution in the Sierra Nevada, California, revealed by cosmogenic dating of cave sediments, *Geology*, *32*(3), 193-196, doi:10.1130/g20197.1.
- Turcotte, D. L., and G. Schubert (1982), *Geodynamics Application of Continuum Physics to Geological Problems*, 450 pp., John Wiley, New York.
- Unruh, J. R. (1991), The Uplift of the Sierra-Nevada and Implications for Late Cenozoic Epeirogeny in the Western Cordillera, *Geol. Soc. Am. Bull.*, *103*(11), 1395-1404,

doi:10.1130/0016-7606(1991)103<1395:tuotsn>2.3.co;2.

Valera, J. L., A. M. Negredo, and A. Villasenor (2008), Asymmetric Delamination and Convective Removal Numerical Modeling: Comparison with Evolutionary Models for the Alboran Sea Region, *Pure Appl. Geophys.*, *165*(8), 1683-1706, doi:10.1007/s00024-008-0395-8.

Valera, J. L., A. M. Negredo, and I. Jimenez-Munt (2011), Deep and near-surface consequences of root removal by asymmetric continental delamination, *Tectonophysics*, *502*(1-2), 257-265, doi:10.1016/j.tecto.2010.04.002.

Wakabayashi, J., and T. L. Sawyer (2001), Stream incision, tectonics, uplift, and evolution of topography of the Sierra Nevada, California, *J. Geol.*, *109*(5), 539-562, doi:10.1086/321962.

Weijermars, R., and H. Schmeling (1986), Scaling of Newtonian and non-Newtonian fluid dynamics without inertia for quantitative modeling of rock flow due to gravity (including the concept of rheological similarity), *Phys. Earth Planet. In.*, *43*, 316-330, doi:10.1016/0031-9201(86)90021-X.

Zandt, G., H. Gilbert, T. J. Owens, M. Ducea, J. Saleeby, and C. H. Jones (2004), Active foundering of a continental arc root beneath the southern Sierra Nevada in California, *Nature*, *431*, 41-46, doi:10.1038/nature02847.

Part III: Dynamic topography in subduction zones

1. Introduction, model setup and force balance

1.1. Introduction

The topography in subduction zones can exhibit very complex patterns due to the variety of forces operating in such context. If we can deduce the theoretical isostatic value from density structure of the lithosphere, the effect of flexural bending, and even more the dynamic component of topography are difficult to quantify. With the following experiments, we attempt to measure and interpret the topography of the overriding plate in a subduction process compared to pure shortening setting. This approach aims at distinguishing and quantifying the isostatic, flexural and dynamic component of a subduction zone.

1.2. Model setup

The performed experiments are composed of thin sheets of silicone putty and are of two types: with a dense oceanic subducting plate (Figure III.1a), or with a light continental plate (Figure III.1b). In both cases, the upper plate is composed of a continental lithosphere and a weak zone that localizes the deformation in the center of the model. The plates are lying on a Newtonian low-viscosity syrup simulating the asthenosphere. The properties of analog materials are listed in Table III.1.

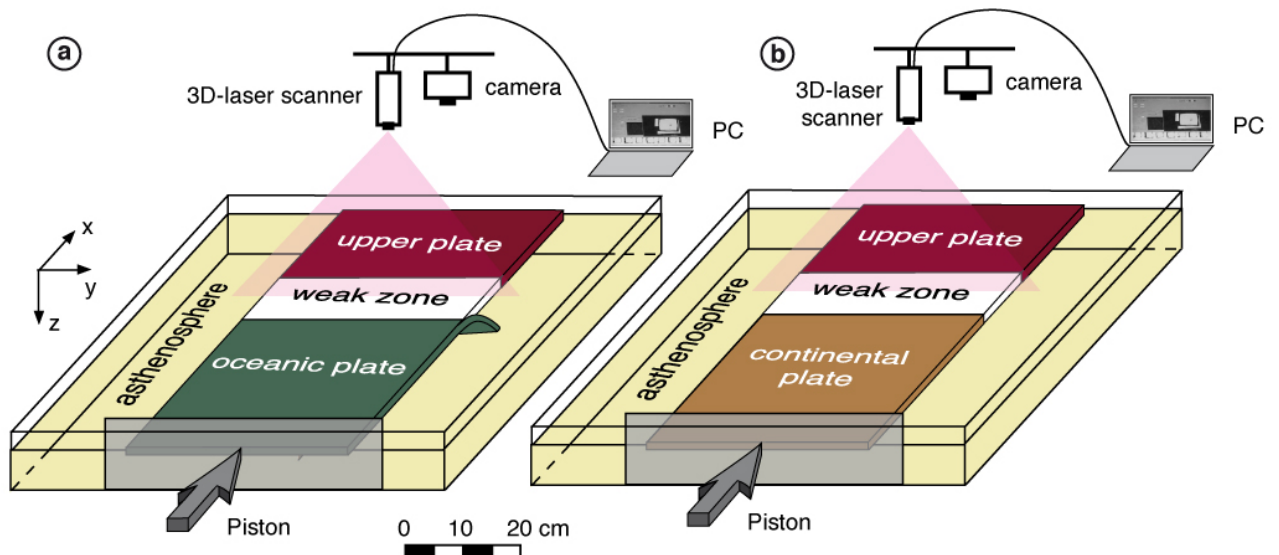


Figure III.1. Experimental setup for (a) subduction experiment, (b) shortening experiment.

Material	Density (kg m ⁻³)	Viscosity (Pa s)
Black ocean	1495	3.4 x 10 ⁴
Lower continent	1390	4.7 x 10 ⁴
Black upper continent	1364	3.2 x 10 ⁴
Weak zone	967	1 x 10 ⁴
Intermediate syrup (asthenosphere)	1428	22

Table III.1. Materials properties. Viscosities are given for room temperature (22°C) and an experimental strain rate of 10⁻² s⁻¹ (scaled for nature).

The overriding plate is attached to the back-wall of the tank, and the lower plate is attached to a piston with a constant convergence rate of 2 cm min⁻¹ equivalent to 6.2 cm yr⁻¹ in nature. The bottom of the tank represents the 660 km discontinuity and the box is large enough to minimize boundary effects and allows for toroidal flow in the subduction setup [Funiciello *et al.*, 2006]. The experimental setting is properly scaled to be comparable with nature [e.g. Weijermars and Schmeling, 1986; Davy and Cobbold, 1991; Table III.2]. The density contrast and viscosity ratio between oceanic slab and asthenosphere in the subduction experiment are - 67 kg m⁻³ and 1.5 × 10³ respectively. The scale factor for length is 1.7 × 10⁻⁷ so that 1 cm in the models represents 66 km in nature. The adopted setup implies the following assumptions, and consequent limitations, that are detailed in Funiciello *et al.* [2003]: (1) isothermal system, (2) constant viscosity and density over the depth of the individual layers, (3) lack of global background mantle flow, (4) 660 km discontinuity as an impermeable barrier.

In the subduction experiment, we manually initiate the subduction by pushing the free edge of the oceanic plate into the glucose syrup. In the shortening experiments, the three silicone plates are attached to each other. The experiments are monitored by top and side view photographs, and the topography is regularly recorded with a 3D laser-scanner (RealScan USB) whose precision is 0.2 mm.

	Parameter	Nature	Model
g	Gravitational acceleration (m s ⁻²)	9.81	9.81
Thickness ^a			
h_l	Lithosphere (m)	70000	0.012
h_{asth}	Upper mantle asthenosphere (m)	660000	0.11
Density			
ρ_c	Continental lithosphere (kg m ³)	3200	1390-1364
ρ_o	Oceanic lithosphere (kg m ³)	3320	1495
ρ_{asth}	Upper mantle asthenosphere (kg m ³)	3220	1428

ρ_c / ρ_{asth}	Density ratio continent	0.99	0.99
ρ_o / ρ_{asth}	Density ratio ocean	1.04	1.05
$\rho_c - \rho_{asth}$	Density contrast continent	20	38-64
$\rho_o - \rho_{asth}$	Density contrast ocean	-100	-67
Viscosity			
η_c	Continental lithosphere (Pa s ⁻¹)	10 ²³	3.2-4.7 × 10 ⁴
η_o	Oceanic lithosphere (Pa s ⁻¹)	10 ²⁴	3.4 × 10 ⁴
η_{asth}	Upper mantle asthenosphere (Pa s ⁻¹)	10 ²¹	22
η_c / η_{asth}	Viscosity ratio continent	10 ²	1.5-2.1 × 10 ³
η_o / η_{asth}	Viscosity ratio ocean	10 ³	1.5 × 10 ³
Dimensionless parameters		Equivalence model-nature	
t°	Characteristic time: ($t_{\text{model}}/t_{\text{nature}} = (\Delta\rho gh)_{\text{lith nature}} / (\Delta\rho gh)_{\text{lith model}} \times (\eta_{\text{l model}} / \eta_{\text{l nature}})$)	1.01 × 10 ⁻¹²	1 min _{model} → 1.89 My _{nature}
U°	Characteristic velocity: ($U_{\text{model}}/U_{\text{nature}} = t_{\text{nature}} / t_{\text{model}} \times L_{\text{model}} / L_{\text{nature}}$)	5.5 × 10 ⁵	1 cm min ⁻¹ _{model} → 3.1 cm y ⁻¹ _{nature}

Table III.2. Scaling of experimental parameters. In both subduction and shortening experiments, the lithospheres have the same thicknesses (1.2 cm).

1.3. Force balance

The evolution of the models is controlled by the balance between driving and resisting forces. The possible driving forces are the tectonic force (F_t) and the slab pull (F_{sp}). The tectonic force is the force applied at plate boundaries and is simulated in the models by the constant push of the rigid piston. The slab pull force is active only in the subduction experiment and is proportional to the density contrast between asthenosphere and oceanic slab ($\Delta\rho$), gravity (g) and slab length (L) and thickness (h_l)

$$F_{sp} = \Delta\rho g h_l L \quad (1)$$

The slab pull increases until the slab reaches the bottom of the box, and remains constant during the subsequent evolution of the subduction.

The possible resisting forces are the buoyancy of the upper plate, the bending resistance, the resistance acting at plate interface and the resistance to sliding into the mantle. For the shortening experiment, only the buoyancy of the plates is acting on the system. Because of convergence, the plates thicken and store potential energy. Following *Artyushkov* [1973], *Turcotte* [1982] and *Stein et al.* [1989], the force per unit length due to potential energy scales with the gravity, the density contrast of the plate with respect to the mantle and its thickness.

This stress can be either supported or not by the strength of the plate itself, which in our case is proportional to its viscosity and strain rate.

When subduction occurs, the lower plate has to bend to sink into the asthenosphere. Following *Turcotte and Schubert* [1982], the force necessary to bend a viscous layer can be approximated by

$$R_b \approx V h_l^3 \eta_o / r^3 \quad (2)$$

where V is the velocity of subduction, η_o and r the viscosity and radius of curvature of the oceanic slab (expressed as deviation of the initial straight shape) respectively. The bending resistance is large during the first stages of subduction, but decreases rapidly with r as steady-state is reached.

The resistance of the plates interface is proportional to the plate thickness and the viscosity of the plate interface, considered of the same order as the asthenospheric mantle.

Finally, the resistance to sliding into the mantle is represented by the viscous dissipation exerted at the slab-mantle interface during subduction and is directly proportional to the slab surface and asthenosphere viscosity.

2. Experimental results

In the shortening model, we simply observe homogeneous shortening and thickening of the plates. The most deformed is, as expected, the central weak zone, which concentrates most of the deformation with up to 58% of shortening after 15 min of experiment (Figure III.2a to c and III.3b). The model is also flowing laterally: the width of the weak zone is almost doubled after 15 min.

In the subduction model, the convergence is partly accommodated by the sinking of the oceanic slab into the asthenosphere. Thus, for the same time-step, the amount of shortening is lower than for the shortening model (Figure III.2d to f and III.3b). During the first 4 min of subduction, the slab is progressively sinking into the mantle, the trench slightly advances or is stationary (Figure III.3a), and the weak zone is slightly extending (negative value of shortening, Figure III.3b). At 4 min, the slab reaches the bottom of the box starting the steady-state stage of subduction. The trench then continuously advances (Figure III.3a) and the weak zone shortens (Figure III.3b). Both trench motion and shortening evolve almost linearly with time.

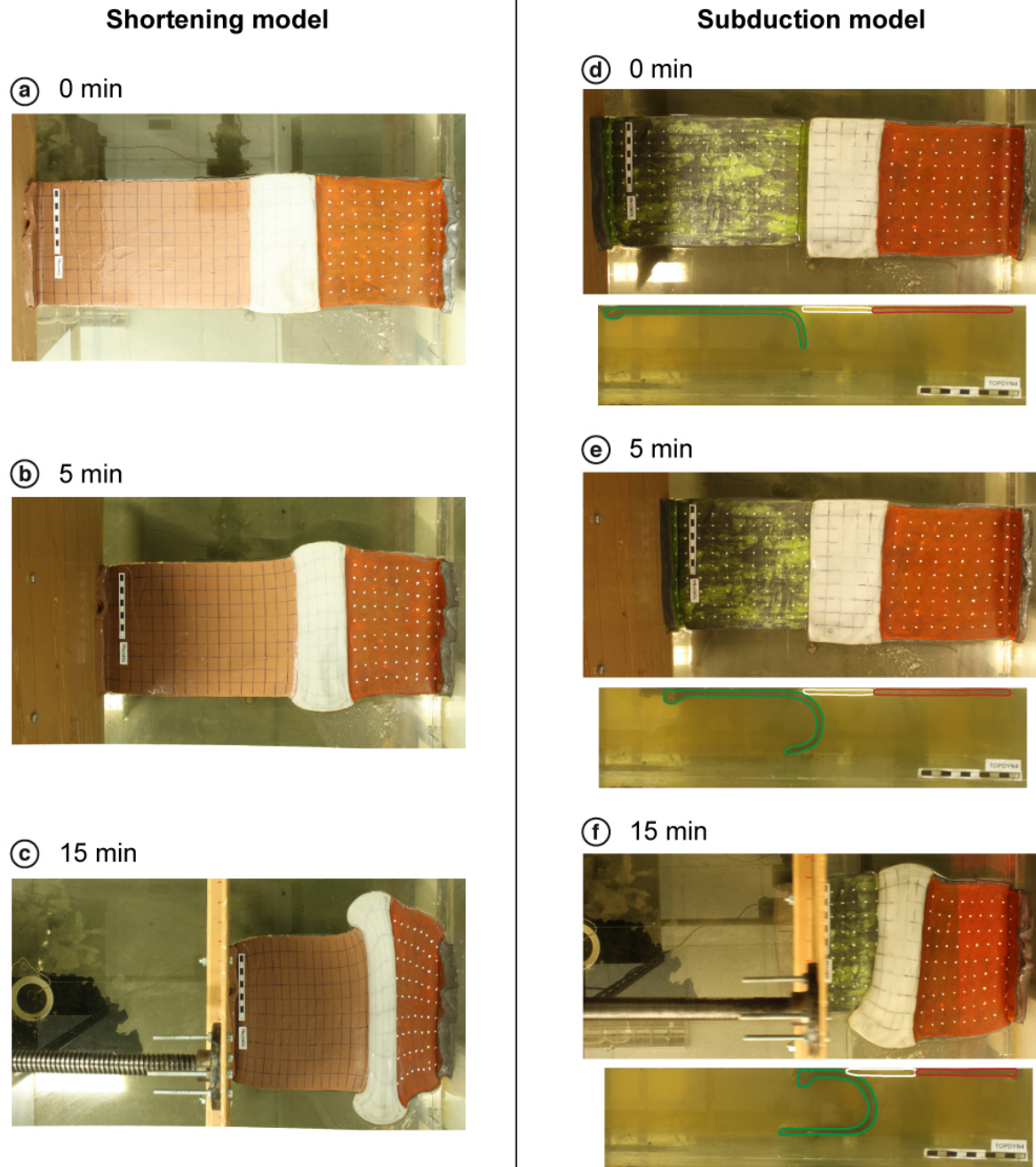


Figure III.2. Top and side view photos of shortening (a, b and c) and subduction model (d, e and f) at three different stages. The piston is on the left side of the pictures and moves toward the right. The weak zone is the white silicone, the upper continent is red, the oceanic plate green and the “lower” continent is brown.

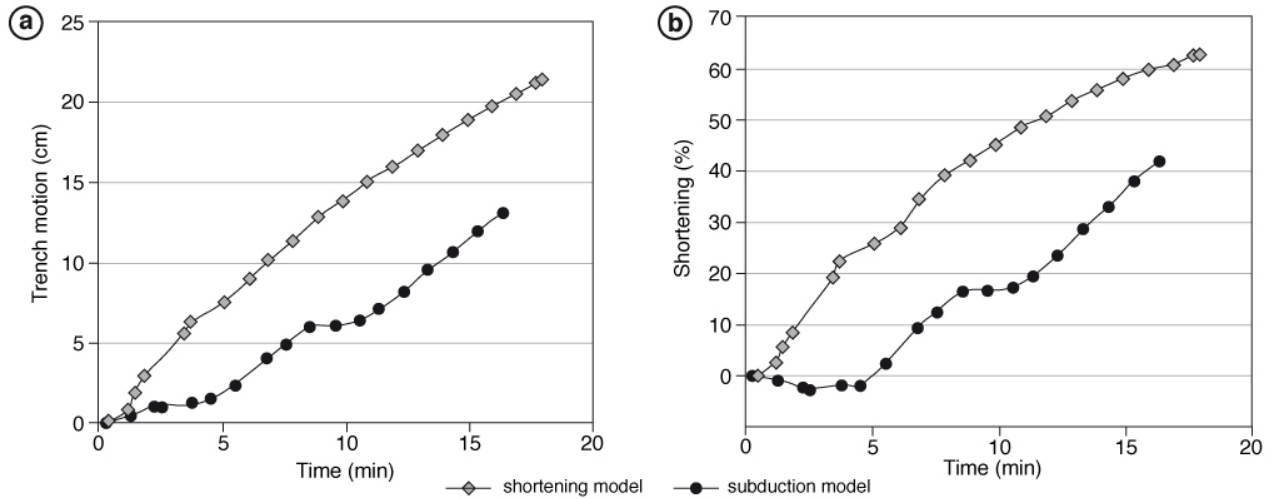


Figure III.3. (a) Evolution of trench motion with time. In the shortening model, it corresponds to the boundary between the “lower” brown continent and the weak zone. (b) Percentage of shortening of the weak zone through time.

The initial topography for the shortening model is characterized by a higher elevation of the light weak zone, corresponding to the expected isostatic value (Figure III.4af). As shortening proceeds, the elevation of the central area increases while the two other plates remain roughly at the same elevation (Figure III.4b to f). Two little depressions form on both sides of the weak zone, at the boundary between the silicones. The elevation inside the weak zone does not evolve homogeneously. The center is less elevated and two little highs rise on the both sides. After 11 min of experiment, the weak zone has gained about 1.5 mm in global elevation (Figure III.4). The difference between the center and the side bulges increases up to 0.6 mm until 9 min and then decreases when the shortening becomes extreme ($> 45\%$).

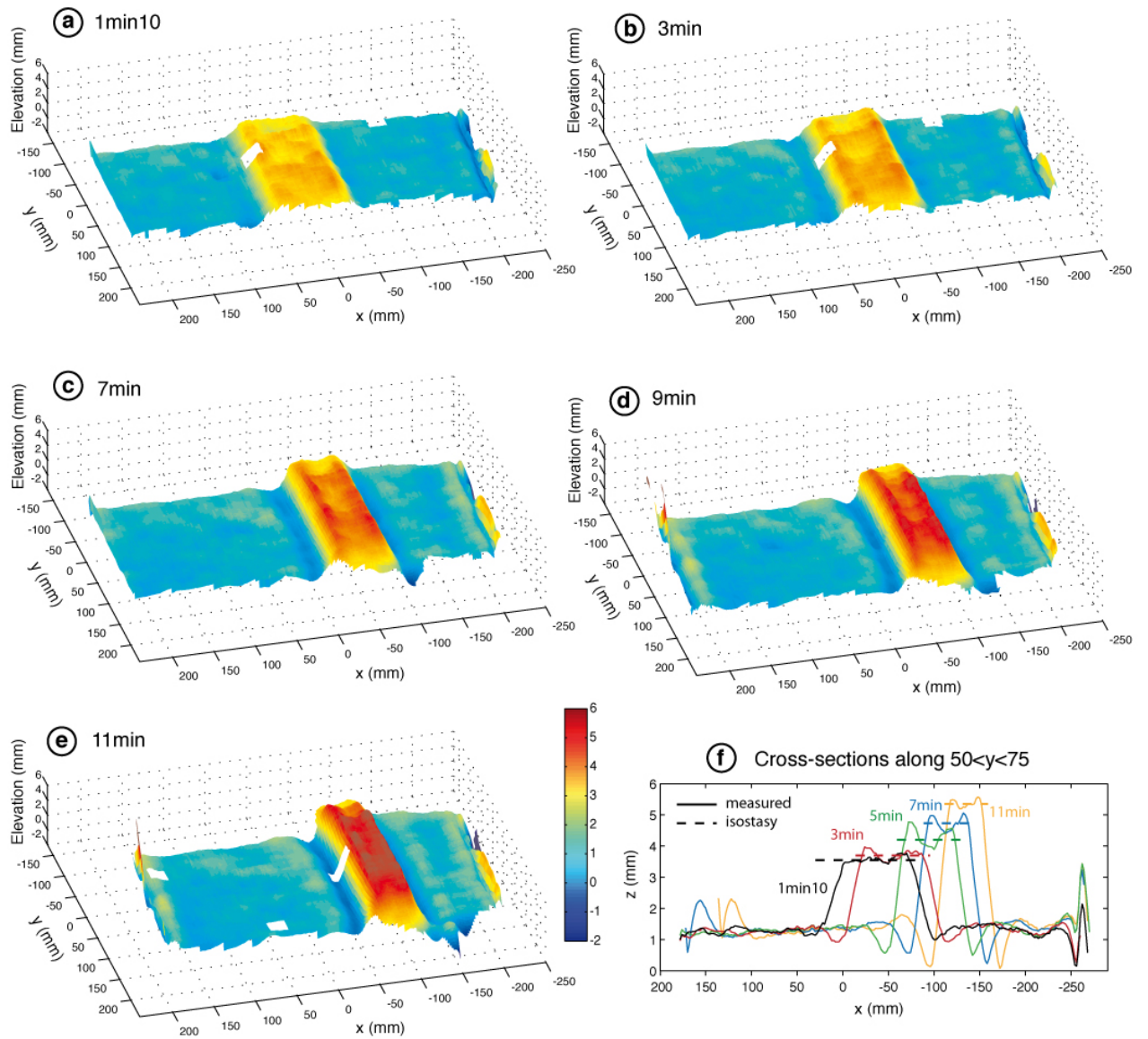


Figure III.4. (a to e) Measured topography at different stage for pure shortening experiment. (f) Corresponding cross-sections along y-axis.

In the subduction model, the initial topography is characterized, from the piston to the back-wall, by a low elevation of the dense oceanic plate, a flexural bulge 0.6 mm high, the trench forming a deep depression (-2.5 mm), the highly elevated weak zone, a little through at the boundary between the silicone putties and the continental upper plate of intermediate elevation (Figure III.5a). As subduction proceeds, the elevation of the weak area globally increases. As for the shortening model, the elevation is not homogeneous: we also observe a depression in the center and two bulges on both sides. But unlike in a pure shortening setting,

the bulges are not symmetric, and the one next to the trench is significantly more elevated. As shortening proceeds, and as for shortening models, the difference in elevation between the side bulges and the center increases up to 1.6 mm at 12 min, then decreases until the central depression disappear (Figure III.5f).

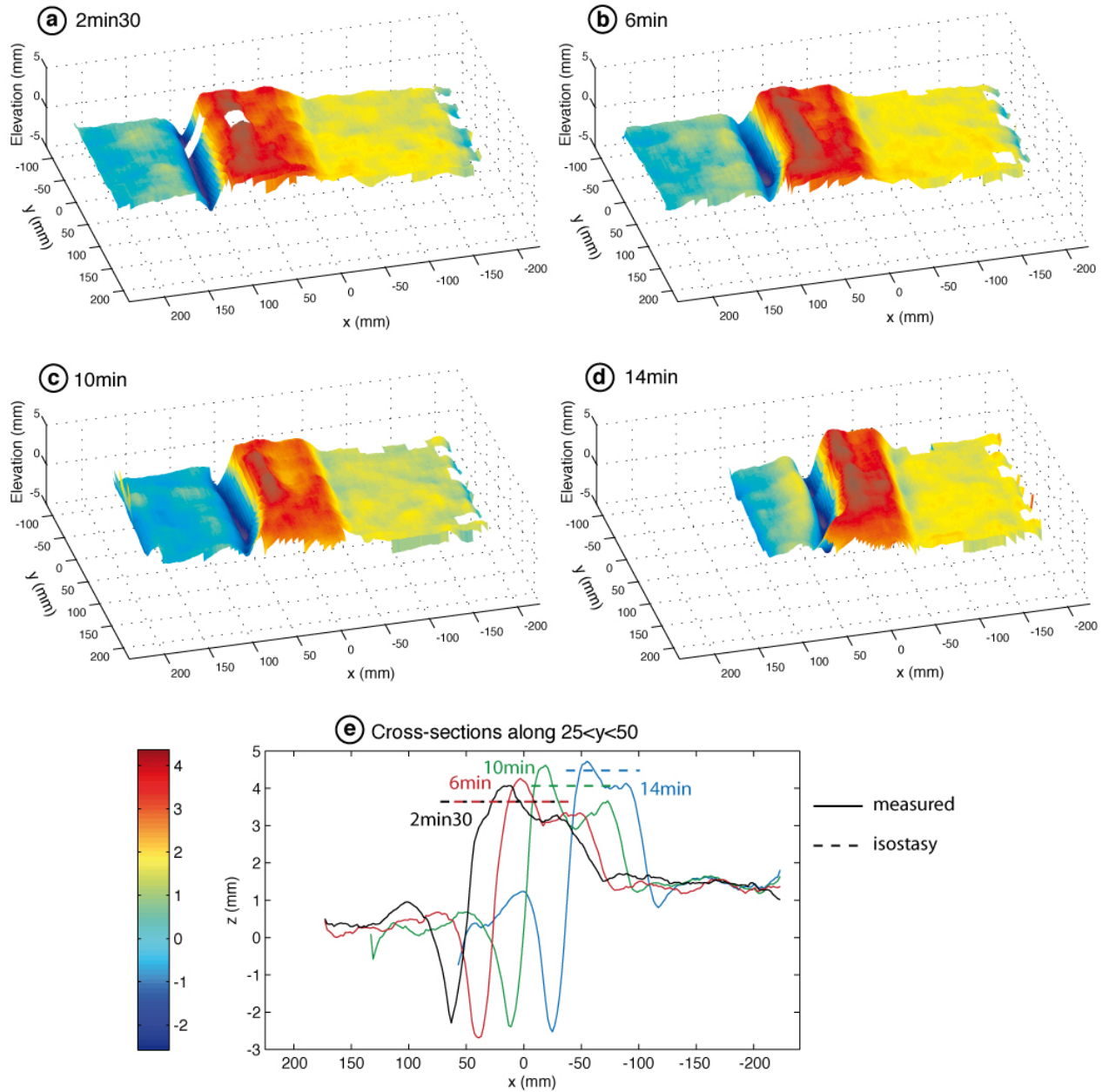


Figure III.5. (a to d) Measured topography at different stage for subduction experiment. (e) Corresponding cross-sections along y-axis.

3. Discussion and conclusions

The global elevation pattern observed in both models is coherent with what is expected. In particular for subduction, the morphology of the flexural bulge and the trench is similar to previous analog experiments [e.g. *Espurt et al.*, 2008; *Luth et al.*, 2010; *Husson et al.*, 2012]. However, a few specific features have to be explained. The two depressions on both sides of the weak zone in the shortening models are most probably due to the boundary between the silicones that creates a discontinuity. The basin shape at the center of the weak zone can be explained by non-homogeneous thickening and lateral escape. Indeed, there might exist a little boundary effect on the sides in contact with the other silicone putties. We can also observe that there is more lateral escape in the central part of the weak zone compared to the sides that are more coupled to the two other plates (Figure III.2bc). These two combined effects cause higher thickening and thus elevation on the sides than in the center. Importantly, although the along-strike elevation of the weak zone is variable, it is globally consistent with the expected isostatic values (Figure III.4f)

In the subduction setup, the bulge next to the trench is higher than the other (Figure III.5f). As the slab has already reached the bottom of the tank at 4 min, this cannot be explained by poloidal flow. A stronger shortening at the subduction front is probably the cause of the asymmetry. It is also possible that the trench advance motion induces an overpressure of fluid in the asthenospheric wedge increasing the elevation next to the trench. Interestingly, this feature is also observed by *Espurt et al.* [2008] during flat slab subduction. The global observed elevations are consistent with isostatic values in the very first stages, but are lower in the late evolution (Figure III.5f).

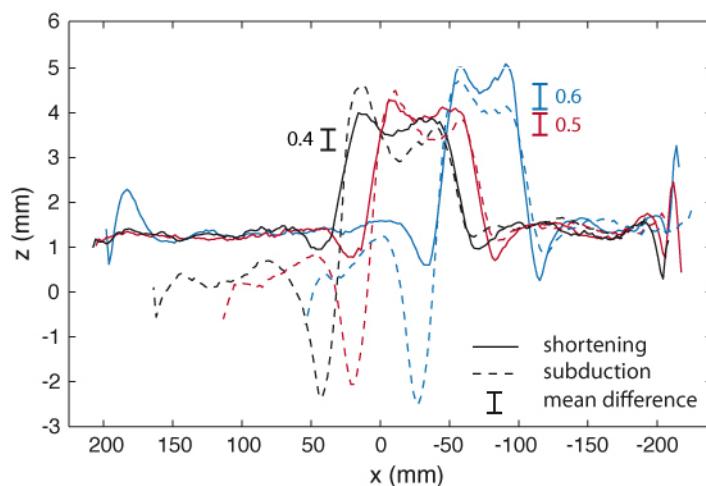


Figure III.6. Along-strike mean topographic profile comparing shortening and subduction experiments at 20% of shortening of the weak zone (black), 29% (red) and 39% (blue).

The influence of subduction and slab pull can be better observed when comparing the elevation in shortening and subduction models for the same amount of shortening of the weak zone, and thus the same theoretical isostatic elevation (Figure III.6). In early stages (for 20% of shortening), the mean elevation is 0.4 mm lower for the subduction model than for the

shortening model, although the bulge next to the trench is higher. In intermediate stages (29% of shortening), we observe 0.5 mm of difference, and in advanced stages (39% of shortening) 0.6 mm. These values correspond to 2.6 to 4 km in nature, and could represent the dynamic effect of the slab lowering sinking into the asthenosphere and lowering the elevation of the upper plate.

In summary, these experiments provide insights into the evolution of topography during subduction and a good basis for further experiments. Common features such as flexural bulge and trench are easily observed. The upper plate elevation is very sensitive to local differences in shortening and records the dynamic effect of the slab pull force.

References

- Artyushkov, E. V. (1973), Stresses in the lithosphere caused by crustal thickness inhomogeneities, *J. Geophys. Res.*, 78(32), 7675–7708, doi:10.1029/JB078i032p07675.
- Davy, P., and P. R. Cobbold (1991), Experiments on Shortening of a 4-Layer Model of the Continental Lithosphere, *Tectonophysics*, 188(1-2), 1-25, doi:10.1016/0040-1951(91)90311-F.
- Funiciello, F., C. Faccenna, D. Giardini, and K. Regenauer-Lieb (2003), Dynamics of retreating slabs: 2. Insights from three-dimensional laboratory experiments, *J. Geophys. Res.*, 108(B4), 2207, doi:10.1029/2001jb000896.
- Funiciello, F., M. Moroni, C. Piromallo, C. Faccenna, A. Cenedese, and H. A. Bui (2006), Mapping mantle flow during retreating subduction: Laboratory models analyzed by feature tracking, *J. Geophys. Res.*, 111(B3), B03402, doi:10.1029/2005JB003792.
- Stein, S., S. Cloetingh, N. H. Sleep, and R. Wortel, Passive margin earthquake, stress and rheology, in *Earthquakes at the North Atlantic Passive Margin: Neotectonics and Postglacial Rebound*, edited by S. Gregersen and P. W. Basham, pp. 231-259, Kluwer Acad., Norwell, MA, 1989.

Turcotte, D. L., The state of stress at passive continental margin, in *Dynamics of Passive Margins, Geodyn. Ser.*, vol. 6, edited by R. A. Scrutton, pp. 141-146, AGU, Washington D. C., 1982.

Turcotte, D. L., and G. Schubert (1982), *Geodynamics Application of Continuum Physics to Geological Problems*, 450 pp., John Wiley, New York.

Weijermars, R., and H. Schmeling (1986), Scaling of Newtonian and non-Newtonian fluid dynamics without inertia for quantitative modeling of rock flow due to gravity (including the concept of rheological similarity), *Phys. Earth Planet. In.*, 43, 316-330, doi:10.1016/0031-9201(86)90021-X.

Part IV: Surface expressions of subduction and collision

OROCLINE AND SYNTAXES FORMATION DURING SUBDUCTION AND COLLISION

Flora Bajolet^{(1)*}, Anne Replumaz⁽²⁾, Claudio Faccenna⁽¹⁾, Romain, Lainé⁽²⁾

(1) LET – Laboratory of Experimental Tectonics, Università Roma TRE, Largo S. Leonardo Murialdo, 1, 00146 Rome, Italy.

(2) ISTerre, Université de Grenoble 1, CNRS, F-38041 Grenoble, France.

*Submitted to **Tectonics***

#2012TC003286

Abstract. The present work investigates the formation of curved ranges and syntaxes with scaled laboratory experiments. We simulated the subduction and collision between a continental upper plate and a subducting plate composed of an oceanic lithosphere and a continental indenter comparable to India-Asia configuration. The experiments reveal that the shape of the range (concave, straight or convex) and development of syntaxes are controlled by the trench viscosity, the buoyancy number (F_b) of the upper plate (i.e. thickness and viscosity) and the boundary conditions. Four end-members regimes of the indentation process can be defined depending on the range shape and dynamics of the upper plate. The curvature of the range is convex (toward the subducting plate) with syntaxes for a low viscosity trench and concave without syntaxes for a high viscosity. Convex curvature and syntaxes form by overthrusting of upper plate material on the subducting plate, faster at the center than at the extremities. They are associated with a rather flat slab (underthrusting) during continental collision. A thick and weak upper plate (high F_b) leads to gravity collapse that increases the amplitude of the curvature and lateral escape, similar to the late evolution of the Himalaya-Tibet system. In contrast, low F_b experiments show less pronounced curvatures associated to thickening comparable to the early stages of India-Asia collision. Important lateral decoupling on the sides of the indenter enhances the indentation and produces sharper syntaxes.

1. Introduction

One striking feature of mountain belts worldwide is the diversity of shapes it can adopt. Most of the mountain ranges show a curvature concave toward the overriding plate (e.g. Andes, Alps, Bitlis) or straight (e.g. Pyrenees, Rockies Mountains). On the contrary, the Himalayas shows an original shape convex towards the overriding plate. The overall geometry of the range is more complex, with a large penetration of India far north into the Asian continent and two curves in the trend of the range at both east and west extremities, named large-scale syntaxes (Figure IV.1). This penetration is accommodated by two north-south strike-slip faults: the Sagaing fault to the east and the Chaman fault to the west. India slid north, leaving behind the two lateral oceans subducting beneath Makran to the west and Sumatra to the east. The Tsangpo suture, which is the trace of the Tethys ocean closed between India and Asia, follows the shape of the range. It stretched north-south along the east and west border of the Indian continent and curved towards the overriding plate to the north (Figure IV.1).

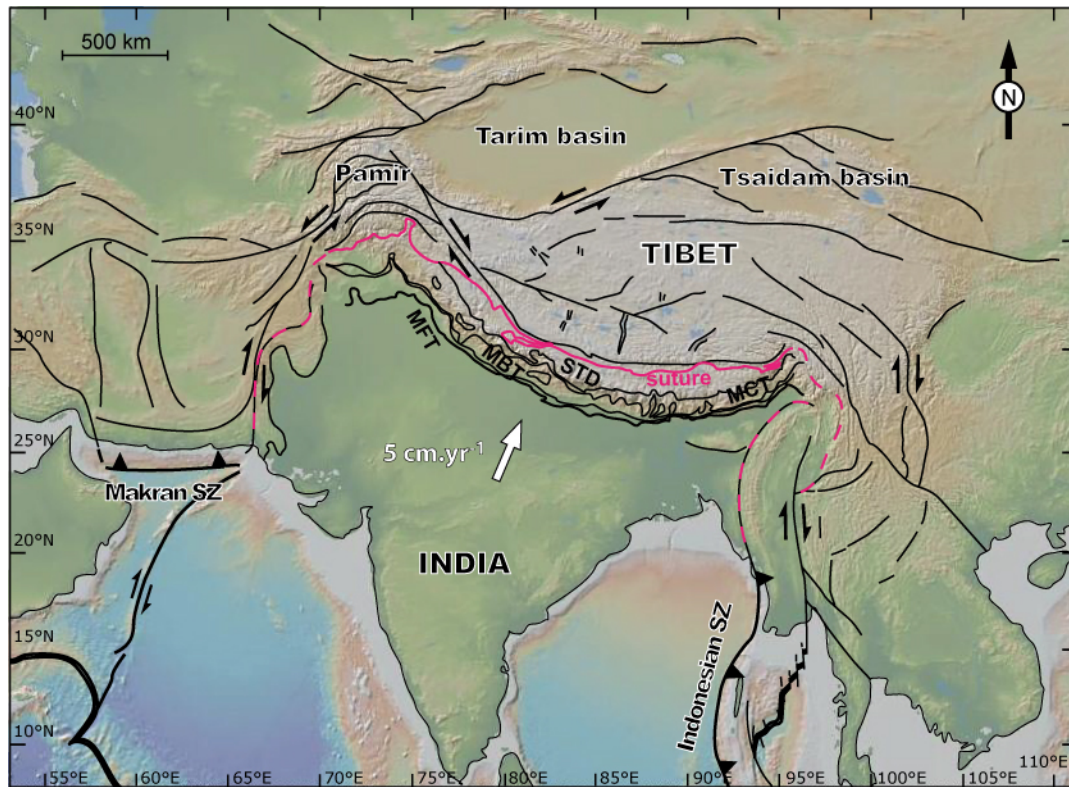


Figure IV.1. Map of the geodynamic context of India-Asia collision. Main faults are drawn in bold and the suture between Indian and Asian plate is underlined in pink. STD: South Tibetan Detachment; MCT: Main Central Thrust; MBT: Main Boundary Thrust; MFT: Main Frontal Thrust; SZ: Subduction Zone.

In detail, the suture shows two small-scale sharp curves around the Nanga Parbat to the west and around the Namche Barwa to the east named small-scale syntaxes. The curvature of the range generates oblique convergence and strain partitioning in the Asian upper plate, which has a fundamental influence on stress pattern and faulting [e.g. Seeber and Pêcher, 1998; McCaffrey and Nabelek, 1998; Mohadjer *et al.*, 2010; Kapp and Guynn, 2004]. However, the origin of the curvature of the Himalayan range remains poorly understood.

The indentation process is driven by a vigorous advance of the Indian plate [Molnar and Stock, 2009]. Mantle tomography shows that pieces of the Indian lithosphere have subducted and that India is overriding its own continental slab [e.g. van der Voo *et al.*, 1999; Replumaz *et al.*, 2010b]. The Indian continental lithosphere has long been considered too buoyant to actively drive subduction, and external forcing, as Indian Ocean ridge push or pull of neighbouring slabs has to be invoked [Chemenda *et al.*, 2000; Li *et al.*, 2008]. Recently, it has been shown that the continental lithosphere of India could lead to a continuous subduction unless India is scraped off its upper crust and part of its lower crust [Capitanio *et al.*, 2011]. It

is the case for the Himalaya which grows up as a sedimentary wedge [e.g. *Malavieille*, 1984], by scrapping of the Indian upper crust along the Main Himalayan Thrust [e.g. *Lavé and Avouac*, 2000]. The subduction process could also be facilitated by the eclogitisation of the lower crust, becoming denser than the mantle, when it bent beneath the Himalaya range [e.g. *Hetenyi et al.*, 2007]. But external forcing has still to be invoked to reproduce the high velocity of the India–Asia convergence, the trench advance and the overriding of the Indian slab. The mantle drag exerted on the base of the lithosphere by a large-scale convective belt with an active upwelling component is likely the main cause for the ongoing indentation of the Indian plate into Eurasia [*Alvarez*, 2010; *Becker and Faccenna*, 2011]. The northward motion of India occurs at about 5 cm yr^{-1} , an almost constant rate since the beginning of the collision about 50 My ago [*Patriat and Achache*, 1984; *Molnar and Stock*, 2009].

The curvature of the trench has been observed in subduction experiments where an oceanic plate subducts under its own weight. The trench curves toward the subducting plate if the slab retreats, or is straight if steep subduction occurs [*Funicello et al.*, 2003; *Stegman et al.*, 2010]. This is consistent with natural examples [*Lallemand et al.*, 2005]. With a continental upper plate, the trench curves towards the subducting oceanic plate if an older thus denser part is introduced in the middle of the subducting plate, while an opposite curvature is obtained with the denser heterogeneity in the upper plate [*Capitanio et al.*, 2011]. But very few studies explore orocline evolution in continental collision settings and most models applied to India-Asia orogen do not include the influence of the subduction process [e.g. *Houseman and England*, 1986] or use a pre-shaped plate boundary with a convex curvature [e.g. *McCaffrey and Nabelek*, 1998; *Seeber and Pêcher*, 1998]. Indentation process has been previously simulated with a rigid, non-deformable indenter therefore preventing any curvature but reproducing lateral escape and extrusion [*Tapponnier et al.*, 1982; *Sokoutis et al.*, 2000; *Rosenberg et al.*, 2007]. *Regard et al.*, [2005] use a deformable subducting plate including lateral variations to explore the links between indentation and subduction dynamics. In that setup, the curvature of the oceanic slab (convex) opposes that of the continental one (concave). In this paper we present analog models performed to simulate in three-dimensions, at the scale of the mantle – lithosphere system, the mechanics of the indentation process for a continental lithosphere. We test (1) which geometry and rheological parameters favor arcuate orogen and syntaxes formation, (2) what are the consequences on the topography and strain of both the orogenic front and the plateau, and (3) how they relate with the subduction/collision dynamics.

2. Model setup and experimental procedure

2.1. Model setup

The model is composed of thin sheets of silicone putty (analog for lithospheres) lying on top of low viscosity glucose syrup simulating the asthenospheric mantle. One silicone layer reproduces the overriding continental plate. The subducting plate is composed of one dense oceanic silicone (analog for Tethys oceans at the front) attached to a light continental indenter (analog for Indian continent). In some experiments, the initial configuration is completed by lateral oceans analog for Makran and Indonesian domains on both sides (Figures IV.1 and IV.2). Silicone putties are visco-elastic materials, quasi-Newtonian at experimental strain rates [Weijermars, 1986] and the glucose syrup a Newtonian fluid. The properties of analog materials are listed in Table IV.1. The subducting plate is attached to a rigid piston advancing at constant velocity and reproducing the convergence between India and Asia. The piston is confined to the upper part of the tank and the glucose syrup is free to move underneath (Figure IV.2).

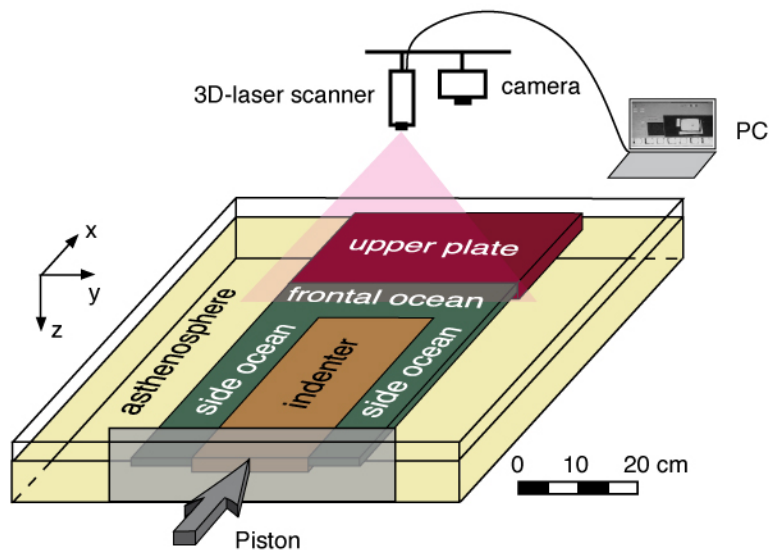


Figure IV.2. Experimental setup. Some experiments were performed only with the frontal ocean, others with both frontal and side oceans (Table IV.3).

Material	Density (kg m ⁻³)	Viscosity ^a (Pa s)
Black ocean	1495	3.4 x 10 ⁴
Indenter (silicone 4)	1411	4.9 x 10 ⁴
Light indenter (silicone 6)	1388	
Black continent	1364	3.2 x 10 ⁴
Weak black continent	1350	3 x 10 ⁴
White continent	967	1 x 10 ⁴
Intermediate syrup (asthenosphere)	1428	22

^aViscosities are given for room temperature (22°C) and an experimental strain rate of 10⁻² s⁻¹ (scaled for nature).

Table IV.1. *Properties of experimental materials.*

The model is placed in a Plexiglas box (75 x 75 x 25 cm³) with the overriding plate attached to the fixed back-wall, far enough from the box sides to minimize boundary effects [Funiciello *et al.*, 2006]. The experiments are properly scaled for gravity, length, density, viscosity and velocity following the method of previous studies [e.g. *Weijermars and Schmeling*, 1986; *Davy and Cobbold*, 1991; *Funiciello et al.*, 2003]. The scaled factor for length is 1.7 x 10⁻⁷ so that 1 cm of the model corresponds to 60 km in nature. The density and viscosity ratios between the oceanic silicone putty and asthenospheric glucose syrup are 1.05 and 1.5 x 10³ respectively. The piston's velocity of 0.54 cm min⁻¹ is scaled to correspond to 5.7 cm yr⁻¹ of convergence in nature, and 1 minute in experiment correspond to 0.55 My in nature. Further details on scaling procedure are presented in Table IV.2.

Our models are performed with the following assumptions and consequent limitations as described in *Funiciello et al.* [2003]: (1) isothermal system (we neglect thermal diffusion and phase changes), (2) the viscosity and density are constant with depth in each individual layer, (3) lack of global background mantle flow, (4) the bottom of the Plexiglas tank simulates the 660 km discontinuity considered as an impermeable barrier.

	Parameter	Nature	Model
g	Gravitational acceleration (m s^{-2})	9.81	9.81
Thickness ^a			
h_c	Continental lithosphere (m)	100000	0.016
h_o	Oceanic lithosphere (m)	70000	0.012
h_{asth}	Upper mantle asthenosphere (m)	660000	0.11
Density			
ρ_c	Continental lithosphere (kg m^3)	3200	1411
ρ_o	Oceanic lithosphere (kg m^3)	3320	1495
ρ_{asth}	Upper mantle asthenosphere (kg m^3)	3220	1428
ρ_c / ρ_{asth}	Density ratio continent	0.99	0.99
ρ_o / ρ_{asth}	Density ratio ocean	1.04	1.05
Viscosity			
η_c	Continental lithosphere (Pa s^{-1})	10^{23}	4.9×10^4
η_o	Oceanic lithosphere (Pa s^{-1})	10^{24}	3.4×10^4
η_{asth}	Upper mantle asthenosphere (Pa s^{-1})	10^{21}	22
η_c / η_{asth}	Viscosity ratio continent	10^2	2.2×10^3
η_o / η_{asth}	Viscosity ratio ocean	10^3	1.5×10^3
Dimensionless parameters		Equivalence model-nature	
t°	Characteristic time: ($t_{\text{model}}/t_{\text{nature}} = (\Delta\rho gh)_{\text{lith nature}} / (\Delta\rho gh)_{\text{lith model}} \times (\eta_{\text{l model}} / \eta_{\text{l nature}})$)	3.46×10^{-12} $1 \text{ min}_{\text{model}} \rightarrow 0.55 \text{ My}_{\text{nature}}$ $1 \text{ h}_{\text{model}} \rightarrow 33 \text{ My}_{\text{nature}}$	
U°	Characteristic velocity: ($U_{\text{model}}/U_{\text{nature}} = t_{\text{nature}} / t_{\text{model}} \times L_{\text{model}} / L_{\text{nature}}$)	49563 $1 \text{ cm h}^{-1}_{\text{model}} \rightarrow 0.18 \text{ cm y}^{-1}_{\text{nature}}$	

^aScale factor for length $L_{\text{model}}/L_{\text{nature}} = 1.7 \times 10^{-7}$.

Table IV.2. *Scaling of parameters for the reference experiment (SH7).*

Each experiment is monitored over its entire duration by top and lateral view photos taken at regular time intervals. Topography evolution is recorded by a laser-scanner (Real Scan USB) whose precision is 0.1 mm corresponding to 600 m in nature. A squared grid of passive markers drawn on the silicone layers enables visualization of the surface deformation.

For representative experiments, we compute the displacement field for a small increment of deformation (over a 1 minute time-step). We used the procedure Cosi-Corr integrated to the software ENVI, made for sub-pixel correlation of images [Leprince *et al.*, 2007; Ayoub *et al.*, 2009]. This procedure correlates one pixel of the picture of step n with one pixel of the picture of step $n+1$ using a window moving across the picture. The result is the displacement field between both steps. We used Cosi-Corr frequency parameters depending on the experiments of 128 or 64 pixels for initial window size (size of initial search zone around the considered pixel), 32 or 16 pixels for final window size, and 16 pixels for step (one measurement each 16 pixels of the picture).

2.2. Forces equilibrium

In collisional systems, the growth and shape of the mountain belt is controlled by the equilibrium between body and boundary forces [England and McKenzie, 1982]. Boundary forces are the driving forces favoring collision, whereas buoyancy forces resist it.

Driving forces

The two main driving forces are the tectonic force (F_t) and the slab pull (F_{sp}). The tectonic force applied at the plate boundary produces the motion of the indenting plate towards the collision zone. In nature, the motion of the indenter could be also supported by far field stress related to plume push [van Hinsbergen *et al.*, 2011], ridge push [Gosh *et al.*, 2010], or mantle drag generated by a large scale convection cell [Alvarez, 2010; Becker and Faccenna, 2011]. In the performed experiments, we simulate the far field stress with a piston pushing the indenter at constant rate. The slab pull force depends on the slab buoyancy given by the density contrast between lithosphere and asthenosphere, and the slab volume (i.e. length and width). The oceanic slab is denser than the asthenosphere and when its length increases as oceanic subduction goes on, F_{sp} becomes more negative (increasing negative buoyancy) favoring extensional backarc basin [e.g. Funicello *et al.*, 2003]. When the lighter continental slab enters the trench and progressively subducts, F_{sp} increases toward positive values (increasing positive buoyancy). Our model setup, considering a mean viscosity for the continental lithosphere lead to a continuous continental subduction, equivalent to the subduction observed after the scraped off the upper crust by Capitanio *et al.* [2011], showing that the force balance is similar. During continental subduction, the trench switches to either stationary or advance regime [Bellahsen *et al.*, 2003; Regard *et al.*, 2003; Magni *et al.*, 2012]. In this case, positive slab pull force may favor continental collision, even though the amount of trench advance is always rather limited [Magni *et al.*, 2012]. Events such as break-off of the dense oceanic root attached to the continental slab favors trench advance and collision [Chemenda *et al.*, 2001; Wortel and Spakman, 2000; Regard *et al.*, 2003; Replumaz *et al.*, 2010b], but is not reproducible with our model setup, and will not be considered in this paper.

Resisting forces

Resisting forces in the system are the force acting at the plate interface depending on coupling (R_f), the bending resistance of the plate (R_b), the resistance to sliding in the mantle (R_s), and the buoyancy of the upper plate (F_b). They depend on the nature of the plates and trench motion, and have been previously quantified in experimental studies [e.g. *Becker et al.*, 1999; *Bellahsen et al.*, 2005; *Funiciello et al.*, 2008]. In our viscous simplified system, R_f is proportional to the plate thickness and the viscosity of the plate interface, considered of the same order as the asthenospheric mantle. The room temperature may vary from one experiment to another causing variations of materials viscosity. The induced change is negligible for silicone putties (maximum 10% of variation for a decrease of 5°C) but not for glucose syrup (130% of variation for a 5°C decrease). The temperature of the glucose syrup (T_s) and corresponding viscosity (η_s) is measured for each experiment (Table IV.3). It corresponds to the viscosity of the trench and influences the lubrication efficiency of the subduction zone. Computations of the shear friction range between 15 and 30 MPa and contribute for about 30% of the energy dissipated during subduction. The viscous dissipation at the trench scales with plate's strength (i.e. viscosity) and thickness and is inversely proportional to the cube of the radius of curvature [*Conrad and Hager*, 1999; *Becker et al.*, 1999]. It may contribute for about 10 to 30% of the energy dissipated during subduction. R_s is represented by the viscous dissipation exerted at the slab-mantle interface during subduction and is directly proportional to the slab surface and asthenosphere viscosity.

The last resisting force is produced by the buoyancy of the continental plate. During continuous thickening, the upper plate stores potential energy with respect to the lowlands (i.e. subducting plate) generating a differential stress. Following *Artyushkov* [1973], *Turcotte* [1982] and *Stein et al.* [1989], the force per unit length due to potential energy scales with the gravity, the density contrast of the upper plate with respect to the mantle and its thickness. This stress can be either supported or not by the strength of the plate itself, which in our case is proportional to its viscosity and strain rate.

Experiment set	Continental plates (upper plate silicone, size in cm) ^a	Size of frontal oceanic plate (cm)	Size of side oceanic plates (cm)	Thickness (cm) ^a	Curvature at 40 min (cm) ^b	Trench temperature (°C)	Trench viscosity (Pa s)	Buoyancy number
SH6	UP (BC): 40x20 Ind: 20x25	40x4	10x25	UP: 0.6 Ind: 1.20 ocean: 1.2	4.3	21	46	0.8
SH7	UP (BC): 40x20 Ind: 20x25	40x7	None	UP: 0.55 Ind: 1.13 ocean: 1.26	1	21.6	42.5	0.7
SH8	UP (BC): 55x20 Ind: 35x25	35x7	None	UP: 0.8 Ind: 1.10 ocean: 1.3	-1.1	23.1	34.5	1.4
SH9	UP (WBC): 40x20 Ind: 20x25	20x7	None	UP: 0.75 Ind: 1.16 ocean: 1.18	-0.2	23.1	34.5	1.7
SH10	UP (WBC): 40x20 Ind: 20x25	20x7	None	UP: 0.58 Ind: 1.2 ocean: 1.18	-0.5	21.9	41.5	1.0
SH11	UP (WBC): 40x20 Ind: 20x25	20x7	None	UP: 0.57 Ind: 1.18 ocean: 1.12	0.8	23.1	35	1
SH12	UP (WBC): 40x20 Ind: 20x25	20x10	None	UP: 0.6 Ind: 1.18 ocean: 1.05	1.6	24	30	1.1
SH13	UP (WC): 40x20 Ind: 20x25	20x7	None	UP: 1.9 Ind: 1.47 ocean: 1.16	-1.3	26.3	18.5	181.4
SH14	UP (WC): 40x20 Ind: 20x37	20x7	None	UP: 0.6 Ind: 1.22 ocean: 1.19	1	22.3	39	18.1
SH15	UP (WC): 40x20 Ind: 20x37	20x7	None	UP: 0.64 Ind: 1.2 ocean: 1.17	1.7	21.8	42	20.8
SH16	No UP Ind: 20x37	20x7	None	Ind: 1. ocean: 1.07		21.2	44.5	
SH17	UP (WC): 40x20 Ind: 20x37	20x7	None	UP: 1.88 Ind: 1.17 ocean: 1.21	0.9	21.5	43.5	177.6
SH18	UP (WC): 40x20 Ind: 20x37	20x5	None	UP: 1.98 Ind: 1.27 ocean: 1.18	-0.4	21.7	42	197
SH19	UP (WC): 40x20 Ind (light): 20x37	20x7	None	UP: 1.9 Ind: 1.28 ocean: 1.28	-0.5	21.3	44.5	181.4
SH20	UP (WC): 40x20 Ind: 20x37	20x7	10x37	UP: 1.93 Ind: 1.22 ocean: 1.15	-1.3	24.2	30	187.2
SH21	UP (WC): 40x20 Ind: 20x37	20x7	10x37 + lateral cuts ^c	UP: 1.90 Ind: 1.27 ocean: 1.26	1	19.8	53	181.4

SH22	UP (BC): 40x20 Ind: 20x37	20x7	None	UP: 0.60 Ind: 1.20 ocean: 1.14	-1.9	24.1	29.5	0.8
SH23	UP (sil. 4): 40x20 Ind: 20x37	20x7	None	UP: 0.56 Ind: 1.20 ocean: 1.16	-1.6	24.2	29	0.1

^a UP: upper plate; Ind: indenter; BC: Black continent; WBC: weak black continent; WC: white continent.

^b Curvature is measured as shown on Figure IV.1. The value is positive when it is concave (toward the North), and negative when it is convex (toward the South).

^c In experiment SH21, we cut between lateral oceans and indenter to allow free motion along this limit.

Table IV.3. *Experimental parameters for each experiment.*

Buoyancy number

The adimensional ratio between the buoyancy ($\Delta\rho g H$) and its resistance ($\eta d\varepsilon/dt$) can be expressed as a buoyancy number (F_b), similar to the Argand number [England and McKenzie, 1982]. This number is expected to vary with time during progressive thickening or thinning of the plate, and can be written as

$$F_b = \Delta\rho g H_i f / (\eta d\varepsilon/dt) \quad (1)$$

where $\Delta\rho$ is the density contrast between the upper plate and the asthenosphere, g the gravity acceleration, H_i and η the initial thickness and viscosity of the plate respectively, $d\varepsilon/dt$ the experimental strain rate, and f the thickening factor measured in the center of the upper plate.

The strain rate is calculated as

$$d\varepsilon/dt = v / H_i \quad (2)$$

where v is the piston velocity. The thickening factor allows us to estimate the evolution of the buoyancy number through time and is calculated as

$$f = H_f / H_i \quad (3)$$

where H_f is the thickness at the considered stage. From equations (2) and (3), (1) is equivalent to

$$F_b = \Delta\rho g H_i H_f / \eta v \quad (4)$$

3. Experimental results: generating curvature and syntaxes

We performed 21 experiments varying geometrical and rheological parameters and selected 16 whose characteristics are listed in Table IV.3. By analogy with India-Asia collision, we shall refer thereafter to regions of the experiment in terms of geographical

directions, the southern boundary corresponding to the piston that is moving toward the north (i.e. from left to right in all figures).

For each experiment, we observed 3 successive processes, the subduction of the frontal ocean, the subduction of the light continental indenter pulled by the denser oceanic slab, and finally the continental collision when the continental lithosphere stops sinking vertically into the mantle. We classified the experiments in different sets. The first set includes experiments with a buoyancy number of 0.5 to 3 favoring the thickening of the upper plate, the second set experiments with a buoyancy number of 20 to 170 favoring the lateral escape of the upper plate, and the third set includes experiments with lateral oceans on each the side of the indenter simulating Makran and Indonesian subduction zones. In each set, we tested the influence of the viscosity of the upper plate and efficiency of the subduction.

We first present three experiments from the first set. SH7 is our reference experiment (Table IV.3).

3.1. First set (low F_b), high viscosity asthenosphere (SH7)

The reference experiment SH7 is composed of a upper plate (“black continent” silicone) of $40 \times 20 \times 0.55 \text{ cm}^3$, and a subducting plate made of a continental indenter of $20 \times 25 \times 1.13 \text{ cm}^3$ (Figure IV.1). The piston pushes the subducting plate at a rate of 0.54 cm min^{-1} corresponding to 5.7 cm yr^{-1} in nature. The buoyancy number at the onset of the experiment is 0.7 (Table IV.3). The viscosity of the trench is 42.5 Pa s corresponding to a poorly lubricated trench.

The experiment starts by the subduction of the oceanic silicone located at the front of the subducting plate accompanied by trench retreat (Figure IV.3). Subduction is driven by the negative buoyancy of the slab and by the push of the advancing piston. The trench gently curves toward the south (Figure IV.3ae) due to active toroidal flow around the corners of the downgoing plate producing along strike variations in subduction velocity [Funicello *et al.* 2006]. Importantly, it generates a small perturbation at each extremity of the downgoing plate, similar to a proto-syntaxis. At the beginning of continental subduction, buoyant material enters at the trench and changes the force equilibrium: slab pull decreases in amplitude (Figure IV.3e) and the trench advances. The curvature remains oriented toward the subducting plate during early continental subduction (Figure IV.3e). When slab pull approaches zero, subduction becomes less efficient and the trench adopts a straight shape (Figure IV.3b), which progressively reverses to form a concave arc without syntaxes (Figure IV.3c). Finally, when the buoyancy of the slab becomes positive, the trench locks, no more material subducts and

continental collision initiates. The curvature amplifies during the continental collision phase. It generates an indentation opposite to the Himalayan curvature without any syntax.

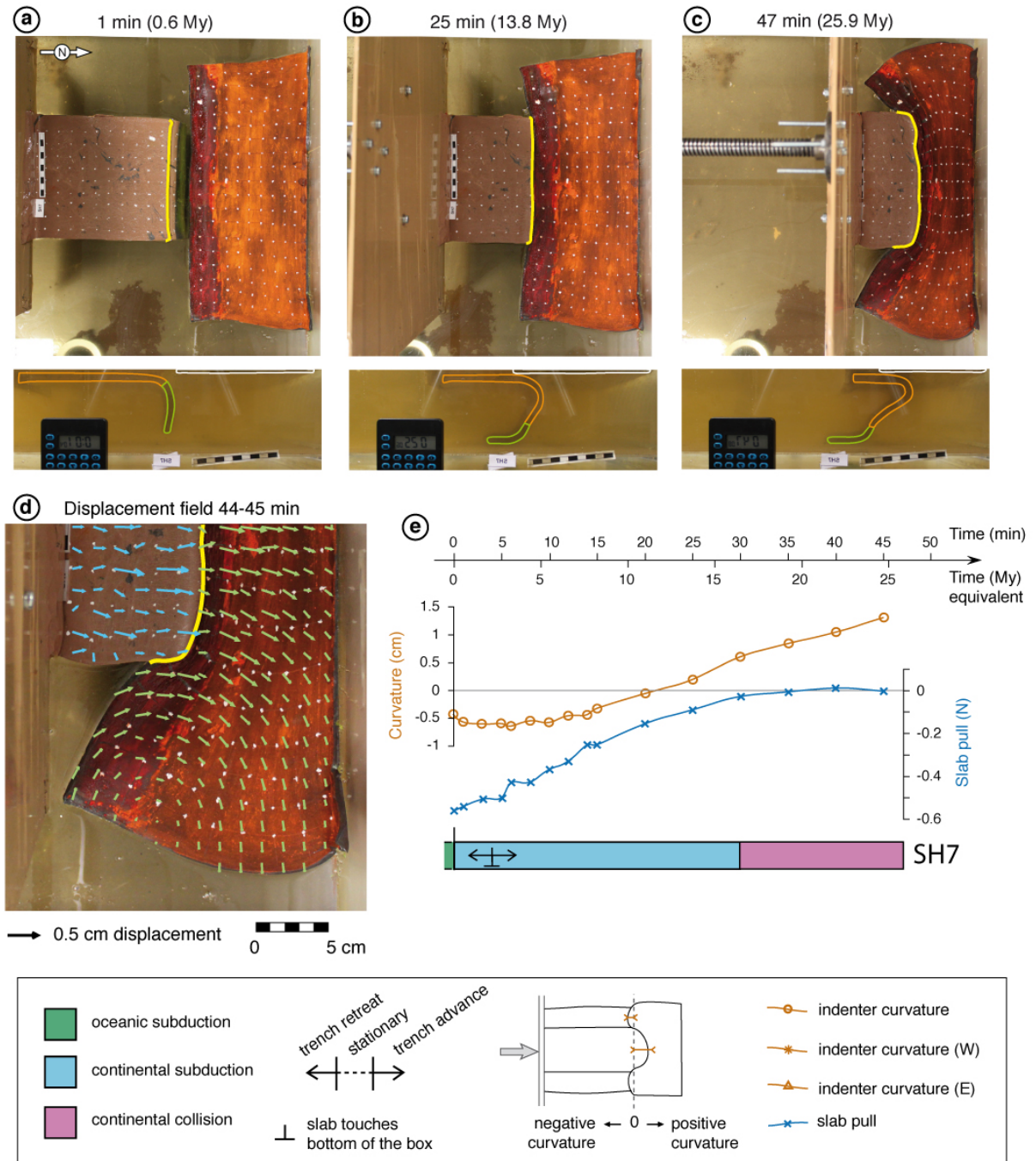


Figure IV.3. (a, b and c) Top and side views photos of experiment SH7 at 1 min, 25 min and 47 min respectively. On top views, the solid yellow line highlights trench location and shape. On side views, oceanic slab is underlined in green, continental slab in orange, upper plate in white. (d) Displacement field computed with Cossi-Corr plugin (see text for details) over a 1-minute time-step. (e) Timeline illustrating the main phases of subduction and collision, with

evolution of curvature and slab pull over time. The amplitude of curvature is measured as shown on the sketch in the legend. Curvature is positive when concave, negative when convex.

The displacement field in the upper plate is dominated by N-S shortening in the center of the model that rotates NW-SE and NE-SW in the northwestern and northeastern corners respectively (Figure IV.3d). We measure the partitioning of the convergence along a mid north-south line after 40 minutes of piston advance. The N-S shortening of the upper plate (S_{up}) is calculated as the difference between final and initial lengths (L_{upf} and L_{upi} respectively)

$$S_{up} = L_{upf} - L_{upi} \quad (5)$$

For the shortening of the subducting indenter (S_i), we take into account the length of the continental slab (L_{cs}) such as

$$S_i = L_{if} + L_{cs} - L_{ii} \quad (6)$$

Where L_{ii} and L_{if} are the initial and final lengths of the indenter respectively.

The total shortening due to the piston advance (S_p) is calculated as

$$S_p = v t \quad (7)$$

Where v is the piston velocity (0.54 cm min^{-1}) and t the time step at which we calculate the partitioning of the convergence (40 min).

The percentage of convergence accommodated by shortening of the upper plate (P_{up}) is

$$P_{up} = 100 S_{up} / S_p \quad (8)$$

The same expression apply for the indenter

$$P_i = 100 S_i / S_p \quad (9)$$

The remaining part of N-S convergence that is not accommodated by shortening of the plates is due to subduction.

We conclude that in the north-south direction, the convergence is accommodated at 52% by continental subduction, 38% by shortening of the upper plate and 10% by shortening of the indenter.

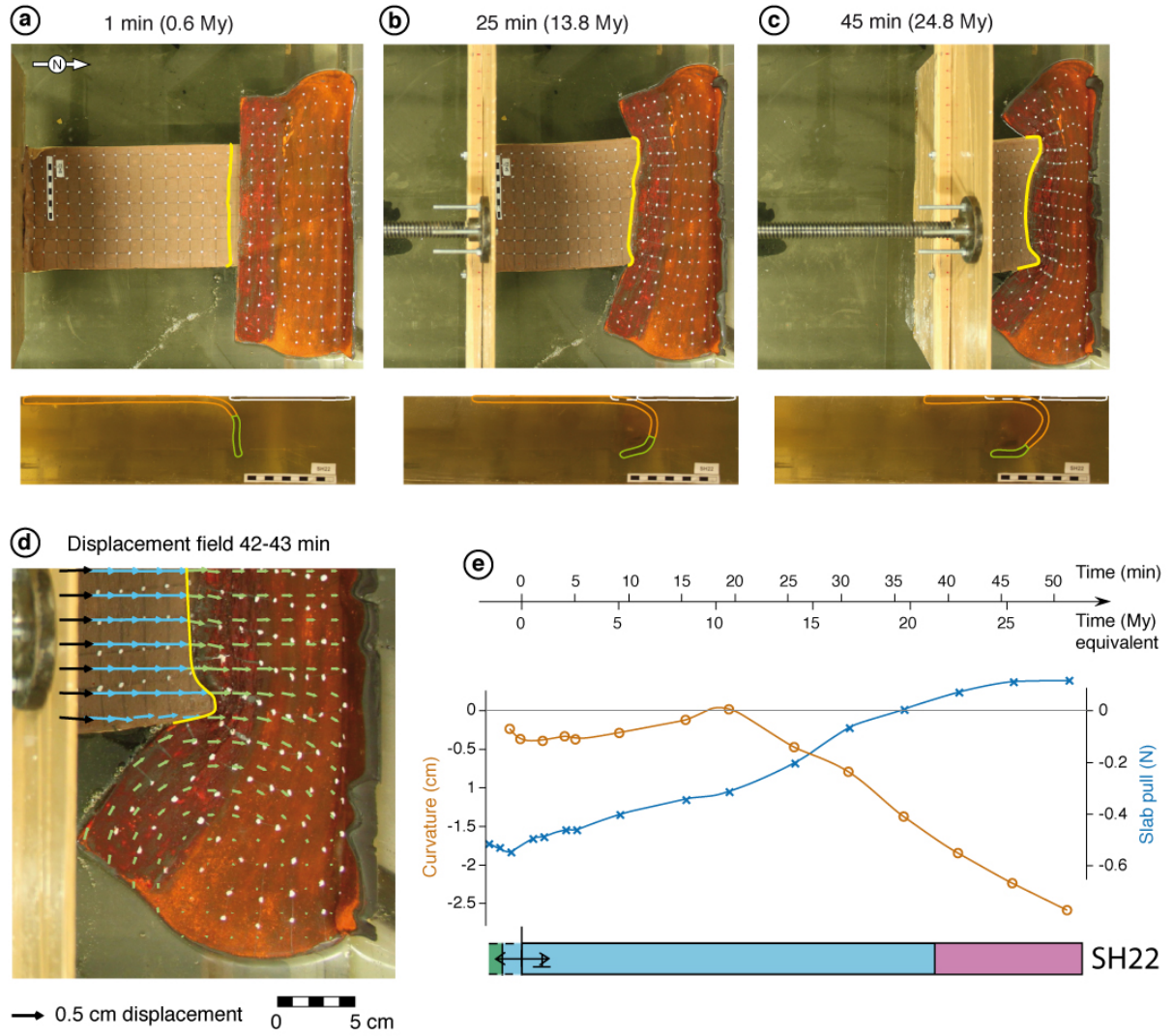


Figure IV.4. (a, b and c) Top and side views photos of experiment SH22 at 1 min, 25 min and 45 min respectively. (d) Displacement field. (e) Timeline, curvature and slab pull evolution. Legend is the same as for Figure IV.3.

3.2. First set (low F_b), low viscosity asthenosphere (SH22)

Experiment SH22 has a buoyancy number similar to SH7 ($F_b = 0.8$) but differs by a higher temperature of the glucose syrup. The viscosity of the syrup is thus lower which generates a more efficient lubrication of the trench. The early evolution is the same as SH7: the trench forms a convex arc during oceanic subduction, with a proto-syntaxis at each extremity (Figure IV.4ae). As for SH7, the early convex curvature decreases slowly during continental subduction, and reaches an almost straight shape while the proto-syntaxes perpetuate, although smaller in amplitude (Figure IV.4e). The trench did not locked at the

onset of collision as in experiment SH7, and the continental subduction is continuous. The slab pull increases continuously, and when it approaches a positive value at ca. 20 minutes (11 My), the trend reverses and both the curvature and proto-syntaxes amplify forming an orocline convex toward the south (Figure IV.4be). Although the slab does not sink vertically anymore, a little amount of continent is forced to subduct forming a rather flat slab in late stages (underthrusting). The more efficient lubrication of the trench allows more continent to subduct despite the positive buoyancy of the slab, driven by the push of the piston combined with the anchor of the oceanic slab. The displacement field in the upper plate is as for SH7 dominated by N-S shortening in front of the indenter that rotates laterally on each side (Figure IV.4d). The difference in N-S shortening between the center of indenter and its sides results in a relative transversal flow of upper plate material overthrusting the subducting plate. This transversal flow enhances the convex orocline and the development of syntaxes during collision (Figure IV.4ce).

After 40 min of experiment (equivalent to 22 My), the convergence has been accommodated in the N-S direction at 41% by subduction, 36% by shortening of the upper plate and 23% by that of the indenter.

3.3 First set (low F_b), low viscosity asthenosphere, weak upper plate (SH9)

Experiment SH9 is similar to SH22 but performed with a weaker upper plate to test the influence of its viscosity (Table IV.3). The early stages of oceanic and continental subduction are similar to that of experiment SH22 with the formation of proto-syntaxes and a convex arcuate trench (Figure IV.5a), which progressively straightens during late continental subduction (Figure IV.5be). However, unlike SH22, it goes through an episode of concave orocline correlating with an almost zero slab pull force (neutral buoyancy; Figure IV.5e). Similarly to SH22, when the slab pull reaches positive values the curvature evolution reverses to a convex shape that is amplified during continental collision (Figure IV.5ce). The upper plate undergoes N-S shortening at the orogenic front, E-W extension in all the plate and rotation at the free edges as shown on the velocity field (Figure IV.5d), similar to that of SH22. After 40 min of experiment (22 My), 54% of the convergence has been accommodated at the trench, 26% by N-S shortening of the upper plate, 20% by that of the indenter.

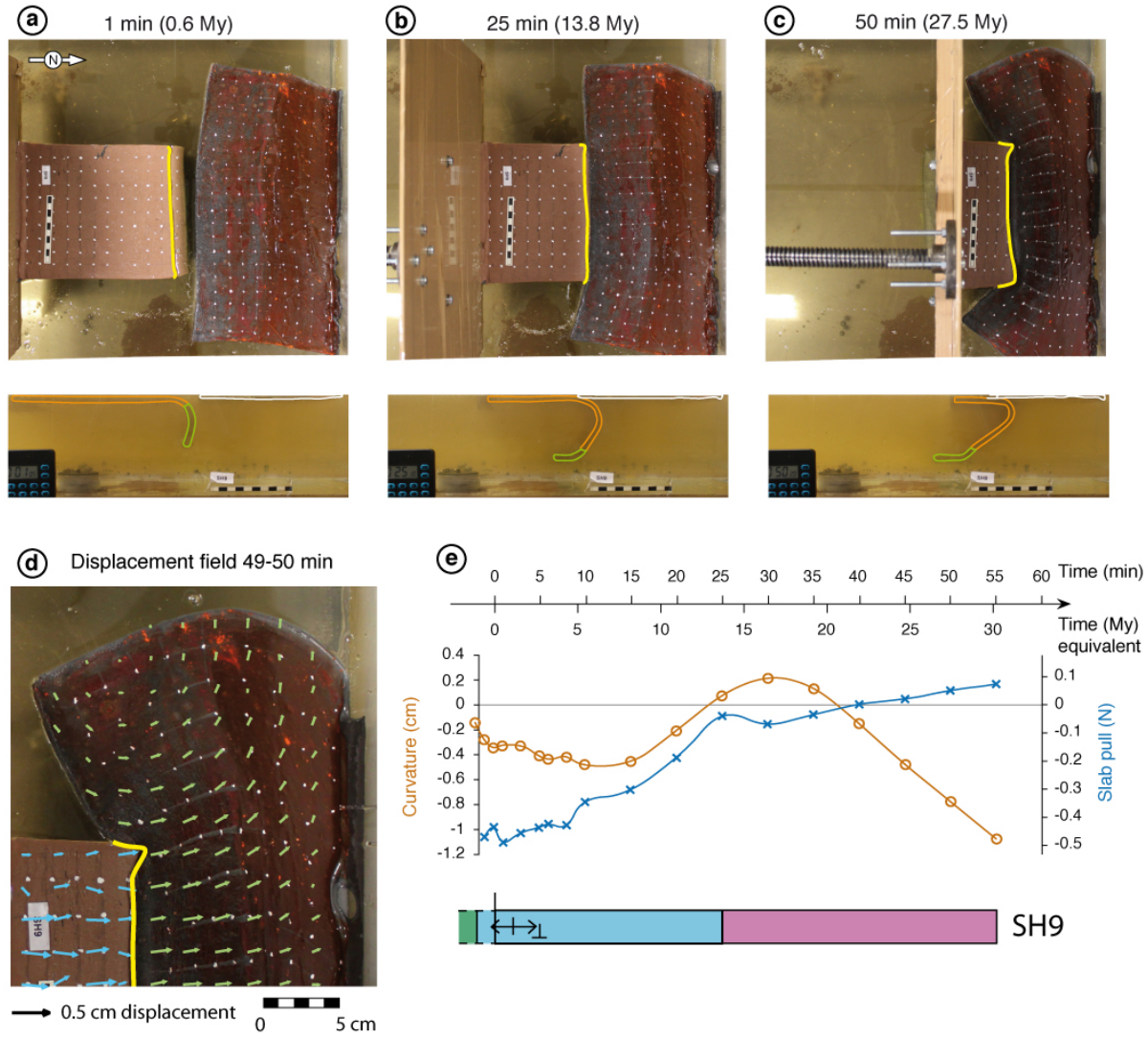


Figure IV.5. (a, b and c) Top and side views photos of experiment SH9 at 1 min, 25 min and 50 min respectively. (d) Displacement field. (e) Timeline, curvature and slab pull evolution. Legend is the same as for Figure IV.3.

3.4. Second set (high F_b), high viscosity asthenosphere, weak upper plate (SH15)

In experiment SH15, we used a upper plate three time weaker than for SH7 to further explore the influence of rheology. This experiment has a high buoyancy number ($F_b = 20.8$). The main effect of the weaker silicone is to favor gravitational collapse (Figure IV.6). The viscosity of the trench is 42 Pa s leading to poor lubrication.

The subduction stage is rather different from SH7, with a constant straight shape of the trench in early stages. When the slab pull approaches zero (neutral buoyancy of the slab), the trench curves concavely. During collision, the orocline grows and produces a moderate

indentation (Figure IV.6). Despite a viscosity of the upper plate lower than for SH9, the poor lubrication of the trench prevents efficient overthrusting and relative transversal flow. The final curvature is concave and no syntaxes are formed, similar to that of experiment SH7. The orogenic front is characterized by N-S shortening while lateral escape and rotation predominate at the edges of the upper plate (Figure IV.6d). The total thickening is lower than for first set experiments and compensated by a larger amount of lateral escape. The subduction undertakes 62% of the convergence, N-S shortening of the upper plate 28% and N-S shortening of the indenter 10%.

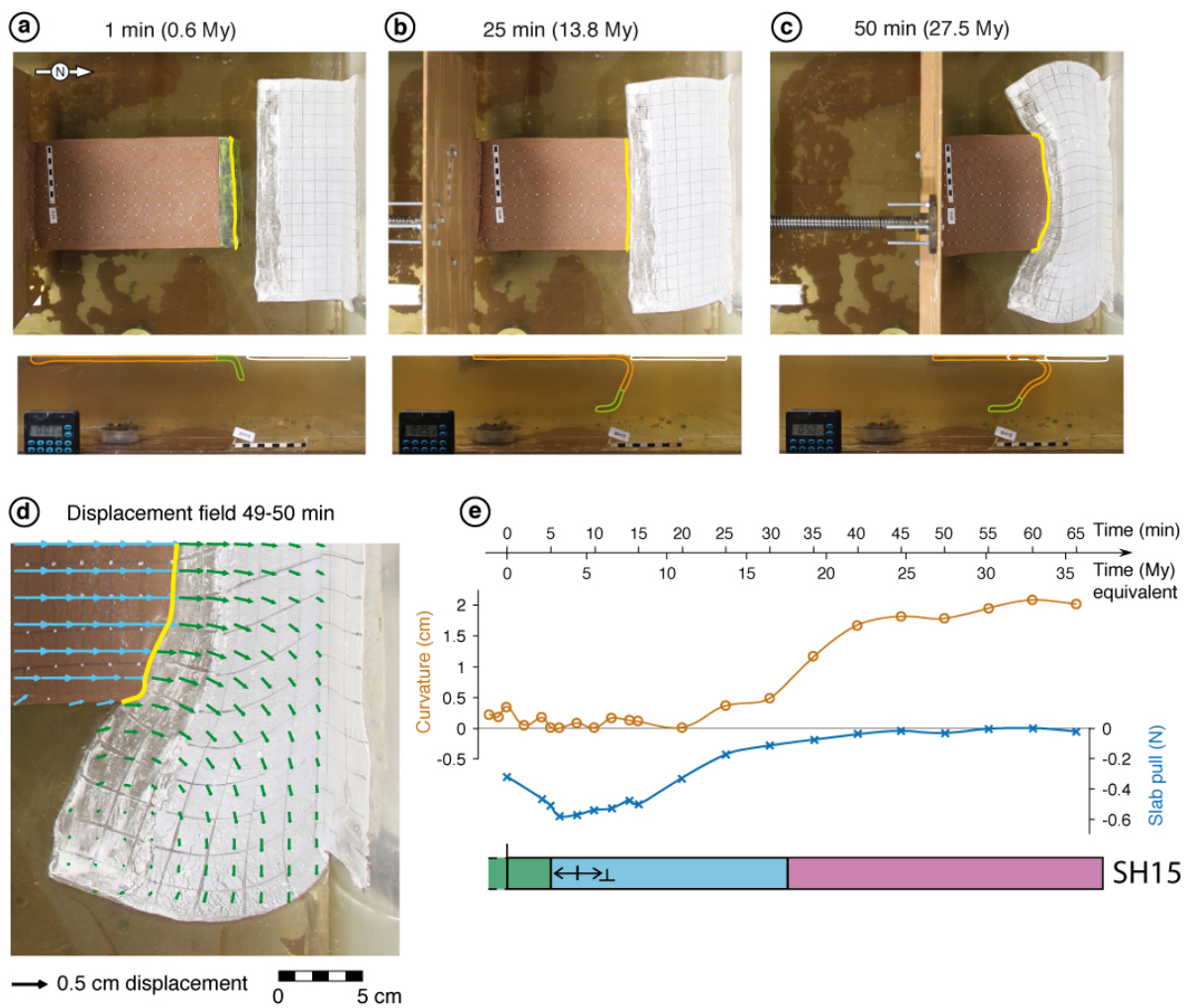


Figure IV.6. (a, b and c) Top and side views photos of experiment SH15 at 1 min, 25 min and 50 min respectively. (d) Displacement field. (e) Timeline, curvature and slab pull evolution. Legend is the same as for Figure IV.3.

3.5. Second set (high F_b), low viscosity asthenosphere, thick and weak upper plate (SH13)

Experiment SH13 has among the highest buoyancy number ($F_b = 181.4$), due to thicker upper plate compared to SH15 (Table IV.3). The viscosity of the trench is 18.5 Pa s leading to good lubrication.

As in reference experiment SH7, the trench forms a convex arc during oceanic subduction and early continental subduction (Figure IV.7ae). Due to an experimental bias (the silicones of the subducting and upper plate stick together in one point on the eastern part of the trench), the evolution then becomes asymmetric. Only one syntaxis forms on the western corner of the downgoing plate, where the subduction is continuous. The eastern half of the trench, where the trench locks, curves concavely. For both sides, the major change in curvature orientation occurs when, or soon after, the buoyancy reaches positive values (Figure IV.7ce). In the region of convex orocline, the curvature rapidly accentuates during continental collision as the relative transversal flow is amplified by a collapse of the overriding plate over the subducting plate (as observed in the first set). This overthrusting and the final convex curvature are more pronounced than in previous experiments due to the higher buoyancy number (i.e. higher gravitational potential energy).

The collapse dynamics of the system is confirmed by the displacement field that indicates global E-W extension on a large area of the upper plate (Figure IV.7d). As a consequence, most of the convergence is accommodated by subduction (83%), only 10% by N-S shortening of the upper plate, and 7% by that of the indenter.

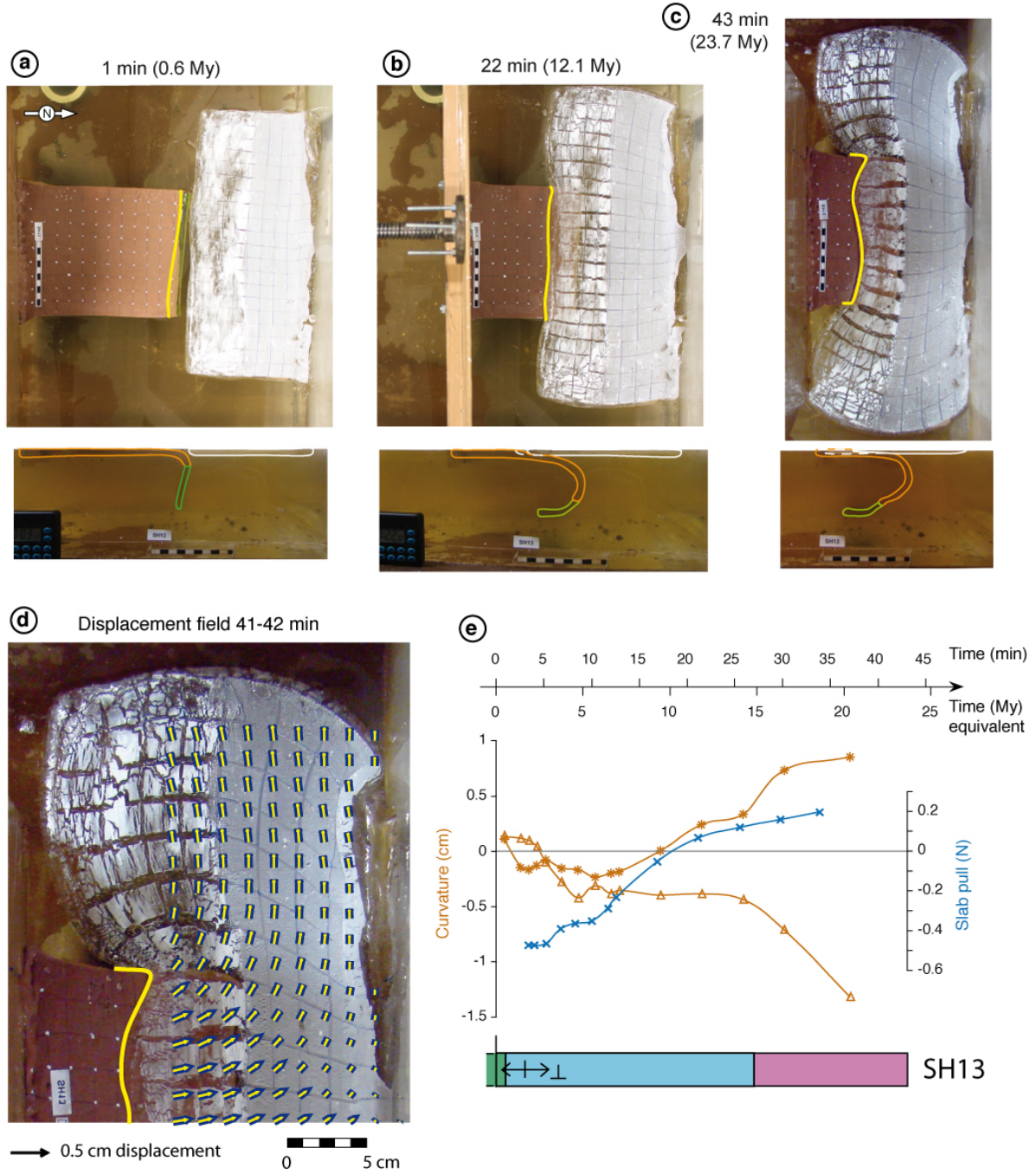


Figure IV.7. (a, b and c) Top and side views photos of experiment SH13 at 1 min, 22 min and 43 min respectively. (d) Displacement field. (e) Timeline, curvature and slab pull evolution. Legend is the same as for Figure IV.3.

3.6. Third set (lateral oceans), low F_b , high viscosity asthenosphere (SH6)

In the third set, we add lateral oceans to the indenter (Figure IV.2). We will present two end-member cases: one with a low buoyancy number and poorly lubricated trench (SH6; Figure IV.8), the other with a high buoyancy number and well lubricated trench (SH20; Figure IV.9).

In experiment SH6, the upper plate is made of black silicone identical to that of SH7 (Table IV.3). The buoyancy number is low ($F_b = 0.78$) and the trench viscosity is high (46 Pa s) leading to poor lubrication.

The experiment starts by the subduction of the oceanic silicone located at the front of the subducting plate accompanied by trench retreat. The trench acquires a slightly concave shape during this phase as trench retreat is faster on the sides (Figure IV.8a). This curvature is then accentuated during the continental subduction stage. Oceanic subduction proceeds on the sides while lighter indenter (continent) is subducted at the center. Entrance of buoyant material at the trench changes the force equilibrium: slab pull continues to increase on the sides that still undergo trench retreat, but decreases at the center that switches to trench advance. The difference in slab pull force and hence trench motion lead to a more pronounced concave curvature (Figure IV.8b). The orocline shape is finally amplified all along the continental collision phase (Figure IV.8ce) and generates a large indentation (ca. 40% of the final length) opposite to the Himalayan curvature; no syntaxes are formed.

The displacement field in the upper plate is dominated by N-S shortening in the center of the model that rotates NW-SE and NE-SW in the northwestern and northeastern corners respectively (Figure IV.8d). However, the rotational component is less important than in experiments without side oceans. After 40 min of experiment (22 My), the convergence has been undertaken at 62% by the subduction and 38% by shortening of the upper plate.

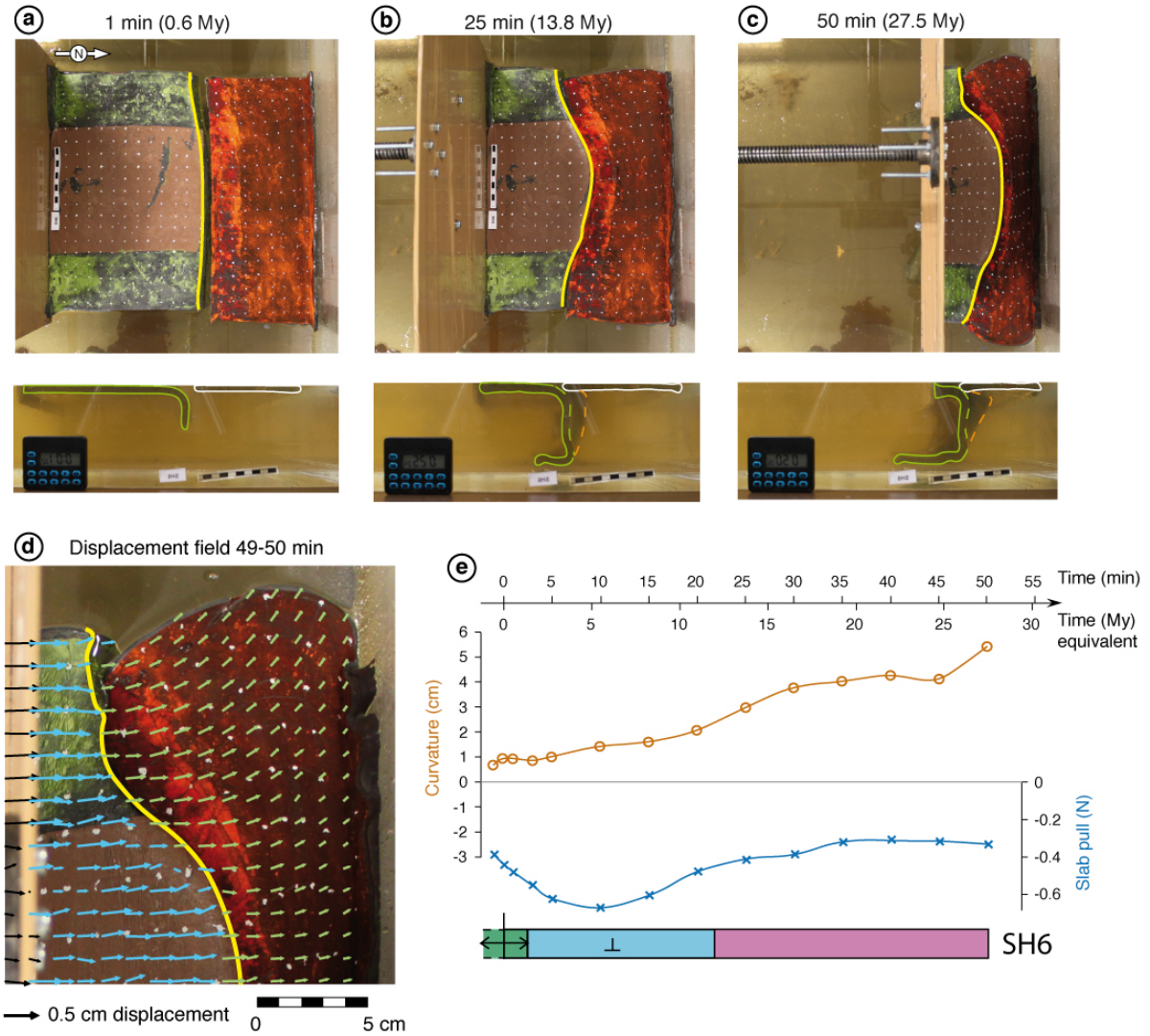


Figure IV.8. (a, b and c) Top and side views photos of experiment SH6 at 1 min, 25 min and 50 min respectively. (d) Displacement field. (e) Timeline, curvature and slab pull evolution. Legend is the same as for Figure IV.3.

3.7. Third set (lateral oceans), high F_b , low viscosity asthenosphere (SH20)

Experiment SH20, is performed with a weak upper plate (white continent) as thick as SH13, that is three times thicker than SH15 (Table IV.3). This experiment has the highest buoyancy number ($F_b = 187$), almost 10 time that of SH15, similar to SH13. The viscosity of the trench is 44.5 Pa s, leading to poor lubrication.

The stages of oceanic subduction and early continental subduction are comparable to SH6 with a difference in trench velocity between the center (light, continent) and the sides (dense, oceanic) leading to a concave orocline (Figure IV.9ae). However, the curvature of the

indenter reverses rapidly and becomes convex toward the south as the overriding plate overthrusts the center of the continent. Between lateral oceans subducting vertically, and the overflowed center of the continent, the edges of the continent form proto-syntaxes (Figure IV.9c). This change is amplified during continental collision as slab pull approaches zero. At the end of the experiment, we observe two syntaxes wider than in experiments without side oceans (Figure IV.9ce). The upper plate also undergoes pronounced lateral flow (Table IV.3).

Deformation of the upper plate is dominated by N-S shortening and E-W lateral escape. We also observe a very limited rotation of the extremities of the upper plate (Figure IV.9d).

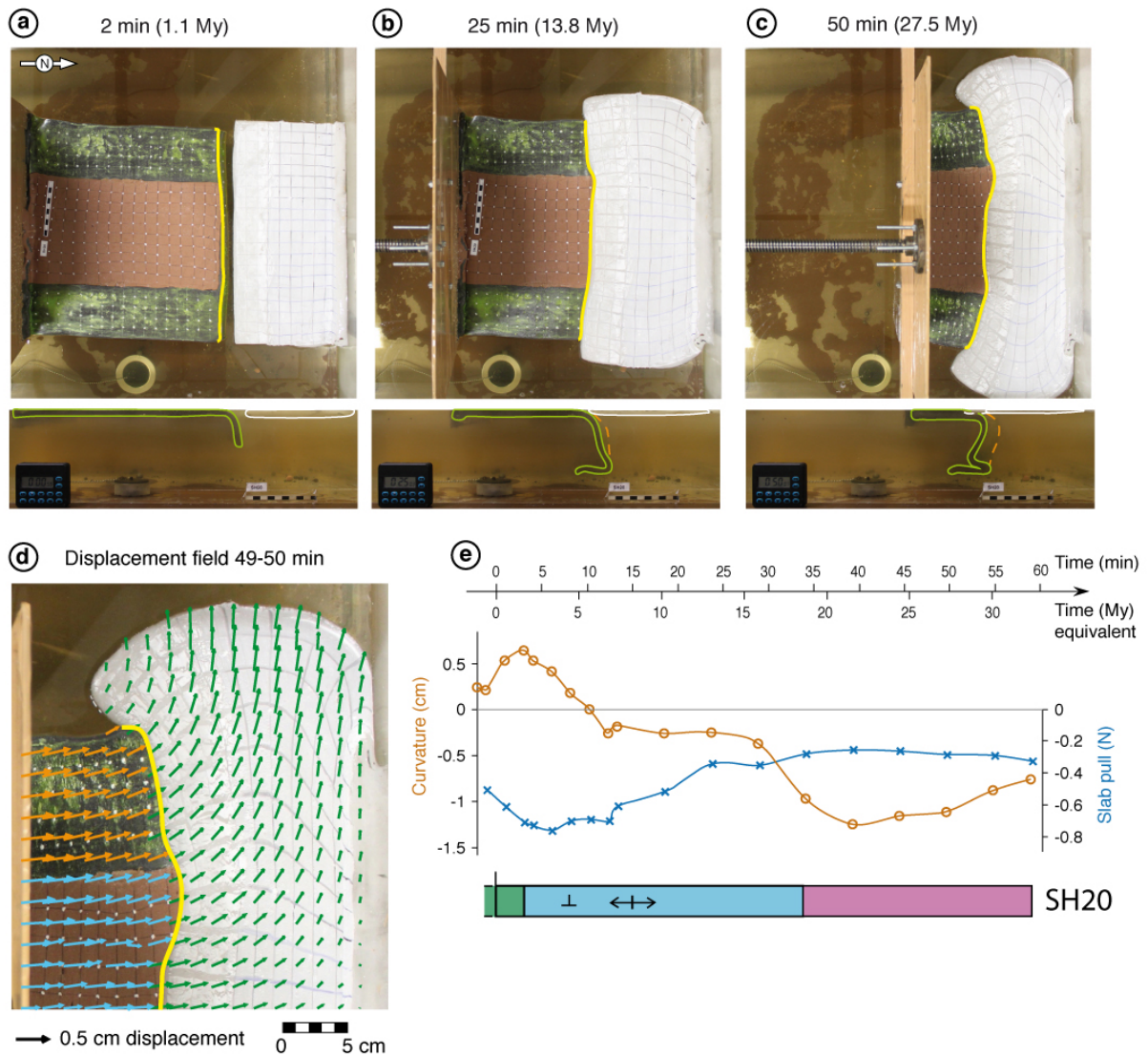


Figure IV.9. (a, b and c) Top and side views photos of experiment SH20 at 2 min, 25 min and 50 min respectively. (d) Displacement field. (e) Timeline, curvature and slab pull evolution. Legend is the same as for Figure IV.3.

4. Discussion: range shape evolution

The continental lithosphere has long been considered too buoyant to subduct on its own, and even attached to a dense oceanic slab, break-off should occur once the continent entered the trench [Wong and Wortel, 1997; Chemenda *et al.*, 2000; Regard *et al.*, 2003]. However by correlating the positive wavespeed tomographic anomalies with the position of the suture through time, it has been shown that pieces of the Indian continent have subducted in the mantle [Replumaz *et al.*, 2010a]. Our models successfully reproduce continuous continental subduction and collision with a light indenter attached to a dense oceanic plate as shown in numerical model with a continent scraped off its upper crust and part of its lower crust [Capitanio *et al.*, 2011]. Proto-syntaxes at each extremity of the subducting plate and slight convex curvature initiate during continental subduction that either grow or is repressed during collision. This evolution and the final amplitude of the curvature appear to be controlled by three main parameters: the efficiency of the subduction correlated to the trench viscosity, the buoyancy number of the upper plate, and the lateral decoupling.

4.1. Subduction efficiency

If the viscosity of the trench, corresponding to the viscosity of the asthenosphere, is high ($> 35 \text{ Pa s}$), the subduction interface is poorly lubricated. The continental subduction will tend to lock early and proto-syntaxes will be annealed while the concave curvature appears (Figures IV.3, IV.6, and IV.8). On the contrary, if the viscosity of the trench is low ($< 35 \text{ Pa s}$), the subduction interface is highly lubricated. A more efficient lubrication of the trench allows more continent to subduct, driven by the push of the piston combined with the anchor of the oceanic slab. The slab pull increases continuously, and when it approaches a positive value the trend reverses and both the curvature and proto-syntaxes are amplified forming an orocline convex toward the south (Figures IV.4, IV.5, IV.7, and IV.9). The continuity of the subduction process coupled with the positive slab pull generate a convex curvature.

Such a curvature has been observed when an oceanic plate subducts under its own weight and collapse, generating a toroidal flow which makes the trench curves toward the subducting plate [Funicello *et al.*, 2003; Stegman *et al.*, 2010]. Such a flow could not be invoked for a continental subduction, as the trench advances continuously and the mantle flow is forward (Figures IV.3 to IV.9).

We can illustrate the effect of subduction efficiency on range shape by plotting the normalized continental slab length (L_{sn}) versus curvature at a certain time (Figure IV.11a).

The normalized continental slab length is obtained by dividing the continental slab length (L_s) by the total thickness of glucose syrup in the tank (t_s). After 40 min, the experiments showing a convex curvature are those with $L_s > 10 \pm 1$. This efficient subduction is obtained only in experiments with well lubricated trench. Side view pictures of these experiments reveal a larger radius of curvature of the subducting plate compared to experiments with concave range (Figures IV.4c, IV.5c, IV.7c, and IV.9c). Moreover, we observe that the change from straight to convex curvature often occurs when the force balance reaches or is close to neutral buoyancy of the slab (e.g. Figures IV.4e and IV.5e). When this threshold is attained, the subducting plate adopts a larger radius of curvature and underthrusts the upper one at a flat angle. A part of the convergence previously undertaken by the subduction is accommodated by overthrusting of the upper plate on the indenter. The transfer from vertical motion (sinking slab) to horizontal one (relative transversal flow/underthrusting) results in a convex orocline.

If the subduction stops, the radius of curvature of the slab is small, and the underthrusting of the subducting plate is reduced. The upper plate does not overthrust the indenter nor curves convexly.

A particular case can occur when the trench partially locked on one side because of local adhesion of the plates. The trench shape becomes asymmetric, with one convex syntaxis where the subduction is continuous, and one concave curve where the trench is locked (Figure IV.7).

4.2. Buoyancy number

The buoyancy number, depending mainly on the thickness and viscosity of the upper plate, is responsible for the amplitude and timing of syntaxes and curvature formation. During convergence, the upper plate undergoes a competition between thickening and collapse. The collapse generates both lateral escape (E-W extrusion) and N-S overthrusting. Syntaxes and convex curvature develop if the relative transversal flow toward the subducting plate is larger at the center of the indenter than on its sides.

The lower the buoyancy number is, the more stable the upper plate is. Three-dimensional strain analysis (Appendix A) performed on a typical experiment (SH9; presented in Figure IV.5) reveals vertical flattening in the central area of the upper plate, with λ_1 vertical and λ_3 orogen-normal. The most external parts are characterized by plane strain to slight horizontal constriction (Figure IV.10a). This is coherent with the velocity field showing N-S displacements in the central area and E-W extrusion and rotation in external areas (Figure IV.5d). In summary, a low F_b (thin and/or strong upper plate) favors the thickening of the

upper plate, especially in front of the indenter (Figures IV.3, IV.4, IV.5 and IV.8). Formation of convex curvature and syntaxes is possible if the trench is well lubricated, but amplitude of overthrusting will be small. In that case, both the convex shape of the suture and the thickening of the upper plate are compatible with the Tsangpo suture and thick crust of the Tibetan Plateau.

The higher the buoyancy number is, the more unstable the upper plate is. A high F_b favors gravitational collapse expressed by lateral escape and relative transversal flow (Figure IV.10). The strain in the upper plate is typically that of experiment SH13 (presented in Figure IV.7) characterized by a λ_1 orogen-parallel and a λ_3 vertical. The central area deforms by horizontal constriction while external parts undergo horizontal flattening (Figure IV.10b). This analysis confirms the strong lateral component observed in the velocity field (Figure IV.7d). To summarize, for a thick and/or low viscosity upper plate convergence is more accommodated by a very efficient lateral spreading that reduces the amount of thickening and can lead to vertical thinning. A well lubricated trench favors the overthrusting of the upper plate on the indenter. This dynamic generates a convex curvature and syntaxes of large amplitude compared to experiments with low F_b (e.g. Figures IV.7 and IV.9). These results are consistent with thin-viscous-sheet models showing a more important range curvature for upper plates of higher gravitational potential energy [Copley, 2012]. However, we also observe that the final shape of the trench is less pronounced for experiment SH9 (Figure IV.5; $F_b = 1.7$) than for SH22 (Figure IV.4; $F_b = 0.8$). That can be explained by the temporary stage of concave orocline in SH9 evolution, absent in the case of SH22, that delays the development of convex curvature. The slight difference of trench viscosity (34.5 Pa s for SH9, 29.5 for SH22) could also explain the lower amplitude of the curvature. In the case of high F_b , the convex shape of the suture is compatible with the Tsangpo suture but the upper plate is thinning unlike the Tibetan Plateau.

The buoyancy number also influences the timing of syntaxes formation. In all experiments, there is a competition between thickening and lateral escape. High F_b leads to important lateral escape that inhibits thickening and N-S overthrusting compared to low F_b experiments. Consequently, a larger amount of convergence is required to reach a similar range shape. Figure IV.11b shows the buoyancy number plotted against the normalized continental slab length. The dotted line representing the amount of subduction after which syntaxes form is shifted toward larger values for high F_b experiments. In other words, syntaxes and thus convex curvature appear later. To summarize, for low F_b experiments

syntaxes and curvature are of small amplitude and form early in the collision history, while for high F_b experiments they have a larger amplitude and appears later.

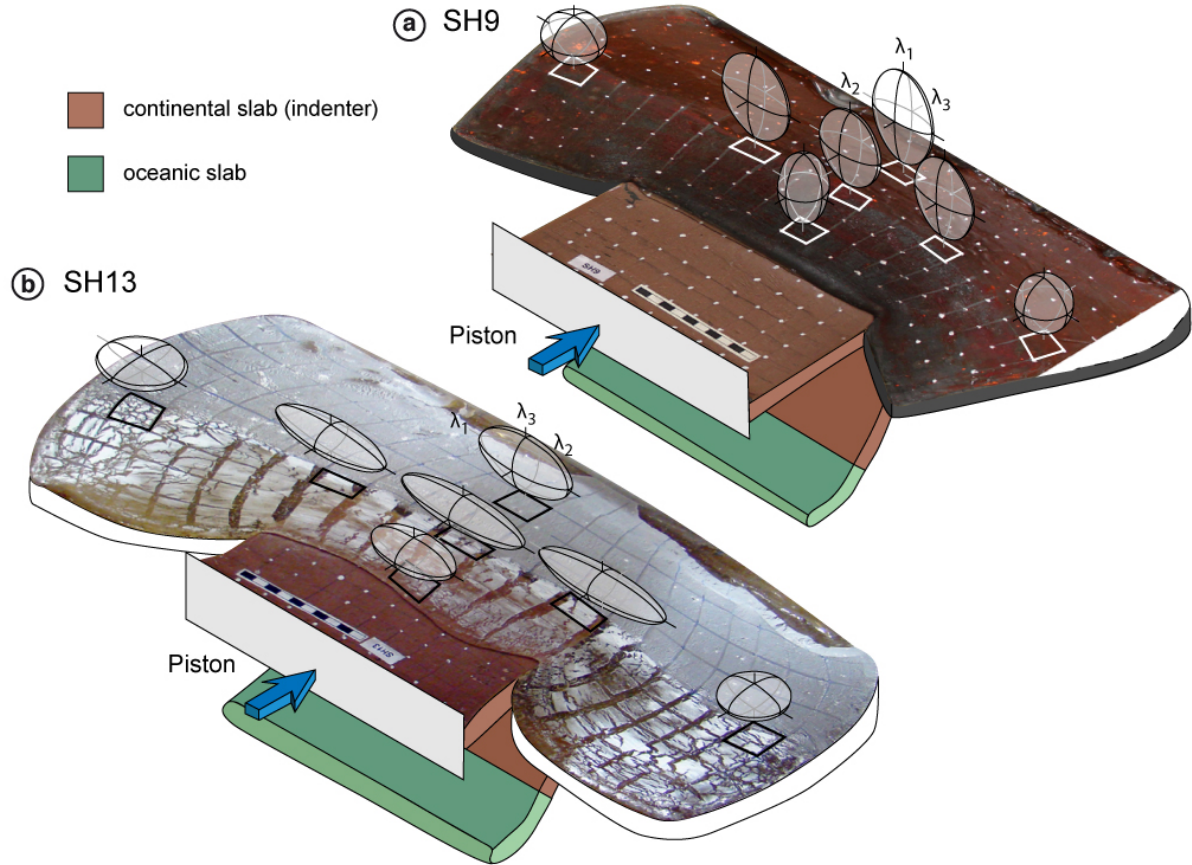


Figure IV.10. Three-dimensional strain analysis (Appendix A) on two typical experiments (a) SH9 (see Figure IV.5 for details), (b) SH13 (see Figure IV.7 for details).

4.3. Lateral decoupling

If the continent is bounded by two lateral oceans (Figure IV.8 and 9), they subduct vertically or slightly retreat, while the continent moves forwards and shapes the range. The parameters controlling the orientation of the suture are identical to experiments without lateral oceans: a low viscosity trench is required and the buoyancy number influences the amplitude of curvature. However, with lateral oceans the syntaxes are wider and the curvature less pronounced. The extreme lateral decoupling reproduced with a continental indenter alone, favors the appearance of an arcuate suture convex towards the upper plate as observed for the

Himalayan range (Figure IV.1). This configuration mimics the strong lateral decoupling of the Indian continent sliding northwards along the Sagaing fault to the east and the Chaman fault to the west (Figure IV.1). It leads to a larger indentation of the upper plate and sharper syntaxes.

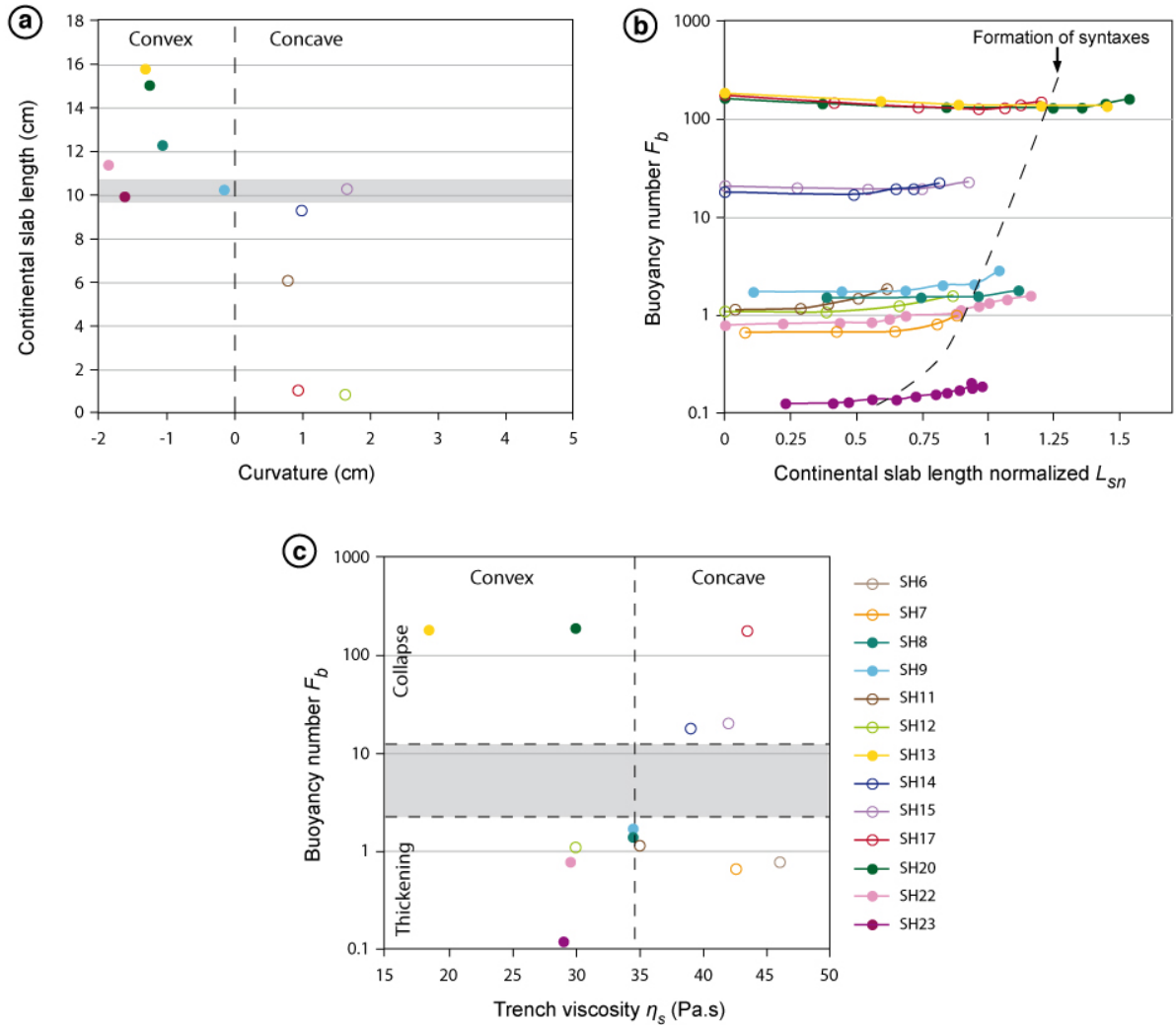


Figure IV.11. (a) Continental slab length as a function of curvature at 40 min (22 My). Filled circles are those of experiments with syntaxes and convex curvature (positive), empty circles those of experiments without syntaxes and concave curvature (negative). The shaded area represents the transition zone between convex and concave oroclines. All experiments with a convex orocline have undergone more than 10 cm of continental subduction (efficient; see text for details). (b) Graph representing the buoyancy number (F_b) versus the normalized continental slab length (L_{sn}). The dotted line highlights the stage of syntaxes formation. (c)

Buoyancy number and trench viscosity plotted for each experiment showing four domains with concave or convex curvature, and thickening or collapse dynamic. The boundary between thickening and collapse regimes is uncertain and illustrated by the shaded area.

4.4. Comparison with the India-Asia collision

The Himalaya range shape is convex towards the overriding plate, with two syntaxes at both east and west extremities (Figure IV.1). This shape is correctly reproduced in our experiments, when continental subduction is continuous (Figures IV.4, IV.5, IV.7 and IV.9). An efficient subduction process is driven by a well lubricated trench, corresponding to a lower viscosity of the asthenosphere. When the force balance reaches neutral buoyancy of the slab, the subducting plate underthrusts the upper one at a flat angle, which accommodates a part of the convergence previously undertaken by the subduction. The transfer from vertical motion (sinking slab) to horizontal one (relative transversal flow/underthrusting) results in a convex orocline. The global tomography shows that the continental subduction of India has been active since the beginning of the indentation [Negredo *et al.*, 2007; Replumaz *et al.*, 2010a]. It has been shown that beneath Southern Tibet [e.g. Nabelek *et al.*, 2009] and Hindu Kush [Negredo *et al.*, 2007], this subduction process is coupled with underthrusting. The results of our laboratory experiments suggest that this process, active since the beginning of indentation and increasing as collision proceeds, is partly responsible for the curvature of the Himalayan range. This efficient subduction can be explained by the high velocity of the Indian plate, due to active convection. This is not the case for other mountain belts showing a curvature concave toward the overriding plate (e.g. Andes, Alps, Bitlis) or straight (e.g. Pyrenees, Rockies Mountains).

The convexity of Himalayan range observed today and measured in the same way as for our experiments is about 350 km. We have to take into account that we simulated ca. 15 My of collision (occurring generally from 20 to 45 min) while it started 45 My ago for India-Asia. Our experiments show a linear increase of curvature with time during continental collision and we can thus extrapolate the value for 45 My. The curvature of experiment SH9 would be equivalent to 310 km after 45 My of collision and the one of SH13 to 400 km. This suggests that the current state of the Himalayan range is best represented by a rheology intermediate between these two experiments.

The dynamic in experiments with high F_b is dominated by collapse dynamic, enhancing the lateral spreading and reducing the thickening in front of the indenter (Figures IV.6, IV.7

and IV.9). The indentation of such a high F_b lithosphere could produce an overall range shape similar to the Himalayan, with a convex curvature (Figures IV.7 and IV.9), but could not reproduce the thickening of the Tibetan Plateau, and generates an overestimated extrusion. Nevertheless, it may be compared to the late evolution of orogenic plateaux such as Tibet. Indeed, the Tibetan upper plate may become weaker when it thickens [e.g. *Kind et al.*, 2002; *Nabelek et al.*, 2009], increasing the component of gravitational collapse. The induced lateral spreading would enhance E-W extension activating N-S striking grabens in Southern Tibet at ca. 15 My [e.g. *Armijo et al.*, 1986; *Williams et al.*, 2001] coupled with strike-slip motion along the Jiali fault [*Armijo et al.*, 1989]. However, the amount and velocity of collapse of high F_b experiments is probably overestimated compared to the Tibetan Plateau.

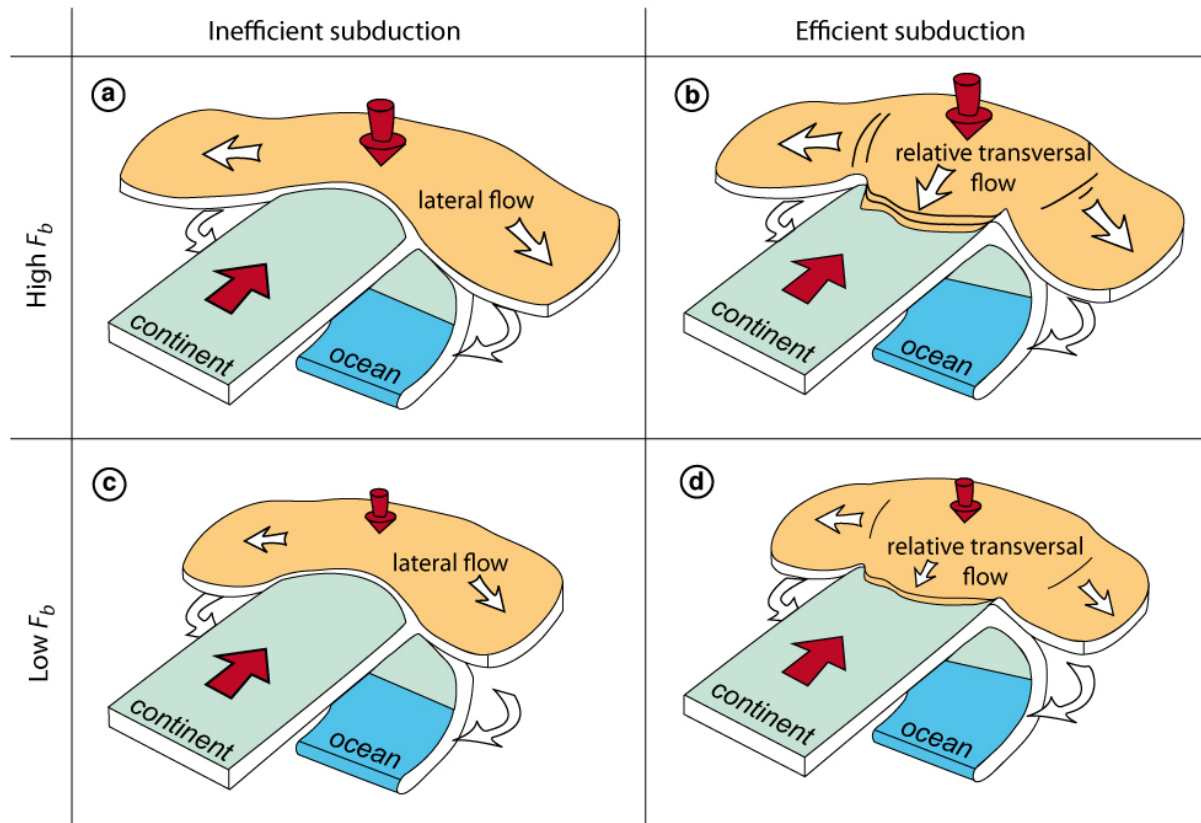


Figure IV.12. Sketch summarizing the possible indentation dynamics depending on buoyancy number and subduction efficiency. (a) Reduced crustal thickening with indentation, large lateral flow, no overthrusting, (b) reduced crustal thickening, large lateral flow, large overthrusting, (c) large crustal thickening with indentation, reduced lateral flow, no overthrusting, (d) large crustal thickening, reduced lateral flow, reduced overthrusting.

5. Conclusions: Four end-members regimes of indentation

Our experiments highlight four end-members regimes of indentation (Figures IV.11c and IV.12):

(1) high buoyancy number (collapse), high viscosity trench: collision regime leading to concave curvature and absence of syntaxes, with lateral extrusion as a main process of deformation of the upper plate and limited thickening (SH15; Figures IV.6, IV.11c and IV.12a).

(2) high buoyancy number (collapse), low viscosity trench: indentation regime enhancing large amplitude syntaxes and convex curvature with large lateral flow, overthrusting of the upper plate and vertical thinning such as occurring today in the Tibetan plateau (SH13; Figures IV.7, IV.11c and IV.12b).

(3) low buoyancy number (thickening) and high viscosity trench: collision regime leading to concave curvature and absence of syntaxes, with thickening coupled to limited lateral extrusion (SH7; Figures IV.3, IV.11c and IV.12c).

(4) low buoyancy number (thickening) and low viscosity trench: a collisional regime promoting convex curvature and thickening coupled to lateral escape that could be compare to early stages of India-Asia history, shape of the suture and thickening of the Tibetan Plateau (SH9; Figures IV.5, IV.11c and IV.12d).

Acknowledgments

F. Bajolet was funded by the European Union FP7 Marie Curie ITN “Crystal2Plate”, contract n° 215353. Experiments presented in this paper have been realized at the Laboratory of Experimental Tectonics, Univ. “Roma TRE”, Italy. A. Replumaz and R. Lainé were funded by Université de Grenoble Joseph Fourier and LabEx *OSUG@2020*. We are grateful to Syral srl for providing us the sugar syrup used in our experimental models.

References

- Alvarez, W. (2010), Protracted continental collisions argue for continental plates driven by basal traction, *Earth Planet. Sci. Lett.*, 296(3-4), 434-442, doi:10.1016/j.epsl.2010.05.030.
- Armijo, R., P. Tapponnier, and H. Tonglin (1989), Late Cenozoic right-lateral strike-slip faulting in Southern Tibet, *J. Geophys. Res.*, 94(B3), 2787-2838, doi:10.1029/JB094iB03p02787.
- Armijo, R., P. Tapponnier, J. L. Mercier and H. Tong-Lin (1986), Quaternary extension in Southern Tibet: Field observations and tectonic implications, *J. Geophys. Res.*, 91, B14, doi: 10.1029/JB091iB14p13803.
- Artyushkov, E. V. (1973), Stresses in the lithosphere caused by crustal thickness inhomogeneities, *J. Geophys. Res.*, 78(32), 7675–7708, doi:10.1029/JB078i032p07675.
- Ayoub, F., S. Leprince, and J.-P. Avouac (2009), Co-registration and correlation of aerial photographs for ground deformation measurements, *Isprs Journal of Photogrammetry and Remote Sensing*, 64(6), 551-560, doi:10.1016/j.isprsjprs.2009.03.005.
- Becker, T. W., C. Faccenna, R. J. O'Connell, and D. Giardini (1999), The development of slabs in the upper mantle: Insights from numerical and laboratory experiments, *J. Geophys. Res.*, 104(B7), 15207-15226, doi:10.1029/1999jb900140.
- Becker, T. W., and C. Faccenna (2011), Mantle conveyor beneath the Tethyan collisional belt, *Earth Planet. Sci. Lett.*, 310(3-4), 453-461, doi:10.1016/j.epsl.2011.08.021.

- Bellahsen, N., C. Faccenna, F. Funiciello, J. M. Daniel, and L. Jolivet (2003), Why did Arabia separate from Africa? Insights from 3-D laboratory experiments, *Earth Planet. Sci. Lett.*, *216*(3), 365-381, doi:10.1016/s0012-821x(03)00516-8.
- Bellahsen, N., C. Faccenna, and F. Funiciello (2005), Dynamics of subduction and plate motion in laboratory experiments: Insights into the "plate tectonics" behavior of the Earth, *J. Geophys. Res.*, *110*(B1), B01401 doi:10.1029/2004jb002999.
- Capitanio, F. A., C. Faccenna, S. Zlotnik, and D. R. Stegman (2011), Subduction dynamics and the origin of Andean orogeny and the Bolivian orocline, *Nature*, *480*(7375), 83-86, doi:10.1038/nature10596.
- Chemenda, A. I., J. P. Burg, and M. Mattauer (2000), Evolutionary model of the Himalaya-Tibet system: geopoem based on new modelling, geological and geophysical data, *Earth Planet. Sci. Lett.*, *174*(3-4), 397-409, doi:10.1016/s0012-821x(99)00277-0.
- Conrad, C. P., and B. H. Hager (1999), Effects of plate bending and fault strength at subduction zones on plate dynamics, *J Geophys Res.*, *104*(B8), 17551-17571, doi:10.1029/1999jb900149.
- Copley, A. (2012), The formation of mountain range curvature by gravitational spreading., *Earth Planet. Sci. Lett.*, *351-352*, 208-214, doi:10.1016/j.epsl.2012.07.036.
- Davy, P., and P. R. Cobbold (1991), Experiments on Shortening of a 4-Layer Model of the Continental Lithosphere, *Tectonophysics*, *188*(1-2), 1-25, doi:10.1016/0040-1951(91)90311-F.
- England, P., and D. McKenzie (1982), A thin viscous sheet model for continental deformation, *Geophys. J. R. Astr. Soc.*, *70*(2), 295-321, doi:10.1111/j.1365-246X.1982.tb04969.x.
- England, P., and G. Houseman (1986), Finite strain calculations of continental deformation .2. Comparison with the India-Asia collision zone, *J. Geophys. Res.*, *91*(B3), 3664-3676, doi:10.1029/JB091iB03p03664.
- Funiciello, F., C. Faccenna, D. Giardini, and K. Regenauer-Lieb (2003), Dynamics of retreating

- slabs: 2. Insights from three-dimensional laboratory experiments, *J. Geophys. Res.*, *108*(B4), 2207, doi:10.1029/2001jb000896.
- Funiciello, F., M. Moroni, C. Piromallo, C. Faccenna, A. Cenedese, and H. A. Bui (2006), Mapping mantle flow during retreating subduction: Laboratory models analyzed by feature tracking, *J. Geophys. Res.*, *111*(B3), B03402, doi:10.1029/2005JB003792.
- Funiciello, F., C. Faccenna, A. Heuret, S. Lallemand, E. Di Giuseppe, and T. W. Becker (2008), Trench migration, net rotation and slab-mantle coupling, *Earth Planet. Sci. Lett.*, *271*(1-4), 233-240, doi:10.1016/j.epsl.2008.04.006.
- Ghosh, A., T. W. Becker, and S. Zhong (2010), Effects of lateral viscosity variations on the geoid., *Geophys. Res. Lett.*, *37*, L01301, doi:10.1029/2009GL040426.
- Hetenyi, G., R. Cattin, F. Brunet, L. Bollinger, J. Vergne, J. Nabelek, and M. Diament (2007), Density distribution of the India plate beneath the Tibetan plateau: Geophysical and petrological constraints on the kinetics of lower-crustal eclogitization, *Earth Planet. Sci. Lett.*, *264*(1-2), 226-244, doi:10.1016/j.epst.2007.09.036.
- Kapp, P., and J. H. Guynn (2004), Indian punch rifts Tibet, *Geology*, *32*(11), 993-996, doi:10.1130/g20689.1.
- Kind, R., X. Yuan, J. Saul, D. Nelson, S. V. Sobolev, J. Mechie, W. Zhao, G. Kosarev, J. Ni, U. Achauer, and M. Jiang (2002), Seismic images of crust and upper mantle beneath Tibet: Evidence for Eurasian plate subduction, *Science*, *298*, 1219-1221.
- Lallemand, S., A. Heuret, and D. Boutelier (2005), On the relationships between slab dip, back-arc stress, upper plate absolute motion, and crustal nature in subduction zones, *Geochem. Geophys. Geosyst.*, *6*, Q09006, doi:10.1029/2005gc000917.
- Lave, J., and J. P. Avouac (2000), Active folding of fluvial terraces across the Siwaliks Hills, Himalayas of central Nepal, *J. Geophys. Res.*, *105*(B3), 5735-5770, doi:10.1029/1999jb900292.
- Leprince, S., F. Ayoub, Y. Klinger, J.-P. Avouac, and Ieee (2007), Co-Registration of Optically

- Sensed Images and Correlation (COSI-Corr): an operational methodology for ground deformation measurements, in *Igarss: 2007 Ieee International Geoscience and Remote Sensing Symposium, Vols 1-12: Sensing and Understanding Our Planet*, edited, pp. 1943-1946.
- Li, C., R. D. Van der Hilst, A. S. Meltzer, and E. R. Engdahl (2008), Subduction of the Indian lithosphere beneath the Tibetan Plateau and Burma, *Earth Planet. Sci. Lett.*, 274(1-2), 157-168, doi:10.1016/j.epsl.2008.07.016.
- Magni, V., J. van Hunen, F. Funiciello, and C. Faccenna (2012), Numerical models of slab migration in continental collision zones, *Solid Earth*, 3(2), 293-306, doi:10.5194/se-3-293-2012.
- Malavieille, J. (1984), Experimental-model for imbricated thrusts - comparison with thrust-belts, *Bull. Soc. Geol. Fr.*, 26(1), 129-138.
- McCaffrey, R., and J. Nabelek (1998), Role of oblique convergence in the active deformation of the Himalayas and southern Tibet plateau, *Geology*, 26(8), 691-694, doi:10.1130/0091-7613(1998)026<0691:roocit>2.3.co;2.
- Mohadjer, S., et al. (2010), Partitioning of India-Eurasia convergence in the Pamir-Hindu Kush from GPS measurements, *Geophys. Res. Lett.*, 37, L04305, doi:10.1029/2009gl041737.
- Molnar, P., and J. M. Stock (2009), Slowing of India's convergence with Eurasia since 20 Ma and its implications for Tibetan mantle dynamics, *Tectonics*, 28, TC3001, doi:10.1029/2008tc002271.
- Nabelek, J., G. Hetenyi, J. Vergne, S. Sapkota, B. Kafle, M. Jiang, H. P. Su, J. Chen, B. S. Huang, and H.-C. Team (2009), Underplating in the Himalaya-Tibet Collision Zone Revealed by the Hi-CLIMB Experiment, *Science*, 325(5946), 1371-1374.
- Negredo, A. M., A. Replumaz, A. Villasenor, and S. Guillot (2007), Modeling the evolution of continental subduction processes in the Pamir-Hindu Kush region, *Earth Planet. Sci. Lett.*, 259(1-2), 212-225, doi:10.1016/j.epsl.2007.04.043.
- Patriat, P., and J. Achache (1984), India Eurasia collision chronology has implications for crustal shortening and driving mechanism of plates, *Nature*, 311(5987), 615-621,

doi:10.1038/311615a0.

- Regard, V., C. Faccenna, J. Martinod, O. Bellier, and J. C. Thomas (2003), From subduction to collision: Control of deep processes on the evolution of convergent plate boundary, *J. Geophys. Res.*, *108*(B4), 2208, doi:10.1029/2002jb001943.
- Regard, V., C. Faccenna, J. Martinod, and O. Bellier (2005), Slab pull and indentation tectonics: insights from 3D laboratory experiments, *Phys. Earth Planet. In.*, *149*(1-2), 99-113, doi:10.1016/j.pepi.2004.08.011.
- Replumaz, A., A. M. Negredo, S. Guillot, and A. Villasenor (2010a), Multiple episodes of continental subduction during India/Asia convergence: Insight from seismic tomography and tectonic reconstruction, *Tectonophysics*, *483*(1-2), 125-134, doi:10.1016/j.tecto.2009.10.007.
- Replumaz, A., A. M. Negredo, S. Guillot, P. van der Beek, and A. Villasenor (2010b), Crustal mass budget and recycling during the India/Asia collision, *Tectonophysics*, *492*(1-4), 99-107.
- Rosenberg, C. L., J. P. Brun, F. Cagnard, and D. Gapais (2007), Oblique indentation in the Eastern Alps: Insights from laboratory experiments, *Tectonics*, *26*(2), TC2003, doi:10.1029/2006tc001960.
- Seeber, L., and A. Pecher (1998), Strain partitioning along the Himalayan arc and the Nanga Parbat antiform, *Geology*, *26*(9), 791-794, doi:10.1130/0091-7613(1998)026<0791:spatha>2.3.co;2.
- Sokoutis, D., M. Bonini, S. Medvedev, M. Boccaletti, C. J. Talbot, and H. Koyi (2000), Indentation of a continent with a built-in thickness change: experiment and nature, *Tectonophysics*, *320*(3-4), 243-270, doi:10.1016/s0040-1951(00)00043-3.
- Stein, S., S. Cloetingh, N. H. Sleep, and R. Wortel, Passive margin earthquake, stress and rheology, in *Earthquakes at the North Atlantic Passive Margin: Neotectonics and Postglacial Rebound*, edited by S. Gregersen and P. W. Basham, pp. 231-259, Kluwer Acad., Norwell, MA, 1989.
- Stegman, D. R., R. Farrington, F. A. Capitanio, and W. P. Schellart (2010), A regime diagram for

- subduction styles from 3-D numerical models of free subduction, *Tectonophysics*, 483(1-2), 29-45, doi:10.1016/j.tecto.2009.08.041.
- Tapponnier, P., G. Peltzer, A. Y. Ledain, R. Armijo, and P. Cobbold (1982), Propagating extrusion tectonics in Asia - New insights from simple experiments with plasticine, *Geology*, 10(12), 611-616, doi:10.1130/0091-7613(1982)10<611:petian>2.0.co;2.
- Ton, S., and M. J. R. Wortel (1997), Slab detachment in continental collision zones: An analysis of controlling parameters, *Geophys. Res. Lett.*, 24(16), 2095-2098.
- Turcotte, D. L., The state of stress at passive continental margin, in *Dynamics of Passive Margins, Geodyn. Ser.*, vol. 6, edited by R. A. Scrutton, pp. 141-146, AGU, Washington D. C., 1982.
- Van der Voo, R., W. Spakman, and H. Bijwaard (1999), Tethyan subducted slabs under India, *Earth Planet. Sci. Lett.*, 171(1), 7-20, doi:10.1016/s0012-821x(99)00131-4.
- van Hinsbergen, D. J. J., B. Steinberger, P. V. Doubrovine, and R. Gassmoeller (2005), Acceleration and deceleration of India-Asia convergence since the Cretaceous: Roles of mantle plumes and continental collision, *J. Geophys. Res.*, 116, B06101, doi:10.1029/2010jb008051.
- Weijermars, R., and H. Schmeling (1986), Scaling of Newtonian and non-Newtonian fluid dynamics without inertia for quantitative modeling of rock flow due to gravity (including the concept of rheological similarity), *Phys. Earth Planet. In.*, 43, 316-330, doi:10.1016/0031-9201(86)90021-X.
- Weijermars, R. (1986), Flow behavior and physical-chemistry of bouncing putties and related polymers in view of tectonic laboratory applications, *Tectonophysics*, 124(3-4), 325-358, doi:10.1016/0040-1951(86)90208-8.
- Williams, H., S. Turner, S. Kelley, and N. Harris (2001), Age and composition of dikes in Southern Tibet: New constraints on the timing of east-west extension and its relationship to postcollisional volcanism, *Geology*, 29(4), 339-342, doi:10.1130/0091-7613(2001)029<0339:AACODI>2.0.CO;2.

Wortel, M. J. R., and W. Spakman (2000), Geophysics - Subduction and slab detachment in the Mediterranean-Carpathian region, *Science*, 290(5498), 1910-1917, doi:10.1126/science.290.5498.1910.